②

RADC-TR-89-123
Interim Technical Report
August 1989

RECONFIGURABLE ANTENNAS - MONOLITHIC MICROWAVE INTEGRATED CIRCUITS WITH FEEDING NETWORKS FOR MICROSTRIP ANTENNAS

University of Illinois

Y.T. Lo, S.L. Chuang, P. Aoyagi

APPROVED FOR PUBLIC RELEASE; DISTRIBUTION UNLIMITED.

ROME AIR DEVELOPMENT CENTER
Air Force Systems Command
Griffiss Air Force Base, NY 13441-5700

This report has been reviewed by the RADC Public Affairs Division (PA) and is releasable to the National Technical Information Service (NTIS). At NTIS it will be releasable to the general public, including foreign nations.

RADC-TR-89-123 has been reviewed and is approved for publication.

APPROVED: Charles J. Drane

CHARLES J. DRANE
Project Engineer

APPROVED: John K. Schindler

JOHN K. SCHINDLER
Director of Electromagnetics

FOR THE COMMANDER: John A. Ritz

JOHN A. RITZ
Directorate of Plans & Programs

If your address has changed or if you wish to be removed from the RADC mailing list, or if the addressee is no longer employed by your organization, please notify RADC (EEAA) Hanscom AFB MA 01731-5000. This will assist us in maintaining a current mailing list.

Do not return copies of this report unless contractual obligations or notices on a specific document require that it be returned.

UNCLASSIFIED
SECURITY CLASSIFICATION OF THIS PAGE

REPORT DOCUMENTATION PAGE

Form Approved
OMB No. 0704-0188

1a. REPORT SECURITY CLASSIFICATION UNCLASSIFIED

1b. RESTRICTIVE MARKINGS N/A

2a. SECURITY CLASSIFICATION AUTHORITY N/A

2b. DECLASSIFICATION / DOWNGRADING SCHEDULE N/A

3. DISTRIBUTION / AVAILABILITY OF REPORT Approved for public release; Distribution unlimited.

4. PERFORMING ORGANIZATION REPORT NUMBER(S) N/A

5. MONITORING ORGANIZATION REPORT NUMBER(S) RADC-TR-89-123

6a. NAME OF PERFORMING ORGANIZATION University of Illinois

6b. OFFICE SYMBOL *(If applicable)*

7a. NAME OF MONITORING ORGANIZATION Rome Air Development Center (EEAA)

6c. ADDRESS *(City, State, and ZIP Code)*
1406 W Green St
Urbana IL 61801-2991

7b. ADDRESS *(City, State, and ZIP Code)*
Hanscom AFB MA 01731-5000

8a. NAME OF FUNDING / SPONSORING ORGANIZATION Rome Air Development Center

8b. OFFICE SYMBOL *(If applicable)* EEAA

9. PROCUREMENT INSTRUMENT IDENTIFICATION NUMBER F19628-85-K-0052

8c. ADDRESS *(City, State, and ZIP Code)*
Hanscom AFB MA 01731-5000

10. SOURCE OF FUNDING NUMBERS

PROGRAM ELEMENT NO.	PROJECT NO.	TASK NO.	WORK UNIT ACCESSION NO.
61102F	2305	J3	48

11. TITLE *(Include Security Classification)*
RECONFIGURABLE ANTENNAS - MONOLITHIC MICROWAVE INTEGRATED CIRCUITS WITH FEEDING NETWORKS FOR MICROSTRIP ANTENNAS

12. PERSONAL AUTHOR(S) Y. T. Lo, S. L. Chuang, P. Aoyagi

13a. TYPE OF REPORT Interim

13b. TIME COVERED FROM Sep 86 TO Sep 87

14. DATE OF REPORT *(Year, Month, Day)* August 1989

15. PAGE COUNT 168

16. SUPPLEMENTARY NOTATION N/A

17. COSATI CODES

FIELD	GROUP	SUB-GROUP
17	02	
17	03	

18. SUBJECT TERMS *(Continue on reverse if necessary and identify by block number)*
Integrated Microstrip Antennas; Arrays; Feeding Networks; Coplanar Lines

19. ABSTRACT *(Continue on reverse if necessary and identify by block number)*

This report consists of two parts and a preface. In the preface, six viable interfacing techniques between the microstrip integrated circuits and the microstrip antennas through the feeding networks are discussed with the comments on their advantages and disadvantages.

In Part 1, the microstrip antenna fed by a slot line is investigated both theoretically and experimentally. This configuration is an attractive element for use in active integrated arrays. This new hybrid technology attempts to incorporate active devices such as amplifier and phase shifters with printed microstrip antennas into a single monolithic package. The boundary value problem for the antenna is analyzed in terms of the integral equations for the equivalent electric currents on the patch and magnetic currents representing the slot line. The integral equations are discretized by Galerkin's method and solved on the computer.

20. DISTRIBUTION / AVAILABILITY OF ABSTRACT ☐ UNCLASSIFIED/UNLIMITED ☒ SAME AS RPT. ☐ DTIC USERS

21. ABSTRACT SECURITY CLASSIFICATION UNCLASSIFIED

22a. NAME OF RESPONSIBLE INDIVIDUAL Dr. Charles J. Drane

22b. TELEPHONE *(Include Area Code)* (617) 377-2051

22c. OFFICE SYMBOL RADC (EEAA)

DD Form 1473, JUN 86 *Previous editions are obsolete.*

SECURITY CLASSIFICATION OF THIS PAGE
UNCLASSIFIED

TABLE OF CONTENTS

PREFACE

By and large the theories for microstrip antennas have been well developed. In general, they can be divided into three levels with various degrees of complexity and computation effort. The applicability of each theory depends on the substrate thickness, geometrical shape, feed structure, the antenna performance parameters to be evaluated (such as input impedances, radiation patterns, directivities etc.), and, of course, the accuracy desired. Except for the difference in computer time, the theoretical problem of microstrip antennas is considered solved.

For reaching the final goal of this study, namely to design and demonstrate the feasibility of MMIC integrated microstrip antenna arrays, there are two major problems needed to be solved. The first is the development of microwave devices, in particular the phase shifters, which would require a large effort and is not within the scope of this research project. The second problem is to develop an interfacing system between the devices and the antennas, including microwave circuit analyses and designs. This interim report covers the work performed in this area.

As reported earlier, in our view there are six basic viable interfacing techniques as listed in Table A with comments on their relative advantages and disadvantages. Since all these feeding systems should interact strongly with the antennas, they must be analyzed together with the antenna. Theories for the first four configurations have been developed while the remaining two are under current study. In particular, the analysis of slot excitation is presented in Part I, and that of coplanar lines (also called coplanar waveguides) in Part II. In actual implementation, two or more of the six configurations may be used. This is illustrated in a few sample designs in Part II, including a simple element, a two-element array, and a four-element array, with and without an integrated FET amplifier. Their excellent performances, as shown in Part II, clearly indicate the viability of these techniques.

We believe that our study is reaching a final stage. We are very anxious to complete the investigation by making a sample design of a MMIC integrated array. To this end, we are urgently in need of phase shifters. We have been seeking help from industrial companies, so far, without much success. In the meantime, our activities have been focused on the wideband design, and CP designs, in addition to the analysis of the interfacing configurations V and VI shown in Table A.

Table A

Various Methods for Feeding Microstrip Antennas

Method	Major Advantage	Major Disadvantage
I. Probe feed via hole 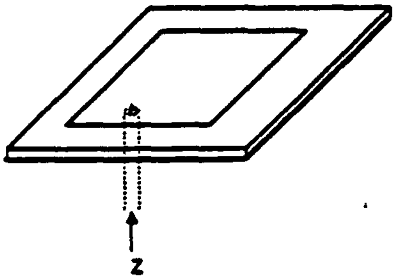 	No feed line radiation loss, little coupling between patch & line, different value of Z obtainable by choosing feed location, Z of thin patch easily predicted.	Complicated and costly in fabrication, difficult to incorporate feed B. C. into analysis
II. Microstrip-line edge feed 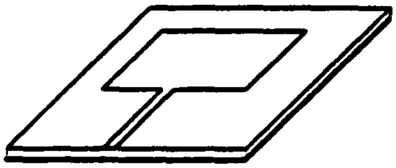	Both can be printed in one step	Inflexible in design since both feed and patch are over the same substrate, resulting in erratic radiation for mm-waves

Method	Major Advantage	Major Disadvantage
III. Electromagnetically coupled microstrip-line feed 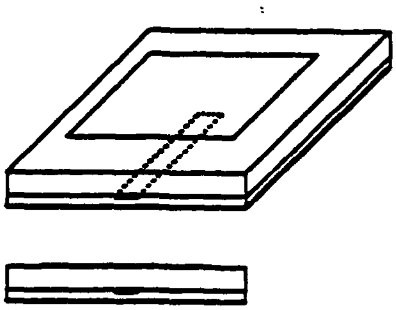	Flexibility in microstrip line and patch design	Requires two layers of substrates, difficult for integration with active devices and their heat dissipation
IV. Slot feed 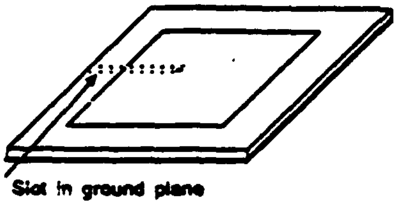	Simple in fabrication, easy in integration with active device & good for heat dissipation, both patch & slot can be etched in one step	Slot may cause stray radiation, limitation in large feeding network layout

Method	Major Advantage	Major Disadvantage
V. Coplanar waveguide feed 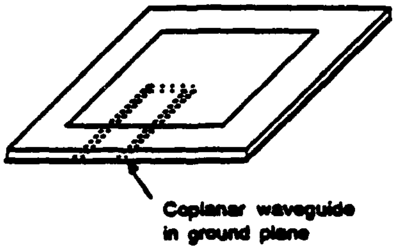 	Same as above. Small stray radiation from feed	Requiring more space, less freedom in large feed network design
VI. Aperture coupling feed 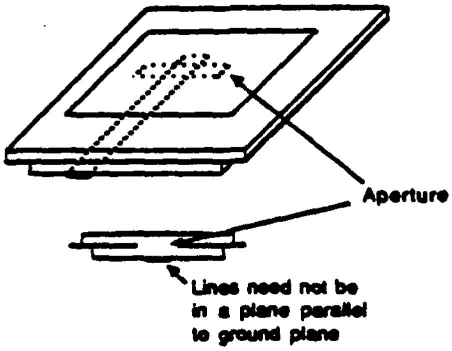 	More freedom: feeding network and patches can be designed separately	Costly and complex, requiring more space under ground plane

General Remarks:

(1) For large arrays, a combination of two or more above feeding methods may be used.

(2) The type of feed to be used should be dictated by array size, frequency, and cost considerations.

Part I.

Numerical Methods for the Electromagnetic Modeling of Microstrip Antennas and Feed Systems

by

D. R. Tanner
Y. T. Lo
P. E. Mayes

NUMERICAL METHODS FOR THE ELECTROMAGNETIC MODELING OF MICROSTRIP ANTENNAS AND FEEDSYSTEMS

David Robert Tanner, Ph.D.
Department of Electrical and Computer Engineering
University of Illinois at Urbana-Champaign, 1988

The importance of low-cost printed circuit antennas has brought about a continued effort to improve and simplify the analysis of multilayered or stratified media. This report derives the dyadic Green functions for the electromagnetic fields in a multilayered medium and shows their relationship to the more familiar Green functions for ordinary transmission lines. This approach simplifies the analysis and allows the treatment of an arbitrary number of layers with a minimal increase in effort.

The theory is applied to the analysis of a microstrip antenna fed by a slot line. This configuration is an attractive element for use in active integrated arrays. This new hybrid technology attempts to incorporate active devices such as amplifiers and phase shifters with printed "microstrip" antennas into a single monolithic package. The boundary value problem for the antenna is analyzed in terms of the integral equations for the equivalent electric currents on the patch and magnetic currents representing the slot line. The integral equations are discretized by Galerkin's method and solved on the computer. Techniques designed to enhance the convergence of the spectral domain integrals are described. Important antenna parameters such as the input reflection coefficient are extracted from the solution of the boundary value problem. The problem concerning definition of antenna impedance (which is nonunique) can be avoided by using this technique. Finally, a method for obtaining automated measurements of the antenna reflection coefficient in the guide of interest is developed. Measurements of the reflection coefficient in a slot line feeding a microstrip patch are compared with computer-generated results of the theory.

TABLE OF CONTENTS

1. INTRODUCTION

1.1. Previous Work

The first theories for microstrip antennas were based on the so-called transmission line model [1], [2]. This theory uses a single "transmission line" mode approximation and roughly predicts the aperture fields and, thus, the far-field patterns. However, its ability to estimate the input impedance is rather poor.

A significant improvement in the theory and understanding soon followed with the "thin cavity models" [3], [4]. This theory included a full modal description of the fields under the patch closed by an approximating "magnetic wall" along its periphery. The cavity model proved to be excellent from an engineering standpoint since it succeeded in describing most of the observable phenomena with reasonable accuracy.

However, as operating frequencies are pushed to higher limits, the cavity model deteriorates for electrically thicker substrates. This led researchers to more rigorous models based on the satisfaction of Maxwell's equations and boundary conditions over the microstrip patch [5], [6]. Typically, the exact Green functions for the fields are used in a method of moments solution. Much effort was put into the general basis function modeling of the patch. These solutions required hundreds of unknowns and necessitated the development of efficient means for computing the slowly convergent series.

Earlier work has shown, however, that practically all shapes of microstrip antennas operating about a single resonant mode radiate nearly identical patterns. The simple shapes such as the rectangular and circular patches work as well as patches of any other shape. Thus, a large degree of freedom in the patch model does not appear to be the highest priority. However, the experience gained in the process has been useful. The "input impedance" in these first rigorous models was defined much the same as in the simpler cavity models and therefore yielded only marginally improved results.

Engineers were quick to realize that the input reactance is strongly determined by the fields in the immediate vicinity of the antenna-feed transition. Thus, accurate satisfaction of the boundary conditions in the transition region between the feed line and the antenna is crucial in accounting for the "observable" effects in the input line. Indeed, even the simple cavity model theory was found to yield improved results when boundary conditions were more strictly enforced in the feed region for coaxial probes [7]. Also, circular patch antennas excited by microstrip lines were studied in [7]. However, input impedance was again defined in a nonunique way by subtracting off the effects of the extraneous open-circuited stub. Thus, the discontinuity and impedance definition problems appear again in a different place. These problems are addressed by some of the techniques described in this report.

1.2. Overview

The recent trend in microstrip antenna technology has been toward more complex multilayered structures which can include active devices. The devices (typically phase shifters or transistor amplifiers) require protection from the environment and must be placed behind the ground plane or a radome layer. These requirements led most designers to structures requiring two or more layers, one for the active devices and feed system, and another for the antenna elements. However, an alternative arrangement involving only one dielectric layer is possible if the feed system can be incorporated into the ground plane in the form of slot line and/or coplanar waveguide. This report describes the general theory and analysis for solving antenna and scattering problems in multilayered media. The Green functions are developed in a manner which will make them widely applicable and easy to understand. The theory has been applied to the analysis of a slot-line fed rectangular patch. A Fortran-77 program that predicts the antenna reflection coefficient has been written to implement the analysis.

A brief outline of this report follows.

Chapter 2 describes the spectral domain formulation for the dyadic Green functions in a multilayered medium.

Chapter 3 applies the dyadic Green functions to the analysis of a slot-line fed microstrip patch antenna. The integral equations for the unknown currents are formulated in terms of the dyadic Green functions for stratified media above and below the ground plane. The continuous problem is discretized by introducing a set of basis-testing functions for the rectangular patch and slot line. A Galerkin moment method procedure formally reduces the integral equation to a matrix equation. The matrix elements are defined by scalar products in the transform (transverse wavenumber) domain via the Parseval relation and the Fourier transform.

The slot-line fed antenna configuration consists of a rectangular microstrip patch situated on a dielectric slab with an underlying ground plane. A narrow slot in the ground plane extends under the patch in the plane of symmetry. The slot-line excitation is provided by an assumed electric current strip across the slot at the feed point. A major objective is to determine the complex reflection coefficient of the antenna as it appears in the waveguiding medium, in this case, the slot line.

Section 3.1 describes the slot-line fed antenna configuration in more detail.

Section 3.2 describes the formulation of the antenna boundary-value problem. The problem is first cast into a form suitable for computer solution using Galerkin's procedure. This process formally reduces the coupled integral equations to a set of matrix equations which can be solved by well-known direct or iterative methods for linear systems.

Section 3.3 describes the choice of basis-test functions for the expansion of the patch electric current and the slot magnetic current.

Section 3.4 describes the dyadic Green functions in the spectral domain for multilayered stratified media. These Green functions are applied to the evaluation of the matrix elements in the moment method formulation of the problem.

Section 3.5 describes how the antenna reflection coefficient can be extracted from the solution of a moment method formulation of an antenna problem. The method is readily applicable to microstrip lines, coplanar waveguide and slot lines, without requiring any reformulation of the moment method problem.

Chapter 4 describes the convergence enhancement technique applied to the matrix elements for the slot line. This technique combines the singularity subtraction technique with the Parseval relation to yield an efficient evaluation of these matrix elements.

Chapter 5 describes a method for measuring the reflection coefficient in an arbitrary waveguide. Particular attention is addressed to the calibration problem in guides where matched loads and reflection standards are difficult to obtain.

Chapter 6 shows Smith-chart plots comparing the computed and measured reflection coefficient data for a few test antennas.

Many of the important analytical details can be found in Appendices A and B. Some singular integrals required for matrix element evaluation are derived in closed form. Great pains have been taken to organize this material in a manner which will minimize the algebraic labor required as well as the chance for error.

1.3. References

[1] R. E. Munson, "Conformal microstrip antennas and microstrip arrays," *IEEE Trans. Antennas Propag.*, vol. AP-22, pp. 74-78, Jan. 1974.

[2] A. G. Derneryd, "Linearly polarized microstrip antennas," *IEEE Trans. Antennas Propag.*, vol. AP-24, pp. 846-851, Nov. 1976.

[3] Y. T. Lo, D. Solomon and W. F. Richards, "Theory and experiment on microstrip antennas," *IEEE Trans. Antennas Propag.*, vol. AP-27, pp. 137-145, Mar. 1979.

[4] W. F. Richards, Y. T. Lo and D. D. Harrison, "An improved theory for microstrip antennas and applications," *IEEE Trans. Antennas Propag.*, vol. AP-29, pp. 38-46, Jan. 1981.

[5] D. M. Pozar, "Input impedance and mutual coupling of rectangular microstrip antennas," *IEEE Trans. Antennas Propag.*, vol. AP-30, pp. 1191-1196, Nov. 1982.

[6] S. M. Wright, "Efficient analysis of infinite microstrip arrays on electrically thick substrates," Ph.D. dissertation, University of Illinois, Urbana-Champaign, 1984.

[7] M. Davidovitz, "Feed analysis for microstrip antennas," Ph.D. dissertation, University of Illinois, Urbana-Champaign, 1987.

2. DYADIC GREEN FUNCTIONS FOR MULTILAYERED MEDIA

2.1. Overview

This chapter describes the dyadic Green functions for the electromagnetic fields in muitilayered media. Many aspects of this problem can be found in the literature. A common approach is to describe the fields in each layer in terms of the z-component of magnetic vector potential A_z and electric vector potential F_z [1], [2]. This technique leads to field expressions which are valid exterior to the source region and it has been useful in obtaining the fields of transverse current sources from the discontinuity of the transverse fields between two source-free regions. However, the A_z-F_z potential approach does not readily yield the correct fields in the source region for longitudinal sources.

In this chapter, the dyadic Green functions for the full vector fields due to both electric and magnetic sources including longitudinal components are given. The derivation is in terms of the governing equations for the field components rather than the potentials. In this approach [3], the dyadic Green functions for the vector problem are related to the familiar scalar Green functions for an ordinary transmission line (TL). The TL Green functions can be found by inspection by a variety of methods. The resulting dyadic Green functions contain source dyadic terms that are not included in the A_z-F_z potential approach [1], [2].

2.2. Derivation of Green Functions for Stratified Media

The medium under consideration is assumed to be an arbitrary function of the z-coordinate variable only. For a fixed value of z, the medium is translationally invariant and isotropic for any direction transverse to z. For time dependence $e^{j\omega t}$ where ω is nonzero, the time harmonic fields (E, H) are completely described by the Maxwell curl equations. The remaining two Maxwell equations follow from the divergence of the curl equations if ω is nonzero. In light of the natural z-coordinate induced by the medium, it is appropriate to separate the longitudinal and transverse components of the curl equations and introduce longitudinal and transverse components of the field and current vectors. The longitudinal component of the curl operator is given by the identity $\hat{z} \cdot \nabla \times A = -\nabla_t \cdot \hat{z} \times A_t$. The transverse projection of the curl operator rotated about $\hat{z}$ by $\pi/2$ in the right-hand sense is given by $\hat{z} \times \nabla \times A = \nabla_t A_z - \frac{\partial}{\partial z} A_t$. After applying these identities, the Maxwell curl equations reduce to

$$\nabla_t \cdot \hat{z} \times E_t = j\omega\mu H_z + K_z \tag{2.1a}$$

$$\nabla_t \cdot \hat{z} \times H_t = -j\omega\varepsilon E_z - J_z \tag{2.1b}$$

$$\frac{\partial}{\partial z} E_t - \nabla_t E_z = j\omega\mu\, \hat{z} \times H_t + \hat{z} \times K_t \tag{2.2a}$$

$$\frac{\partial}{\partial z} H_t - \nabla_t H_z = -j\omega\varepsilon\, \hat{z} \times E_t - \hat{z} \times J_t \tag{2.2b}$$

The four equations are reduced to two equations after eliminating the z-components of the fields by substituting (2.1b) in (2.2a) and (2.1a) in (2.2b).

$$\frac{\partial}{\partial z} E_t + \left[\nabla_t \frac{1}{j\omega\varepsilon} \nabla_t - j\omega\mu\, I \right] \cdot \hat{z} \times H_t = \hat{z} \times K_t - \nabla_t \frac{J_z}{j\omega\varepsilon} \tag{2.3a}$$

$$\frac{\partial}{\partial z} H_t - \left[\nabla_t \frac{1}{j\omega\mu} \nabla_t - j\omega\varepsilon\, I \right] \cdot \hat{z} \times E_t = -\hat{z} \times J_t - \nabla_t \frac{K_z}{j\omega\mu} \tag{2.3b}$$

where I is the identity dyadic. These equations are now solved by a two-dimensional Fourier transformation F with respect to the transverse coordinates, x and y, to the transform variables, ξ and η. The defining relations for the Fourier transform and inverse are, respectively,

$$\tilde{g} = F[g] = \int_{-\infty}^{\infty}\int_{-\infty}^{\infty} g(x, y)\, e^{+j(\xi x + \eta y)}\, dx\, dy \tag{2.4a}$$

$$g = F^{-1}[\tilde{g}] = \frac{1}{(2\pi)^2}\int_{-\infty}^{\infty}\int_{-\infty}^{\infty} \tilde{g}(\xi, \eta)\, e^{-j(\xi x + \eta y)}\, d\xi\, d\eta \tag{2.4b}$$

The rectangular transform variables (ξ, η) are related to polar transform variables (β, ψ) and unit vectors ($\hat{\beta}$, $\hat{\psi}$) by the relations:

$$\xi = \beta\cos\psi \qquad \eta = \beta\sin\psi \tag{2.5a}$$

$$\beta = \sqrt{\xi^2 + \eta^2} \qquad \psi = \arctan \eta/\xi \tag{2.5b}$$

$$\hat{\beta} = \hat{x}\cos\psi + \hat{y}\sin\psi \qquad \hat{\psi} = \hat{z}\times\hat{\beta} = -\hat{x}\sin\psi + \hat{y}\cos\psi \tag{2.6}$$

$$\bar{\beta} = \hat{\beta}\,\beta = \hat{x}\,\xi + \hat{y}\,\eta \tag{2.7}$$

After noting that the permittivity ε(z) and the permeability μ(z) are independent of (x,y), Equations (2.3a) and (2.3b) are easily transformed to yield

$$\frac{\partial}{\partial z}\tilde{\bar{E}}_t - \left[\bar{\beta}\,\frac{1}{j\omega\varepsilon}\,\bar{\beta} + j\omega\mu\, I\right]\cdot\hat{z}\times\tilde{\bar{H}}_t = \hat{z}\times\tilde{\bar{K}}_t + \bar{\beta}\,\frac{\tilde{J}_z}{\omega\varepsilon} \tag{2.8a}$$

$$\frac{\partial}{\partial z}\tilde{\bar{H}}_t + \left[\bar{\beta}\,\frac{1}{j\omega\mu}\,\bar{\beta} + j\omega\varepsilon\, I\right]\cdot\hat{z}\times\tilde{\bar{E}}_t = -\hat{z}\times\tilde{\bar{J}}_t + \bar{\beta}\,\frac{\tilde{K}_z}{\omega\mu} \tag{2.8b}$$

Note that under the Fourier transform, the differential operator ∇_t is effectively replaced by $-j\bar{\beta}$. For fixed values of the transform variables, these equations completely characterize the relationship of the transverse field transforms to the source transforms for a particular "Fourier component." To solve these equations, consider parallel and perpendicularly polarized components with respect to the plane of incidence (i.e., the plane containing $\hat{z}$ and $\hat{\beta}$). The parallel polarized, E-wave, or transverse magnetic (TM) equations are obtained by taking the $\hat{\beta}$ component of (2.8a) and the $\hat{\psi}$ component of (2.8b), viz.,

$$\frac{\partial}{\partial z}\tilde{E}_\beta + \frac{(\beta^2 - k^2)}{j\omega\varepsilon}\tilde{H}_\psi = -\tilde{K}_\psi + \frac{\beta}{\omega\varepsilon}\tilde{J}_z \tag{2.9a}$$

$$\frac{\partial}{\partial z}\tilde{H}_\psi + j\omega\varepsilon\,\tilde{E}_\beta = -\tilde{J}_\beta \tag{2.9b}$$

Similarly, the perpendicularly polarized, H-wave, or transverse electric (TE) equations are obtained by taking the $\hat{\psi}$ component of (2.8a) and the $\hat{\beta}$ component of (2.8b), viz.,

$$\frac{\partial}{\partial z}\tilde{E}_\psi + j\omega\mu\,(-\tilde{H}_\beta) = \tilde{K}_\beta \tag{2.10a}$$

$$\frac{\partial}{\partial z}(-\tilde{H}_\beta) + \frac{(\beta^2 - k^2)}{j\omega\mu}\tilde{E}_\psi = -\tilde{J}_\psi - \frac{\beta}{\omega\mu}\tilde{K}_z \tag{2.10b}$$

The resulting equations for the E-wave case are completely uncoupled from the H-wave case and both are completely analogous to the following equations for the voltage V(z) and current I(z) along a nonuniform transmission line, viz.,

$$\frac{\partial}{\partial z} V(z) + \gamma(z)\, Z(z)\; I(z) = v(z) \tag{2.11a}$$

$$\frac{\partial}{\partial z} I(z) + \gamma(z)\, Y(z)\; V(z) = i(z) \tag{2.11b}$$

where the characteristic impedance is given by

$$Z(z) = \frac{1}{Y(z)} = \frac{\gamma(z)}{j\omega\epsilon(z)} \qquad \text{for E-waves} \tag{2.12a}$$

$$Z(z) = \frac{1}{Y(z)} = \frac{j\omega\mu(z)}{\gamma(z)} \qquad \text{for H-waves} \tag{2.12b}$$

The complex propagation constant is given by

$$\gamma(z) = \sqrt{\beta^2 - k^2(z)}\,, \qquad -\frac{\pi}{2} < \arg(\gamma(z)) \leq \frac{\pi}{2}\,, \tag{2.13}$$

where $k^2(z) = \omega^2\mu(z)\epsilon(z)$ is the square of the intrinsic wavenumber of the medium. The voltage and current source densities per unit length are, respectively, $v(z)$ and $i(z)$. Thus the solutions of (2.9) and (2.10) are readily expressible in terms of the transmission line (TL) Green functions involving either the E-wave or H-wave characteristic immittance in each case. The complete field transforms are then found by combining the transverse components with the z-components obtained from the FT of (2.1a) and (2.1b).

$$\bar{E} = \hat{\beta}\,\bar{E}_\beta + \hat{\psi}\,\bar{E}_\psi - \hat{z}\,\frac{1}{j\omega\epsilon}\,[\,\bar{J}_z + j\beta\,\bar{H}_\psi\,] \tag{2.14a}$$

$$\bar{H} = \hat{\beta}\,\bar{H}_\beta + \hat{\psi}\,\bar{H}_\psi - \hat{z}\,\frac{1}{j\omega\mu}\,[\,\bar{K}_z - j\beta\,\bar{E}_\psi\,] \tag{2.14b}$$

Considering separately electric and magnetic sources that are confined to a single layer (i.e., a current sheet) yields the following dyadic Green functions shown in Table I. The dyadic that yields the transformed electric field $\tilde{\mathbf{E}}$ due to $\tilde{\mathbf{J}}$ is denoted $\tilde{\mathbf{E}}_{\mathrm{J}}$. The space domain electric field is given by $\mathbf{E} = F^{-1}[\int \tilde{\mathbf{E}}_{\mathrm{J}} \cdot \tilde{\mathbf{J}}\, dz']$. The dyadics involving the magnetic field or current are similarly defined and shown in Table I. Expressed in this form, the relationships of the dyadic Green functions to the scalar TL Green functions are easily seen. The scalar TL Green functions are defined as follows.

$V_I(z,z')$ = voltage at z due to a unit current source at z',
$I_I(z,z')$ = current at z due to a unit current source at z',
$V_V(z,z')$ = voltage at z due to a unit voltage source at z',
$I_V(z,z')$ = current at z due to a unit voltage source at z'.

A superscript E or H will be appended to denote whether the E-wave or H-wave immittance is used throughout, respectively.

One should pay particular attention to the source dyadic terms which are required to obtain the correct z-components of the fields in a source region. These source dyadic terms are identical to those obtained for an infinitely thin pillbox principle volume [4], [5]. These terms can be attributed to the irrotational nature of the field in the source region [5]. They arise because of the inability to completely expand the field in a source region solely in terms of solenoidal modes (e.g., the fields derived from only the z-components of vector potentials). The irrotational component is due to the presence of charges.

Table I

Spectral domain Green functions for stratified or multilayered media.

$$\bar{E}_{\tilde{J}}(\bar{\beta},z,z') = -\hat{\beta}\, V_I^E\, \hat{\beta} - \hat{\psi}\, V_I^H\, \hat{\psi}$$

$$+\ \hat{\beta}\,\frac{\beta\, V_V^E}{\omega\, \varepsilon(z')}\,\hat{z} + \hat{z}\,\frac{I_I^E\, \beta}{\omega\, \varepsilon(z)}\,\hat{\beta} - \hat{z}\left[\frac{\beta^2\, I_V^E}{\omega^2\, \varepsilon(z)\, \varepsilon(z')} + \frac{\delta(z-z')}{j\, \omega\, \varepsilon(z)}\right]\hat{z} \qquad (I.1)$$

$$\bar{H}_{\tilde{J}}(\bar{\beta},z,z') = \hat{\beta}\, I_I^H\, \hat{\psi} - \hat{\psi}\, I_I^E\, \hat{\beta} + \hat{\psi}\,\frac{\beta\, I_V^E}{\omega\, \varepsilon(z')}\,\hat{z} - \hat{z}\,\frac{V_I^H\, \beta}{\omega\, \mu(z)}\,\hat{\psi} \qquad (I.2)$$

$$\bar{E}_{\tilde{K}}(\bar{\beta},z,z') = \hat{\psi}\, V_V^H\, \hat{\beta} - \hat{\beta}\, V_V^E\, \hat{\psi} + \hat{z}\,\frac{I_V^E\, \beta}{\omega\, \varepsilon(z)}\,\hat{\psi} - \hat{\psi}\,\frac{\beta\, V_I^H}{\omega\, \mu(z')}\,\hat{z} \qquad (I.3)$$

$$\bar{H}_{\tilde{K}}(\bar{\beta},z,z') = -\hat{\beta}\, I_V^H\, \hat{\beta} - \hat{\psi}\, I_V^E\, \hat{\psi}$$

$$+\ \hat{\beta}\,\frac{\beta\, I_I^H}{\omega\, \mu(z')}\,\hat{z} + \hat{z}\,\frac{V_V^H\, \beta}{\omega\, \mu(z)}\,\hat{\beta} - \hat{z}\left[\frac{\beta^2\, V_I^H}{\omega^2\, \mu(z)\, \mu(z')} + \frac{\delta(z-z')}{j\, \omega\, \mu(z)}\right]\hat{z} \qquad (I.4)$$

Notes: Transmission line Green functions V_I, I_I, V_V and I_V are functions of (β,z,z'). If the Fourier transformed sources $(\tilde{J}, \tilde{K})$ are functions of z', an integration $\int dz'$ is required to obtain the transformed fields $(\tilde{E}, \tilde{H})$ at z.

2.3. Green Functions for Cascaded Uniform Transmission Lines

Several methods can be used to obtain the TL Green functions, each having their advantages and disadvantages. One approach is to characterize each layer and interface by a transfer matrix T. The T matrix approach can be used to describe the observable quantities at the left end of a line in terms of those at the right end. The observable quantities are typically the right and left traveling mode amplitude, or equivalently, the mode voltage and mode current. In either case, the T matrix for a cascade of layers is obtained as the product of the T matrices for all layers. However, in stratified media the propagation constant γ in the z-direction becomes attenuating as the transverse wavenumber $\beta \rightarrow \infty$. This indicates the evanescent nature of these spectral components. Unfortunately in this case, some elements of the T matrix are of exponential order, growing as $e^{\beta d}$, as $\beta \rightarrow \infty$, where d is the thickness of the layer. When numerical solutions are sought on a computer, exponential growth causes overflow and therefore limits the utility of the transfer matrix approach to wavenumber $\beta < \ln(C) / D$, where C is the largest number the computer can represent and D is the total thickness of all layers.

For numerical computation, it is convenient to characterize a number of layers by using the continuity of wave impedance and the transfer property for the reflection coefficient. Another similar approach is to use the scattering parameters (Fresnel reflection and transmission coefficients) of an interface and the transfer property for the reflection coefficient.

In the first approach, the reflection coefficient Γ is transferred through a layer by multiplication by $e^{-2\gamma d}$ where d is the layer thickness. The transformation of the reflection coefficient through an interface is accomplished by converting Γ to normalized wave impedance, followed by renormalizing to the characteristic (wave) impedance of the next layer and converting back to the reflection coefficient . This process is easily repeated for an arbitrary number of layers and interfaces to obtain the reflection coefficient at any plane.

It should be noted that this method involves only the decaying "exponential propagator" and yields a stable result as $\beta \rightarrow \infty$.

In the second approach, the reflection coefficient is transferred through a layer by multiplication by $e^{-2\gamma d}$. Then transfer through an interface is computed from the well-known formula,

$$\Gamma' = S_{11} + \frac{S_{12}\, S_{21}\, \Gamma}{1 - S_{22}\, \Gamma} \tag{2.15}$$

where the Fresnel reflection coefficients,

$$S_{11} = \frac{Z_2 - Z_1}{Z_2 + Z_1}$$

and $S_{22} = -S_{11}$, are expressed in terms of the characteristic wave impedance for either E-waves (2.12a) or H-waves (2.12b). The Fresnel transmission coefficients of the interface are $S_{21} = 1 + S_{11}$ and $S_{12} = 1 + S_{22}$. The reflection coefficients Γ' and Γ are for outgoing waves immediately before and after the interface, respectively. The above relations between the Fresnel coefficients follow from the continuity of the tangential fields at each interface.

Consider a uniform transmission line (TL) of characteristic impedance $Z_0 = 1/Y_0$ and complex propagation constant γ, bounded by known reflection coefficients Γ_1 at the left end ($z = z_1$) and Γ_2 at the right end ($z = z_2$). The four TL Green functions for this configuration can be expressed as

$$V_I(z,z') = \begin{cases} Z_0 \dfrac{e^{-\gamma|z-z'|}}{2} \dfrac{[1+\Gamma_1 e^{-\gamma 2|z'-z_1|}][1+\Gamma_2 e^{-\gamma 2|z-z_2|}]}{[1-\Gamma_1\Gamma_2 e^{-\gamma 2|z_2-z_1|}]} & \text{for } z' < z \\ \\ Z_0 \dfrac{e^{-\gamma|z-z'|}}{2} \dfrac{[1+\Gamma_1 e^{-\gamma 2|z-z_1|}][1+\Gamma_2 e^{-\gamma 2|z'-z_2|}]}{[1-\Gamma_1\Gamma_2 e^{-\gamma 2|z_2-z_1|}]} & \text{for } z < z' \end{cases} \tag{2.16}$$

$$I_I(z,z') = \begin{cases} \dfrac{e^{-\gamma|z-z'|}}{2} \dfrac{[1+\Gamma_1 e^{-\gamma 2|z'-z_1|}][1-\Gamma_2 e^{-\gamma 2|z-z_2|}]}{[1-\Gamma_1\Gamma_2 e^{-\gamma 2|z_2-z_1|}]} & \text{for } z' < z \\ \\ -\dfrac{e^{-\gamma|z-z'|}}{2} \dfrac{[1-\Gamma_1 e^{-\gamma 2|z-z_1|}][1+\Gamma_2 e^{-\gamma 2|z'-z_2|}]}{[1-\Gamma_1\Gamma_2 e^{-\gamma 2|z_2-z_1|}]} & \text{for } z < z' \end{cases} \tag{2.17}$$

$$V_V(z,z') = \begin{cases} \dfrac{e^{-\gamma|z-z'|}}{2} \dfrac{[1-\Gamma_1 e^{-\gamma 2|z'-z_1|}][1+\Gamma_2 e^{-\gamma 2|z-z_2|}]}{[1-\Gamma_1\Gamma_2 e^{-\gamma 2|z_2-z_1|}]} & \text{for } z' < z \\ \\ -\dfrac{e^{-\gamma|z-z'|}}{2} \dfrac{[1+\Gamma_1 e^{-\gamma 2|z-z_1|}][1-\Gamma_2 e^{-\gamma 2|z'-z_2|}]}{[1-\Gamma_1\Gamma_2 e^{-\gamma 2|z_2-z_1|}]} & \text{for } z < z' \end{cases} \tag{2.18}$$

$$I_V(z,z') = \begin{cases} Y_0 \dfrac{e^{-\gamma|z-z'|}}{2} \dfrac{[1-\Gamma_1 e^{-\gamma 2|z'-z_1|}][1-\Gamma_2 e^{-\gamma 2|z-z_2|}]}{[1-\Gamma_1\Gamma_2 e^{-\gamma 2|z_2-z_1|}]} & \text{for } z' < z \\ \\ Y_0 \dfrac{e^{-\gamma|z-z'|}}{2} \dfrac{[1-\Gamma_1 e^{-\gamma 2|z-z_1|}][1-\Gamma_2 e^{-\gamma 2|z'-z_2|}]}{[1-\Gamma_1\Gamma_2 e^{-\gamma 2|z_2-z_1|}]} & \text{for } z < z' \end{cases} \tag{2.19}$$

These forms of the TL Green functions are stable for "evanescent-wave" propagation. The asymptotic behavior is immediately apparent from these forms of the equations. Since $\gamma \rightarrow \beta$ as $\beta \rightarrow \infty$, the exponentials become negligible compared to 1 provided the argument distance is nonzero. The reflection coefficients approach constants as $\beta \rightarrow \infty$. The denominator in brackets represents the sum of a geometric series accounting for multiple reflections between the two ends of the line. This form of the TL Green functions is also particularly attractive as it will be shown that they can be written by inspection using Mason's "gain formula" and a very simple signal flow graph.

Figure 2.1 shows the signal flow graph corresponding to $V_I(z,z')$ for the right- and left-traveling voltage waves excited by a unit current source at $z=z'$. The upper branches of the flow graphs usually apply to the right-traveling waves. Similarly, the lower branches apply to the left-traveling waves. The "nodes" of the graph represent the values of the right- and left-traveling waves at various points along the line. The signal value at each node is equal to the sum of the signals that enter it, weighted by the "branch" transfer functions. Thus, to each node corresponds an equation and the graph as a whole provides a pictorial representation of how the system of equations is coupled. The system of equations can be solved readily by simple algebra. Alternatively, those familiar with Mason's gain formula will find that the solution for the TL Green functions can be written by inspection. In Fig. 2.1, the total voltage at any plane (z=constant) is the sum of the right-traveling wave (upper node) and the corresponding left-traveling wave (lower node). Similar signal flow graphs for unit voltage sources or current waves can be used to interpret the other Green functions V_V, I_I, and I_V. The flow graphs for Green functions (2.17), (2.18) and (2.19) are shown in Fig. 2.2, Fig. 2.3, and Fig. 2.4, respectively.

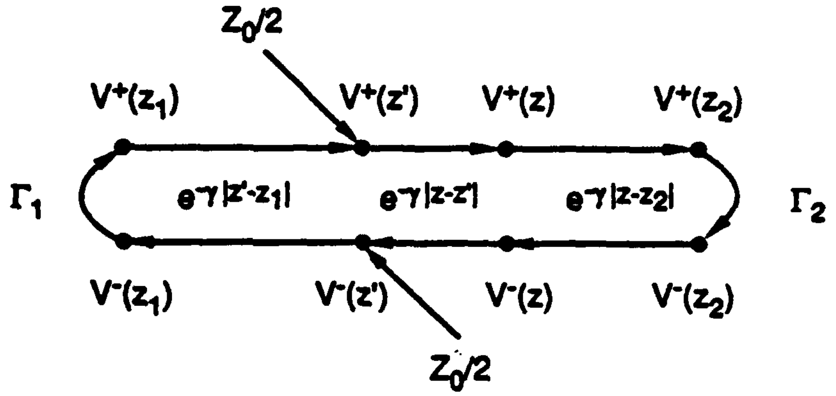

Fig. 2.1 Signal flow graph for Green function $V_I(z,z')$ of Eq. (2.16).

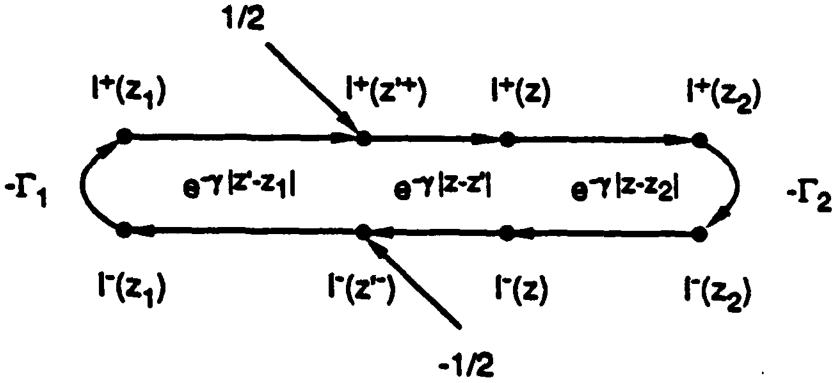

Fig. 2.2 Signal flow graph for Green function $I_I(z,z')$ of Eq. (2.17).

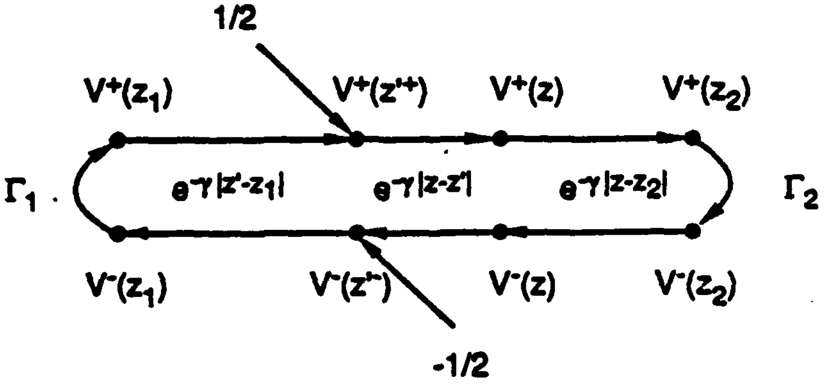

Fig. 2.3 Signal flow graph for Green function $V_V(z,z')$ of Eq. (2.18).

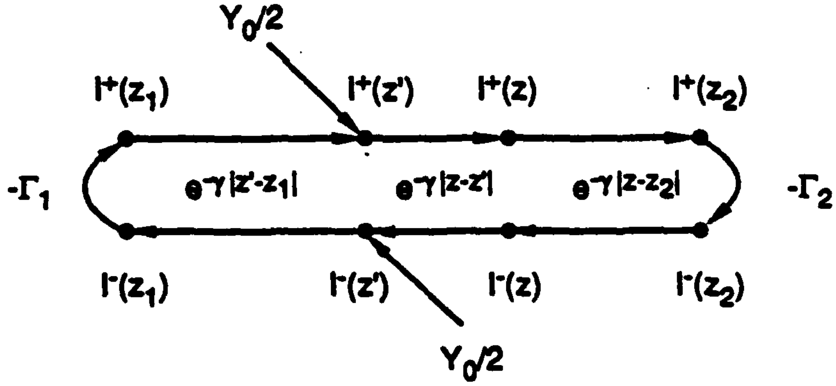

Fig. 2.4 Signal flow graph for Green function $I_V(z,z')$ of Eq. (2.19).

The simplicity of the dyadic Green functions in Table I combined with the TL Green functions should be compared with the method in [6] which requires explicit matching of the fields at each interface.

The previous Green functions were for a uniform line between two bounding reflection coefficients. These Green functions, however, can be used for an arbitrary number of layers provided the following criteria are met:

1) The source and observation points are within the same layer.
2) The reflection coefficients used at each end account for all layers outside of the source-observation layer.

To handle the cases where the source plane and observation plane are in different (homogeneous) layers, the Green functions must be modified. To illustrate the necessary changes, consider the following generalization of (2.18) where the source plane is $z=z_0$ and the observation plane is $z=z_4>z_0$.

$$\begin{aligned} V_V(z_4,z_0) &= \frac{1-\overleftarrow{\Gamma}_0}{2[1-\overleftarrow{\Gamma}_0\overrightarrow{\Gamma}_0]}\, G_{10}\, \frac{1+\overrightarrow{\Gamma}_{1-}}{1+\overrightarrow{\Gamma}_{1+}}\, G_{21}\, \frac{1+\overrightarrow{\Gamma}_{2-}}{1+\overrightarrow{\Gamma}_{2+}}\, G_{32}\, \frac{1+\overrightarrow{\Gamma}_{3-}}{1+\overrightarrow{\Gamma}_{3+}}\, G_{43}\, [1+\overrightarrow{\Gamma}_{4-}] \\ &= \quad V^+_{0+} \quad \frac{V^+_{1-}}{V^+_{0+}}\ \frac{V^+_{1+}}{V^+_{1-}}\ \frac{V^+_{2-}}{V^+_{1+}}\ \frac{V^+_{2+}}{V^+_{2-}}\ \frac{V^+_{3-}}{V^+_{2+}}\ \frac{V^+_{3+}}{V^+_{3-}}\ \frac{V^+_{4-}}{V^+_{3+}}\ \frac{V_4}{V^+_{4-}} \end{aligned} \tag{2.20}$$

The physical interpretation associated with each factor in expression (2.20) is denoted on the second line. The subscripts $_{n+}$ or $_{n-}$ denote the various interface planes $(z=z_n)$ as approached from the right or left, respectively. A superscript $^+$ or $^-$ is used to distinguish between the right- or left-traveling component of the voltage wave, respectively. The reflection coefficients are computed looking in the direction (denoted by the arrows above) away from the source plane $(z=z_0)$. It should be noted that all the reflection coefficients in (2.20) are intermediate results in the computation of the reflection coefficient at the source plane. The "propagator" for an outward traveling wave from plane $(z=z_{n-1})$ to plane $(z=z_n)$ through a homogeneous layer is

$$G_{n,n-1} = e^{-\gamma_{n,n-1}|z_n - z_{n-1}|} \quad n = 1, 2, 3, \cdots \tag{2.21}$$

where

$$\gamma_{n,n-1} = \sqrt{\beta^2 - k^2_{n,n-1}}\,, \qquad -\frac{\pi}{2} < \arg(\gamma_{n,n-1}) \leq \frac{\pi}{2}.$$

Here, a double subscript identifies a homogeneous layer in terms of the two planes that form its boundary.

The other three TL Green functions can obviously be generalized in a similar manner whenever the source plane and observation plane are located within different layers.

2.4. Relationship of Dyadic Green Function to Scalar and Vector Potentials

Another approach often used to formulate the dyadic Green function in a multilayered medium makes use of auxiliary scalar and vector potentials. This approach requires matching the solutions in each region at the interfaces and can be a tedious task unless some sort of cascading procedure is found. An advantage of the scalar and vector potential approach, however, is that the differential operators are in an advantageous position for a method of moments formulation. This is in reference to the procedure whereby the differential operators are transferred to the basis and test functions.

An important result discovered in this report is the connection between the "E- and H-wave, equivalent line" formulation and the "vector and scalar potential" formulation. Consider the transverse electric field due to a transverse electric current. From potential theory it is well known that the electric field can be expressed as

$$E_t = -\nabla_t \Phi - j\,\omega\, A_t \tag{2.22}$$

or equivalently in the transform domain

$$\tilde{E}_t = j\,\overline{\beta}\,\tilde{\Phi} - j\,\omega\,\tilde{A}_t \tag{2.23}$$

where Φ is the scalar potential and A_t is the transverse component of the magnetic vector potential.

From Table I it follows that the transform domain dyadic Green function for the transverse electric field reduces to

$$\tilde{\mathbf{E}}_{\bar{J}}(\bar{\beta},z,z') = -\hat{\beta}\, V_I^E(\beta,z,z')\,\hat{\beta} - \hat{\psi}\, V_I^H(\beta,z,z')\,\hat{\psi} \tag{2.24}$$

The second term of (2.24) can be rewritten in terms of the transform plane identity dyadic.

$$\mathbf{I} = \hat{\beta}\hat{\beta} + \hat{\psi}\hat{\psi} \tag{2.25}$$

Therefore, for a source current sheet $\tilde{\mathbf{J}}_t = \tilde{\mathbf{J}}_s(\xi,\eta)\,\delta(z-z')$, the transverse electric field can be expressed as

$$\tilde{\mathbf{E}}_t = -\bar{\beta}\left\{\frac{V_I^E - V_I^H}{\beta^2}\right\}\bar{\beta}\cdot\tilde{\mathbf{J}}_s - \left\{V_I^H\right\}\tilde{\mathbf{J}}_s \tag{2.26}$$

The two functions in brackets are, respectively, scalar and vector potential Green functions in the transform domain. An advantage of this form is that those familiar with transmission line theory can now just as easily derive "potential Green functions." The space domain, transverse electric field follows by applying the inverse Fourier transform, viz.,

$$\mathbf{E}_t = \nabla_t\, F^{-1}\left\{\frac{V_I^E - V_I^H}{\beta^2}\right\} * \nabla_t\cdot\mathbf{J}_s - F^{-1}\left\{V_I^H\right\} * \mathbf{J}_s \tag{2.27}$$

The inverse Fourier transform operator is denoted by F^{-1}, and * denotes convolution with respect to x and y. This result dramatically shows the connection between the transmission line (TL) Green functions and the scalar and vector potentials for a stratified medium. The asymptotic form of both the scalar and vector potential Green functions in the transform domain is $O(\beta^{-1})$ as $\beta \rightarrow \infty$ which is characteristic of a corresponding $O(r^{-1})$ singularity at the origin in the space domain. It is not a difficult task (and perhaps worthwhile) for the reader to verify that the familiar free-space potential expressions result if the TL Green functions for a homogeneous space are substituted in (2.27). Similarly, a dual result holds for the magnetic field produced by a magnetic current source.

2.5. References

[1] T. Itoh, "Spectral domain immittance approach for dispersion characteristics of generalized printed transmission lines," *IEEE Trans. Microwave Theory Tech.*, vol. MTT-28, pp. 733-736, July 1980.

[2] N. K. Das and D. M. Pozar, "A generalized spectral-domain Green's function for multilayer dielectric substrates with application to multilayer transmission lines," *IEEE Trans. Microwave Theory Tech.*, vol. MTT-35, pp. 326-335, Mar. 1987.

[3] L. B. Felsen and N. Marcuvitz, *Radiation and Scattering of Waves*, Englewood Cliffs, NJ: Prentice-Hall, 1973.

[4] A. D. Yaghjian, "Electric dyadic Green's functions in the source region," *Proc. IEEE*, vol. 68, no. 2, Feb. 1980.

[5] W. A. Johnson, A. Q. Howard and D. G. Dudley, "On the irrotational component of the electric Green's dyadic," *Radio Sci.*, vol. 14, no. 6, pp. 961-967, Nov.-Dec. 1979.

[6] J. A. Kong, *Electromagnetic Wave Theory*. New York: John Wiley & Sons, 1986, pp. 519-524.

3. ANALYSIS OF A RECTANGULAR PATCH FED BY A SLOT LINE

3.1. Description of Antenna and Feed Line

The slot-line fed antenna configuration consists of a rectangular microstrip patch whose x-y dimensions are a and b, respectively, as shown in Fig. 3.1. The patch is situated on a dielectric slab of thickness t in the plane $z=t$ with an underlying ground plane at $z=0$. A slot of width w_s in the ground plane extends under the patch an arbitrary distance in the plane of symmetry $y=b/2$. The left and right ends of the slots are fixed by the points $(x_1, b/2, 0)$ and $(x_2, b/2, 0)$, respectively.

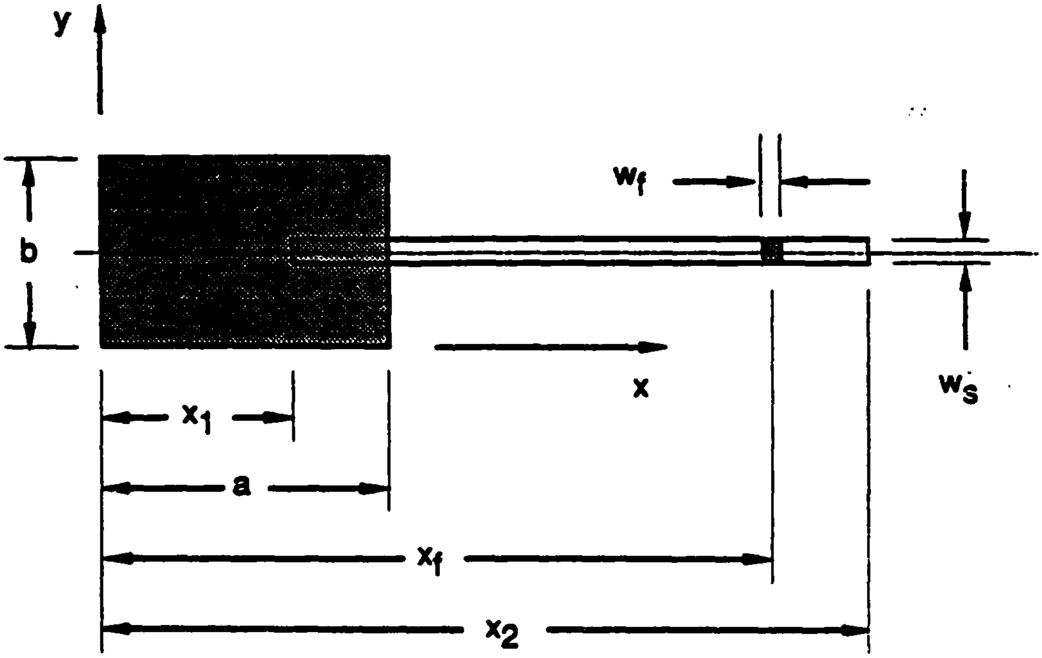

Fig. 3.1 Top view of a rectangular microstrip antenna fed by a slot line in the ground plane.

The slot-line excitation is provided by an electric current strip across the slot at the feed point $(x_f, b/2, 0)$. This current is assumed to be of uniform density over a width w_f and carries 1 A in the y-direction. A major objective is to determine the complex reflection coefficient of the antenna as it appears in the waveguiding medium, in this case, the slot line.

3.2. Problem Formulation

The rigorous analysis of the slot-line fed rectangular patch is first formulated as a set of coupled integral equations. The unknown quantities are the equivalent patch electric surface currents J^X and J^Y and the slot magnetic surface current K^S acting in response to an impressed discontinuity in the slot magnetic field

$$\hat{z} \times [H^+ - H^-] = J^S(x,y) \qquad \text{over slot S} \qquad (3.1)$$

as shown in Fig. 3.1. The unknown sources act in the presence of a translationally invariant grounded-dielectric slab. As the ground plane is approached from either above or below, limits are denoted by a superscript $^+$ or $^-$, respectively. The boundary conditions require the tangential projection of the fields (denoted by an underscore) to satisfy

$$\underline{E}(J^X) + \underline{E}(J^Y) + \underline{E}(K^S) = 0 \qquad \text{over patch P} \qquad (3.2)$$

$$\underline{H}(J^X) + \underline{H}(J^Y) + \underline{H}^+(K^S) + \underline{H}^-(K^S) = -\hat{z} \times J^S \qquad \text{over slot S} \qquad (3.3)$$

where J^S is assumed to be a uniform strip of surface current carrying 1 A across the slot.

$$J^S(x,y) = \hat{y} \begin{cases} 1/w_s & |x - x_f| \le w_f/2, \quad |y - y_s| \le w_s/2 \\ 0 & \text{otherwise} \end{cases} \qquad (3.4)$$

Equations (3.2) and (3.3) represent a coupled pair of integral equations in the unknowns J^X, J^Y and K^S. Moment methods are applied to reduce the integral equations to matrix equations after suitable expansions of the unknown sources are introduced.

$$J^X = \sum_{n=1}^{N_X} I_n^X \, J_n^X \tag{3.5}$$

$$J^Y = \sum_{n=1}^{N_Y} I_n^Y \, J_n^Y \tag{3.6}$$

$$K^S = \sum_{n=1}^{N_S} V_n^S \, K_n^S \tag{3.7}$$

The resulting partitioned matrix equations are

$$\begin{bmatrix} Z^{XX} & Z^{XY} & T^{XS} \\ Z^{YX} & Z^{YY} & T^{YS} \\ T^{SX} & T^{SY} & Y^{SS} \end{bmatrix} \begin{bmatrix} I^X \\ I^Y \\ V^S \end{bmatrix} = \begin{bmatrix} 0 \\ 0 \\ I^S \end{bmatrix} \tag{3.8}$$

where the matrix elements are given by

$$Z_{mn}^{XX} = - < J_m^{X*} \cdot E(J_n^X) > \tag{3.9}$$

$$Z_{mn}^{XY} = - < J_m^{X*} \cdot E(J_n^Y) > \tag{3.10}$$

$$Z_{mn}^{YX} = - < J_m^{Y*} \cdot E(J_n^X) > \tag{3.11}$$

$$Z_{mn}^{YY} = - < J_m^{Y*} \cdot E(J_n^Y) > \tag{3.12}$$

$$T^{XS}_{mn} = -< J^{X*}_m \cdot E(K^S_n) > \tag{3.13}$$

$$T^{YS}_{mn} = -< J^{Y*}_m \cdot E(K^S_n) > \tag{3.14}$$

$$T^{SX}_{mn} = -< K^{S*}_m \cdot H(J^X_n) > \tag{3.15}$$

$$T^{SY}_{mn} = -< K^{S*}_m \cdot H(J^Y_n) > \tag{3.16}$$

$$Y^{SS}_{mn} = -< K^{S*}_m \cdot H^+(K^S_n) > - < K^{S*}_m \cdot H^-(K^S_n) > \tag{3.17}$$

$$I^S_m = < K^{S*}_m \cdot \hat{z} \times J^S > \tag{3.18}$$

and $<(\cdot)> = \int_{-\infty}^{\infty}\int_{-\infty}^{\infty} (\cdot)\, dx\, dy$ for integrable functions when a distribution or generalized function interpretation is not required. For real expansion functions J^X, J^Y and K^S, the reciprocity theorem [1], [2] implies Z^{XX}, Z^{YY} and Y^{SS} are symmetric matrices, $Z^{XY} = (Z^{YX})^T$, $T^{XS} = -(T^{SX})^T$ and $T^{YS} = -(T^{SY})^T$, where superscript ^{T} denotes transpose.

The fields of the expansion currents are found in the Fourier transform domain. The required scalar products for the matrix elements can therefore be defined through the Parseval relation in accord with distribution theory.

$$< J^* \cdot E > = < \tilde{J}^* \cdot \tilde{E} > \tag{3.19}$$

Here the number $<(\cdot)>$ denotes the application of a distribution to a test function and superscript * denotes complex conjugation. When a distribution is generated by a locally integrable function, $<(\cdot)> = \int_{-\infty}^{\infty}\int_{-\infty}^{\infty} (\cdot)\, dx\, dy$ for the space domain and $<(\cdot)> = \int_{-\infty}^{\infty}\int_{-\infty}^{\infty} (\cdot)\, d\xi\, d\eta \,/\, (2\pi)^2$ for the spectral domain, respectively. By convention, the same letter is used to denote a function $F(\cdot)$ and its corresponding distribution F generated by the function F(·). When Fourier integrals exist in the classical sense, the Fourier transform (FT) pair is defined by

$$\tilde{g} = F[g] = \int_{-\infty}^{\infty}\int_{-\infty}^{\infty} g(x, y)\, e^{+j(\xi x + \eta y)}\, dx\, dy \tag{3.20a}$$

$$g = F^{-1}[\tilde{g}] = \frac{1}{(2\pi)^2}\int_{-\infty}^{\infty}\int_{-\infty}^{\infty} \tilde{g}(\xi, \eta)\, e^{-j(\xi x + \eta y)}\, d\xi\, d\eta \tag{3.20b}$$

However, the FT (inverse FT) of a spatial (spectral) distribution is defined by the Parseval relation (3.19). Thus the matrix elements (3.9) through (3.17) are defined by the corresponding spectral integrations.

3.3. Expansion Functions for the Patch and Slot

The expansion functions for the representation of the patch electric current can be either subsectional or entire-domain functions. While subsectional bases provide versatility for representing a wider variety of shapes than the typical rectangular patch, they have the disadvantage of requiring at least on the order of a hundred or more unknowns in the expansion of the patch electric surface current. A more elegant approach is to use an expansion that incorporates more of the known information about the current distribution with the hope of obtaining a representation with fewer unknown coefficients. To this end, the thin cavity model for microstrip antennas suggests an entire-domain expansion for the surface current corresponding to each of the z-independent modes of a thin magnetic-walled cavity. The surface currents associated with the z-independent solenoidal E-modes of the cavity are therefore given by

$$J^{P}_{mn} = -\nabla_t \cos\frac{m\pi x}{a}\cos\frac{n\pi y}{b} \qquad , 0<x<a,\ 0<y<b,$$

$$= \hat{x}\,\frac{m\pi}{a}\sin\frac{m\pi x}{a}\cos\frac{n\pi y}{b} + \hat{y}\,\frac{n\pi}{b}\cos\frac{m\pi x}{a}\sin\frac{n\pi y}{b} \qquad , 0<x<a,\ 0<y<b. \tag{3.21}$$

When a cavity is excited by a slot or aperture, the magnetic field in the cavity also contains an irrotational component. This component is due to the equivalent magnetic surface charge associated with the aperture electric field (magnetic surface current). Such an irrotational magnetic field can be expressed as the gradient of a scalar. The patch surface current associated with an irrotational magnetic mode can therefore be expressed as

$$J^{P'}_{mn} = -\hat{z}\times\nabla_t \sin\frac{m\pi x}{a}\sin\frac{n\pi y}{b} \qquad , 0<x<a,\ 0<y<b,$$

$$= \hat{x}\,\frac{n\pi}{b}\sin\frac{m\pi x}{a}\cos\frac{n\pi y}{b} - \hat{y}\,\frac{m\pi}{a}\cos\frac{m\pi x}{a}\sin\frac{n\pi y}{b} \qquad , 0<x<a,\ 0<y<b. \tag{3.22}$$

It is interesting to note that the surface current corresponding to a solenoidal E-mode contains electric surface charge ($\nabla_t \cdot J^P \neq 0$) while that associated with an irrotational magnetic mode does not ($\nabla_t \cdot J^{P'} = 0$). Also, comparing the x- and y-components of (3.21) and (3.22) shows that they can be considered as linearly independent combinations of the following alternate entire domain basis functions.

$$J^{X}_{mn} = \hat{x}\,\sin\left[\frac{m\pi}{a}\left(x+\frac{a}{2}\right)\right]\cos\left[\frac{n\pi}{b}\left(y+\frac{b}{2}\right)\right] \qquad , |x|<\frac{a}{2},\ |y|<\frac{b}{2}, \tag{3.23}$$

$$J^{Y}_{mn} = \hat{y}\,\cos\left[\frac{m\pi}{a}\left(x+\frac{a}{2}\right)\right]\sin\left[\frac{n\pi}{b}\left(y+\frac{b}{2}\right)\right] \qquad , |x|<\frac{a}{2},\ |y|<\frac{b}{2}. \tag{3.24}$$

For convenience, the origin in (3.23) and (3.24) is taken as the centroid of the patch, and $m = 1,2,3,\cdots$ for J^{X}_{mn}, $m = 0,1,2,\cdots$ for J^{Y}_{mn} and $n = 1,3,5,\cdots$. The even values of n are not required for a slot line along the symmetry axis of the patch. Since an offset slot line does not appear useful at this time, it was felt that symmetry should be used to simplify the analysis and improve the efficiency of the program.

Either set of basis functions, (3.21) and (3.22) or (3.23) and (3.24), can be used to expand the patch electric currents. It was decided, however, that the x-y component approach would be easier to implement since it would involve simpler equations for the matrix elements. An advantage of the other expansion is that it could require fewer unknown coefficients. This is based on the assumption that the patch current due to irrotational-magnetic modes is negligible compared to that associated with the solenoidal modes in the frequency range of interest (i.e., the first few resonances). Early evidence seems to indicate some truth to this hypothesis. However, until more experience is gained with the program it was felt that it would be safer to use the x-y component expansion.

The centered expansion functions (3.23) and (3.24) can readily be shown to have the following Fourier transforms

$$\tilde{J}^{x}_{mn} = \frac{j^{m+n-1}ab}{4}\left[\mathrm{sa}\left(\frac{\xi a+m\pi}{2}\right) - (-1)^{m}\,\mathrm{sa}\left(\frac{\xi a-m\pi}{2}\right)\right] \cdot \left[\mathrm{sa}\left(\frac{\eta b+n\pi}{2}\right) + (-1)^{n}\,\mathrm{sa}\left(\frac{\eta b+n\pi}{2}\right)\right] \tag{3.25}$$

$$\tilde{J}^{Y}_{mn} = \frac{j^{m+n-1}ab}{4}\left[\mathrm{sa}\left(\frac{\xi a+m\pi}{2}\right) + (-1)^{m}\,\mathrm{sa}\left(\frac{\xi a-m\pi}{2}\right)\right] \cdot \left[\mathrm{sa}\left(\frac{\eta b+n\pi}{2}\right) - (-1)^{n}\,\mathrm{sa}\left(\frac{\eta b+n\pi}{2}\right)\right] \tag{3.26}$$

where $\mathrm{sa}(x) = \frac{\sin x}{x}$.

The correct singular edge behavior can also be modeled by replacing the rectangular pulse weighting in (3.23) and (3.24) with a singular weight function. The following transform pair can easily be substituted for this purpose.

$$S(x) = \begin{cases} \dfrac{1}{\pi\sqrt{h^2-x^2}} & , |x| < h, \\ 0 & , \text{otherwise.} \end{cases} \qquad \Leftrightarrow \qquad \tilde{S}(\xi) = J_0(\xi h)$$

The Fourier transforms of the patch currents with singular weighting are the same as (3.25) and (3.26) with sa( ) replaced by $J_0($).

The magnetic current representing the slot line of width w_s is approximated by a subsectional expansion where the m^{th} basis function is

$$K_m^S(x,y) = \hat{x}\, \Lambda\left(\frac{x-x_m}{h_x}\right) \Pi\left(\frac{y-y_s}{w_s}\right) \frac{1}{w_s}\, \delta(z-z_s) \tag{3.27}$$

$$\Pi(x) = \begin{cases} 1, & |x| < 1/2, \\ 0, & \text{otherwise.} \end{cases}$$

$$\Lambda(x) = \begin{cases} 1-|x|, & |x| < 1, \\ 0, & \text{otherwise.} \end{cases}$$

where (x_m, y_s) is the center of the m^{th} basis function, $x_m = x_1 + (m-1)\, h_x$ and h_x is the spacing increment along the slot. Here it is assumed that only the longitudinal component of magnetic current along the slot is of importance. Also, the exact nature of the current distribution across the slot is considered unimportant and replaced with an "equivalent" uniform distribution that stores the same energy per unit length. The "equivalent" uniform width should be chosen approximately 12% wider than the actual slot width for equal quasi-static stored energies. The slot expansion function of (3.27) can readily be shown to have the following Fourier transform

$$\tilde{K}_m^S = \hat{x}\, h_x \left[sa\left(\frac{\xi h_x}{2}\right)\right]^2 sa\left(\frac{\eta w_s}{2}\right) e^{j(\xi x_m + \eta y_s)} \tag{3.28}$$

where $\mathrm{sa}(x) = \frac{\sin x}{x}$. The exponential in (3.28) immediately follows from the shifting theorem.

3.4. Computation of the Matrix Elements

A description of the dyadic Green functions required for this problem is now appropriate. The fields of the patch and slot equivalent currents are formulated in the spectral (transverse wavenumber) domain for each transverse wavevector component. A complete discussion sufficient for this problem can be found in Chapter 2. The problem at hand requires the dyadic Green functions for the transverse field components due to transverse currents which are succinctly summarized below.

$$\bar{\bar{E}}_J(\bar{\beta},z,z') = -\hat{\beta}\, V_I^E(\beta,z,z')\,\hat{\beta} - \hat{\psi}\, V_I^H(\beta,z,z')\,\hat{\psi} \tag{3.29a}$$

$$\bar{\bar{H}}_J(\bar{\beta},z,z') = +\hat{\beta}\, I_I^H(\beta,z,z')\,\hat{\psi} - \hat{\psi}\, I_I^E(\beta,z,z')\,\hat{\beta} \tag{3.29b}$$

$$\bar{\bar{E}}_K(\bar{\beta},z,z') = -\hat{\beta}\, V_V^E(\beta,z,z')\,\hat{\psi} + \hat{\psi}\, V_V^H(\beta,z,z')\,\hat{\beta} \tag{3.29c}$$

$$\bar{\bar{H}}_K(\bar{\beta},z,z') = -\hat{\beta}\, I_V^H(\beta,z,z')\,\hat{\beta} - \hat{\psi}\, I_V^E(\beta,z,z')\,\hat{\psi} \tag{3.29d}$$

The polar coordinates (β, ψ) and unit vectors $(\hat{\beta}, \hat{\psi})$ in the transform plane are defined in terms of the rectangular coordinates (ξ, η) and the unit vectors $(\hat{x}, \hat{y})$.

$$\xi = \beta \cos\psi \qquad \eta = \beta \sin\psi \tag{3.30a}$$

$$\beta = \sqrt{\xi^2 + \eta^2} \qquad \psi = \arctan \eta/\xi \tag{3.30b}$$

$$\hat{\beta} = \hat{x}\cos\psi + \hat{y}\sin\psi \qquad \hat{\psi} = -\hat{x}\sin\psi + \hat{y}\cos\psi \tag{3.30c}$$

$$\bar{\beta} = \hat{\beta}\,\beta = \hat{x}\,\xi + \hat{y}\,\eta \tag{3.30d}$$

The dyadic Green functions (3.29) are formulated in terms of scalar Green functions for equivalent E-wave and H-wave transmission lines. In words, these Green functions are defined as

$V_I(z,z')$ = voltage at z due to a unit current source at z' (3.31a)

$I_I(z,z')$ = current at z due to a unit current source at z' (3.31b)

$V_V(z,z')$ = voltage at z due to a unit voltage source at z' (3.31c)

$I_V(z,z')$ = current at z due to a unit voltage source at z' (3.31d)

where a superscript denotes the E- or H-wave case. Usually the transmission medium is reciprocal; therefore, the TL Green functions satisfy the following reciprocity relationships.

$$V_I(z,z') = V_I(z',z) \qquad (3.32a)$$

$$I_V(z,z') = I_V(z',z) \qquad (3.32b)$$

$$V_V(z,z') = - I_I(z',z) \qquad (3.32c)$$

For the general case of multiple homogeneous dielectric layers, these Green functions are uniquely determined by the equivalent cascaded transmission lines, thickness t_n of the n^{th} layer, and the following parameters associated with the n^{th} layer.

The complex propagation constant

$$\gamma_n = \sqrt{\beta^2 - k^2_n} \qquad -\frac{\pi}{2} < \arg(\gamma_n) \le \frac{\pi}{2}, \qquad (3.33)$$

where $k^2_n = \omega^2\mu_n\varepsilon_n$ is the square of the intrinsic wavenumber of the medium in the n^{th} layer.

The characteristic impedances/admittances for E- and H-waves are

$$Z_n = \frac{1}{Y_n} = \frac{\gamma_n}{j\omega\varepsilon_n} \qquad \text{for E-waves} \qquad (3.34a)$$

$$Z_n = \frac{1}{Y_n} = \frac{j\omega\mu_n}{\gamma_n} \qquad \text{for H-waves.} \qquad (3.34b)$$

The characteristic impedance $Z_n = V^+ / I^+ = - V^- / I^-$ where superscripts $^+$ and $^-$ denote +z and -z traveling-wave components of the total mode voltage V or current I on the equivalent line.

Applying the Parseval relation (3.19) and the dyadic Green functions (3.29) to the previously defined matrix elements (3.9) through (3.17) leads to the formulas in Table II.

Table II

Matrix elements in integral form.

$$Z_{mn}^{XX} = \frac{1}{4\pi^2} \int_0^\infty \left\{ V_I^E \int_{-\pi}^{\pi} \cos^2\psi \, \tilde{J}_m^{X*} \tilde{J}_n^X \, d\psi + V_I^H \int_{-\pi}^{\pi} \sin^2\psi \, \tilde{J}_m^{X*} \tilde{J}_n^X \, d\psi \right\} \beta \, d\beta$$

$$Z_{mn}^{XY} = \frac{1}{4\pi^2} \int_0^\infty (V_I^E - V_I^H) \int_{-\pi}^{\pi} \cos\psi \sin\psi \, \tilde{J}_m^{X*} \tilde{J}_n^Y \, d\psi \;\; \beta \, d\beta$$

$$Z_{mn}^{YY} = \frac{1}{4\pi^2} \int_0^\infty \left\{ V_I^E \int_{-\pi}^{\pi} \sin^2\psi \, \tilde{J}_m^{Y*} \tilde{J}_n^Y \, d\psi + V_I^H \int_{-\pi}^{\pi} \cos^2\psi \, \tilde{J}_m^{Y*} \tilde{J}_n^Y \, d\psi \right\} \beta \, d\beta$$

$$Y_{mn}^{XX} = \frac{1}{4\pi^2} \int_0^\infty \left\{ I_V^H \int_{-\pi}^{\pi} \cos^2\psi \, \tilde{K}_m^{X*} \tilde{K}_n^X \, d\psi + I_V^E \int_{-\pi}^{\pi} \sin^2\psi \, \tilde{K}_m^{X*} \tilde{K}_n^X \, d\psi \right\} \beta \, d\beta$$

$$T_{mn}^{XS} = \frac{1}{4\pi^2} \int_0^\infty (V_V^H - V_V^E) \int_{-\pi}^{\pi} \cos\psi \sin\psi \, \tilde{J}_m^{X*} \tilde{K}_n^X \, d\psi \;\; \beta \, d\beta$$

$$T_{mn}^{YS} = \frac{1}{4\pi^2} \int_0^\infty \left\{ - V_V^E \int_{-\pi}^{\pi} \sin^2\psi \, \tilde{J}_m^{Y*} \tilde{K}_n^X \, d\psi - V_V^H \int_{-\pi}^{\pi} \cos^2\psi \, \tilde{J}_m^{Y*} \tilde{K}_n^X \, d\psi \right\} \beta \, d\beta$$

By exploiting the even and odd symmetries with respect to the rectangular transform variables (ξ, η), the spectral integrations are reduced to the first quadrant of the transform plane. The integration over the first quadrant is performed in polar coordinates with the integration with respect to angle (ψ) being performed first. This approach allows the transmission line (TL) Green functions to be pulled outside the inner integration. This approach greatly improves the efficiency since the TL Green functions are evaluated only once at each spectral (wavenumber) radius. Also, it was found that the angular (inner) integration can be reduced to a real integration by factoring out $(-1)^{n/2}$ where $n=0,1,2,3$. However, the resulting double integrals can be quite time-consuming to compute. Such integrations for sources in the same plane (e.g., matrix elements Z^{YY} and Y^{SS}) are slowly convergent. (They rely on the decay of the source and test function spectra rather than on the decay of the Green function spectrum as the spectral radius increases.) The efficiency of their evaluation can be improved by the methods described in the next chapter.

3.5. Extraction of the Reflection Coefficient from Moment Method Data

The definition of impedance in a moment method formulation is a recurring problem. A unique definition can be found only in a TEM transmission line away from discontinuities. Despite this deficiency, the impedance concept is sometimes useful when the excitation region is electrically small, too close to the antenna, or too complicated to model. In this situation, impedance at the feed point can be defined as

$$Z_{feed} = \frac{-1}{I^2} \int_{feed} \mathbf{E} \cdot \mathbf{J}^S \, da \tag{3.35}$$

where I is the current carried by the impressed current $\mathbf{J}^S$, and $\mathbf{E}$ is the electric field in the feed region found from the solution of the boundary-value problem.

However, a more useful parameter for microwave circuit design is the reflection coefficient associated with the waveguiding structure feeding the antenna. The realization that the reflection coefficient is the desired quantity also circumvents the apparent problem associated with making impedance definitions which are nonunique. In contrast, the reflection coefficient is well defined within a section of translationally invariant guide. Therefore, a rigorous approach is to extract the antenna reflection coefficient from the data without making any impedance definitions. This level of rigor, however, can complicate the numerical solution of the problem if special entire domain standing-wave basis functions [3] are introduced.

An alternative approach to determining the reflection coefficient is to continue to use the subsectional basis functions for a finite section of line long enough to extract the standing-wave-ratio (SWR) on the line between the antenna and feed point. A true indication of the transverse field in the guide is obtained from the magnitude of the coefficients of the basis functions for the guide between the antenna and the feed point. In the moment method model the excitation mechanism is taken to be an impressed electric current across the slot.

The SWR is the ratio of the maximum to minimum amplitude observed in the guide between the antenna and feed point, but far enough from them such that the field is effectively described by a single propagating mode. At the electric field minimum (magnetic field maximum) the true normalized impedance $z_A = 1 / \mathrm{SWR}$ and reflection coefficient $\Gamma_A = (z_A - 1) / (z_A + 1)$. However, the true minimum amplitude can occur between the sample points along the guide. To circumvent the difficulty in obtaining the precise location of the minimum, it is necessary to "curve fit" the traveling wave expression,

$$V(x) = A\, e^{-\gamma x} + B\, e^{+\gamma x}, \tag{3.36}$$

to the sampled data obtained from the moment method solution. If three samples (V(–h), V(0) and V(h)) are obtained with regular spacing h between them, the three constants A, B and γ can be solved for, viz.,

$$\gamma h = \operatorname{arccosh}\left(\frac{V(h) + V(-h)}{2\,V(0)}\right) \tag{3.37}$$

$$A = \frac{1}{2}\left(V(0) - \frac{V(h) - V(-h)}{2 \sinh \gamma h}\right) \tag{3.38a}$$

$$B = \frac{1}{2}\left(V(0) + \frac{V(h) - V(-h)}{2 \sinh \gamma h}\right) \tag{3.38b}$$

The reflection coefficient at the reference plane (x=0) is then given by B/A or A/B if the source is on the left or right, respectively.

Obviously, this method can be used to extract the reflection coefficient in microstrip lines as well. In this case, the axial current along the strip is proportional to the transverse magnetic field. Three samples of the current I(x) yield the propagation constant and the complex amplitudes A and B of the traveling current waves. Therefore, it follows that the voltage reflection coefficient is given by –B/A or –A/B if the source is on the left or right, respectively.

However, to properly measure this reflection coefficient with a modern automated network analyzer (ANA), calibration (with 3 reflection standards) must be performed in the guide. This measurement problem is currently under investigation and is discussed in a later chapter.

3.6. Program Implementation

A Fortran-77 computer program has been written to implement the formulation described above. The program structure is most readily described by the following "flow chart" in outline form.

```
Program MSANT1
Declare Variable Types and Dimension Arrays
Define Statement Functions for Mode Indices
Read Antenna Description File INDATA
Initialize Constants and Common Variables
Fill Excitation Vector (independent of freq.)
Fill Quasi-static Coefficient Vector (independent of freq.)
Beginning of Frequency Stepping Do-Loop
    Fill $Z^{XX}$ Symmetric Block
    Fill $Z^{YY}$ Symmetric Block
    Fill $Z^{XY}$ and $Z^{YX}$ Related Blocks
    Fill $T^{XS}$ and $T^{SX}$ Related Blocks
    Fill $T^{YS}$ and $T^{SY}$ Related Blocks
    Fill a Work Vector and the Toeplitz Block $Y^{SS}$
    Factor the Linear System Matrix into LU Form
    Solve the Factored Linear System
    Compute Feed Pt. Impedance and Refl. Coef.
    Write Normalized Impedance to File ZNDATA
    Write Reflection Coefficient to File SDATA
    Write Warnings and Data As Needed to File OUTDATA
End of Frequency Stepping Do-Loop
Stop
End of Program MSANT1
```

The computation of the matrix elements is performed by the following subroutines:

Subroutine	Interaction Computed
ZJXJX	$-<J^X \cdot E(J^X)>$
ZJYJY	$-<J^Y \cdot E(J^Y)>$
ZJXJY	$-<J^X \cdot E(J^Y)>$
YKXKX	$-<K^X \cdot H(K^X)>$
TJXKX	$-<J^X \cdot E(K^X)>$
TJYKX	$-<J^Y \cdot E(K^X)>$

where $E(\cdot)$ and $H(\cdot)$ denote the electric and magnetic fields of the following source. These subroutines compute the double integral over the first quadrant in the transform plane to yield the matrix elements shown in Table II. The integral is performed in polar coordinates with the angular integral being performed first. The angular integral is divided into panels and performed by a Gaussian quadrature using an eight-point formula for each panel. The division into panels and computation of the integral are done by subroutine CGQ8FG (RGQ8FG for real integrands). The routine uses the least multiple of eight points, greater than or equal to the number of points requested in the integral approximation.

The number of points used in the angular and radial integrals is estimated with the variable DBETA. DBETA represents the maximum allowable sample spacing in the spectral domain according to the usual Nyquist criterion. For example, DBETA is equal to one half the shortest "period" in the spectrum to be integrated. The size of DBETA depends on the spatial support of the sources as well as the relative separation between primary and test sources. DBETA is used to estimate the number of points required to accurately estimate the spectral domain integrals. The approximate number of points required is the length of the integral divided by DBETA. Generally, a safety factor of two times the minimum density of points has been used in all the spectral integrations. As experience is gained with the program, this density may be changed to improve the efficiency.

After the angular integral has been completed, the radial integral is computed in parts between concentric radii. The radial integral is computed using a multiple-point complex Gaussian quadrature (subroutine CGQN) which uses from 2 to 32 points as required. The first interval $(0, k_0)$ extends from the origin to the branch point at BETA = k_0. The second interval $(k_0, k_0+0.2(k_1-k_0))$ passes near a TM_z surface-wave pole which lies just below the real axis in the complex BETA plane, if the realistic dielectric losses are included. For electrically thin substrates, this pole is located at a wavenumber slightly greater than k_0 as shown in Fig. 3.2. In this short interval, to accurately account for surface-wave excitation, either a high-order Gaussian quadrature or convergence enhancement technique (described in Chapter 4) is used. As the electrical thickness of the substrate increases, this pole tends to move toward k_1, possibly entering the next integration interval $(k_0+0.2(k_1-k_0), k_1)$. However, for practical antennas (under 0.1 wavelength in thickness) this extreme pole shift does not occur. For very thick substrates, multiple poles due to higher-order surface-wave modes can exist in the interval (k_0, k_1). It is the program user's responsibility to see that the program is used properly or suitably modified if substrates thicker than 0.1 wavelength are used. In the following interval $(k_1, 5k_1)$ 16 points are used.

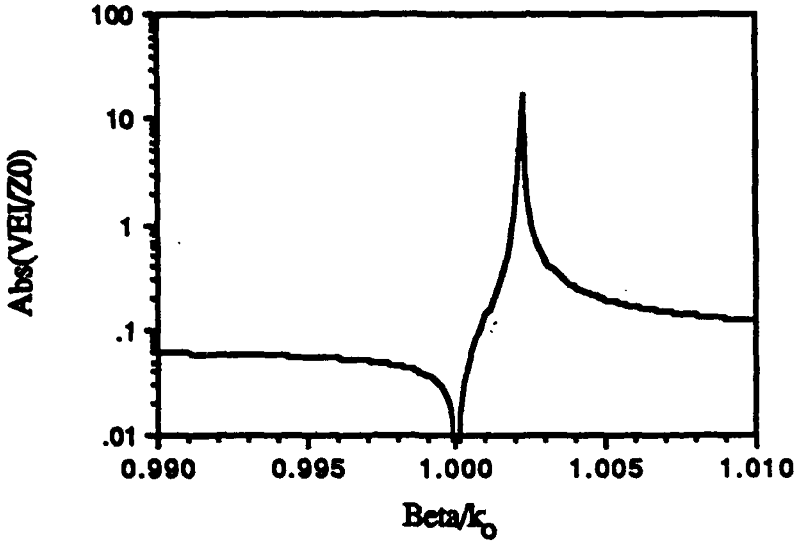

Fig. 3.2 Plot of $|V^{E}_{I}(\beta,t,t) / Z_0|$ as a function of β/k_0 showing the behavior near the surface wave pole ($\beta \approx 1.002\ k_0$) at 3.2 GHz for a substrate of thickness $t_1 = 1.5875$ mm, dielectric constant $\varepsilon_1 = 2.62$, and loss tangent $\tan\delta_1 = 0.001$.

Following the first four intervals, several more intervals are integrated to approximate the integral to infinity. The lengths of these intervals are chosen typically 4*DBETA to 8*DBETA. Convergence is checked by comparing the magnitude of the integral over the last interval to RERR times the magnitude of the total integral. If the last interval contributes more than RERR times the total, integration over an additional interval is performed and again compared to RERR times the new total. The process is repeated until convergence is achieved or a maximum number of intervals is reached. If convergence is not achieved, a warning message (displaying the result after the last two integration intervals) is written to file OUTDATA for that matrix element. Occasionally this warning can appear even though the convergence is acceptable, such as when the coupling between two sources is very small or zero. Also, the last interval covers an increasingly large area (annular region) in the spectral plane as the radius gets larger. The convergence criteria and interval boundaries are clearly documented in the matrix element subroutines and can easily be modified as experience with the program dictates.

To run the program the following steps must be taken:

1. Create an input file DATAIN that describes the antenna dimensions and parameters.

2. In the input file, the user must specify the number of J^X and J^Y modes to be used for the patch. This is accomplished by specifying the last double index (LASTM, LASTN) to be used in the expansion. For efficiency, the last double index can be taken as (0, 1) or (1, 1) for respectively 1 or 3 patch modes when the frequency range desired is not well-defined. The effect of adding several more modes is to increase the matrix fill time approximately as the square of the number of modes. The additional modes slightly alter the resonant frequency, but produce only a slight change in the S_{11} locus about the dominant resonance (TM_{01} mode). It is as if the frequency tick marks slide along the locus; however, the curve itself appears not to change.

3. The density of slot elements should be on the order of 20 per wavelength or more.

4. The frequency range of analysis is specified by variables FSTART and FSTOP. The approximate resonant frequency f'_{01} of the dominant TM_{01} mode due to the slot can be estimated from the following perturbation formula.

$$f'_{01} = f_{01}\sqrt{1 - \frac{\pi s^2}{ab}} \tag{3.39}$$

where ab = the area of the rectangular patch (a by b)
s = distance slot extends under patch
f_{01} = unperturbed resonant frequency

The frequency range is then divided into equal intervals of width (FSTOP - FSTART) / NSTEPS by specifying the parameter NSTEPS.

Numerical results obtained from this program are compared with experimental results in Chapter 6.

3.7. References

[1] R. F. Harrington, *Time-Harmonic Electromagnetic Fields*. New York: McGraw-Hill, 1961.

[2] P. E. Mayes, *Electromagnetics for Engineers*. Ann Arbor, Michigan: Edwards Brothers Inc., 1965.

[3] P. L. Sullivan and D. H. Schaubert, "Analysis of an aperture coupled microstrip antenna," *IEEE Trans. Antennas Propag.*, vol. AP-34, no. 8, Aug. 1986.

4. CONVERGENCE ENHANCEMENT TECHNIQUES

4.1. Integration as the Spectral Radius Approaches Infinity

As shown in the previous chapter, the matrix elements in Table II require double integration over one quadrant of the spectral domain. Since the integration range extends to infinity, care must be taken to assure that convergence is achieved if the domain is truncated to some finite region. Typically, when the observation and source planes are separated ($z \neq z'$), the scalar TL Green functions (3.31) and hence the dyadic Green functions (3.29) exhibit an exponential decay with increasing radial wavenumber β

$$G(\beta,z,z') = O(\beta^n e^{-\beta|z-z'|}) \quad \text{as} \quad \beta \to \infty$$

where $n=-1$ for $G = V_I^H$ or I_V^E; $n=0$ for $G = I_I^E$, I_I^H, V_V^E or V_V^H and $n=1$ for $G = V_I^E$ or I_V^H. However, when the observation and source planes coincide ($z = z'$), the decay is at best algebraic in nature and can even grow. One must then interpret the spectral Green functions as distributions which are defined in terms of space domain distributions. In distribution theory, the transform of a distribution is *defined* by the Parseval relation and not by the Fourier integral (which might not even exist if the integrand is growing as infinity is approached). Thus, the convergence of the integrals in Table II relies heavily on the decay of the FT of the basis-test functions. When the support of the basis-test function is small, the support of its FT is large (the uncertainty principle or principle of reciprocal spreading). Historically, the "relative convergence problem" reported by Mittra, Itoh and Li [1] can be explained merely as a failure to integrate (or sum in the periodic case) over the bulk of the support of the basis-test function in the spectral domain. To enhance the convergence of these spectral integrals, a method combining the singularity subtraction technique with the Parseval relation is developed. The technique is quite general and combines advantages of both spectral and spatial domain formulations in addition to extracting the frequency dependence of the Green function. It is a distribution theory generalization of a procedure used by Richards et al. [2] that combined Kummer's transformation and Poisson's summation formulas for periodic (Floquet) field problems. The procedure is perhaps best illustrated by example.

To illustrate the convergence enhancement technique, consider its application to the evaluation of the matrix elements for the slot line described in Chapter 3. Since the "roof-top" basis functions representing the slot have small spatial support, these matrix elements require the largest domain of spectral integration. From the matrix element definition (3.17), the Parseval relation (3.19) and the dyadic Green function (3.29d), it follows that

$$Y^{SS}_{mn} = < \tilde{K}^{S*}_m \cdot \hat{\beta} \; I^H_V(\beta) \; \hat{\beta} \cdot \tilde{K}^S_n > + < \tilde{K}^{S*}_m \cdot \hat{\psi} \; I^E_V(\beta) \; \hat{\psi} \cdot \tilde{K}^S_n > \tag{4.1}$$

where in this case the TL Green functions must include contributions from the equivalent lines for the regions above and below the ground plane.

$$\begin{aligned} I^H_V(\beta) &= I^H_V(\beta, z{=}0^+, z'{=}0) + I^H_V(\beta, z{=}0^-, z'{=}0) \\ I^E_V(\beta) &= I^E_V(\beta, z{=}0^+, z'{=}0) + I^E_V(\beta, z{=}0^-, z'{=}0) \end{aligned} \tag{4.2}$$

When a distribution in the spectral domain is generated by a locally integrable function, $<(\cdot)> = \int_{-\infty}^{\infty} \int_{-\infty}^{\infty} (\cdot) \, d\xi \, d\eta \, / \, (2\pi)^2$. The first term of (4.1) contains a rather slowly convergent integral as $\beta = \sqrt{\xi^2 + \eta^2} \rightarrow \infty$. The subtraction technique allows (4.1) to be rewritten as

$$\begin{aligned} Y^{SS}_{mn} = &< \tilde{K}^{S*}_m \cdot \bar{\beta} \; [\beta^{-2} I^H_V(\beta) - \bar{A}(\beta)] \; \bar{\beta} \cdot \tilde{K}^S_n > + < \tilde{K}^{S*}_m \cdot \hat{\psi} \; I^E_V(\beta) \; \hat{\psi} \cdot \tilde{K}^S_n > \\ &+ < \tilde{K}^{S*}_m \cdot \bar{\beta} \; \bar{A}(\beta) \; \bar{\beta} \cdot \tilde{K}^S_n > \end{aligned} \tag{4.3}$$

where $\tilde{A}(\beta)$ is an asymptotic expansion of $[\beta^{-2} I_V^H(\beta)]$ as $\beta \rightarrow \infty$. Now applying the Parseval relation (3.19) to the third term of (4.3) yields

$$Y_{mn}^{SS} = < \bar{\tilde{K}}_m^{S*} \cdot \bar{\beta} \; [\beta^{-2} I_V^H(\beta) - \tilde{A}(\beta)] \; \bar{\beta} \cdot \bar{\tilde{K}}_n^S > + < \bar{\tilde{K}}_m^{S*} \cdot \hat{\psi} \; I_V^E(\beta) \; \hat{\psi} \cdot \bar{\tilde{K}}_n^S >$$

$$+ < (\nabla_t \cdot K_m^{S*}), [A * (\nabla_t \cdot K_n^S)] > \tag{4.4}$$

where $A(\rho) = F^{-1}[\tilde{A}(\beta)]$, $\nabla_t \cdot$ denotes the transverse divergence operator, and two-dimensional convolution $f*g(x,y) = \int_{-\infty}^{\infty} \int_{-\infty}^{\infty} f(x-x',y-y') \; g(x',y') \; dx'dy'$. The advantage of (4.4) over (4.1) is that the first term is now more rapidly convergent as $\beta \rightarrow \infty$. Also, the frequency dependence of $A(\rho,z)$ can usually be factored out of the third term of (4.4). Therefore, the integration of the third term need be performed only once when Y_{mn}^{SS} is needed over a range of frequencies. Equation (4.4) concisely illustrates the power of this technique to improve the convergence of the required spectral integrations.

To summarize, the convergence of the required spectral integrations is improved by the subtraction technique. The term which is re-added must have a known spectral integral, or alternatively, can be converted to a more easily computed spatial integral via the Parseval relation. The success of the latter alternative relies on the asymptotic Green function $A(\rho,z) = F^{-1}[\tilde{A}(\beta,z)]$ being known in closed form. Fortunately, this is easily found in all cases for a one-term asymptotic expansion (for this example see Equation (B.2) of Appendix B). Retaining additional higher-order terms allows further convergence enhancement but requires an additional space domain integration for each term in order to factor out the frequency dependence. However, the additional terms contain an excessive singularity in the spectral domain at $\beta=0$. A uniform asymptotic expansion (with respect to β) can be obtained by first expanding with respect to a new variable such as β' where $\beta'^2 = \beta^2 + \tau^2$

and τ is a smoothing parameter. The resulting expansion with the substitution $\beta' = \sqrt{\beta^2 + \tau^2}$ no longer contains a singularity at $\beta=0$ and can be inverse transformed term by term.

4.2. Elimination of Branch-Point Singularities

In addition to the problem that occurs as β approaches ∞, there is always a branch point at $\beta=k_0$ where k_0 is the wavenumber of the last layer (half-space extending to infinity). This is a manifestation of the sign chosen for $\gamma_0 = \sqrt{\beta^2 - k_0^2}$ such that the field in the last layer consists of only outgoing waves. The singularity introduced near such points can be eliminated by making the trigonometric substitution $\beta = k_0 \sin\theta'$ for $\beta < k_0$ and $\beta = k_0 \cosh\theta''$ for $\beta > k_0$. Assuming that $0 < k_0 < \beta_1$, this technique allows the following generic integral to be rewritten in two parts.

$$\int_0^{\beta_1} f(\beta)\, d\beta = \int_0^{\pi/2} f(k_0 \sin\theta')\, k_0 \cos\theta'\, d\theta' + \int_0^{\cosh^{-1}(\beta_1/k_0)} f(k_0 \cosh\theta'')\, k_0 \sinh\theta''\, d\theta'' \tag{4.5}$$

The two transformed integrals no longer contain the singularity associated with the square root function in the expression for γ_0. Therefore, numerical integration can be used to efficiently compute these integrals.

4.3. Integration Near Pole Singularities

Within the integration interval $k_0 < \beta < k_{max}$ where k_{max} is the wavenumber associated with the layer having the largest refractive index, one or more surface-wave poles can exist slightly below the positive real β axis in the complex β plane. For a stratified medium of total thickness $T < \lambda_0/4$, there is usually only one such pole corresponding to an E (or TM to z) type surface wave. The integral can be very time-consuming if done numerically since a very fine sample spacing is required to integrate this highly peaked integrand.

Within an annular region about an isolated pole p, however, the integrand $f(\beta)$ can be approximated by a convergent Laurent series

$$f(\beta) = \frac{c_{-1}}{\beta - p} + c_0 + c_1(\beta - p) + \ldots \tag{4.6}$$

where c_{-1} is known as the residue of $f(\beta)$ at the pole p. Assuming the location of the pole is known, the coefficients c_{-1} and c_0 can also be approximated in terms of the integrand evaluated at two points near the pole. Point matching the first two terms of the Laurent series for $f(\beta)$ at β_1 and β_2 yields the following approximate coefficients.

$$c_{-1} \approx \frac{[f(\beta_1) - f(\beta_2)]\,(\beta_2 - p)\,(\beta_1 - p)}{\beta_2 - \beta_1} \tag{4.7a}$$

$$c_0 \approx \frac{f(\beta_2)(\beta_2 - p) - f(\beta_1)(\beta_1 - p)}{\beta_2 - \beta_1} \tag{4.7b}$$

Now the generic integral $\int_{\beta_1}^{\beta_2} f(\beta)\, d\beta$ can be rewritten in the following form by adding and subtracting the first two terms of the Laurent series for the integrand.

$$\int_{\beta_1}^{\beta_2} f(\beta)\, d\beta = \int_{\beta_1}^{\beta_2} \left(\frac{c_{-1}}{\beta - p} + c_0\right) d\beta + \int_{\beta_1}^{\beta_2} \left(f(\beta) - \frac{c_{-1}}{\beta - p} - c_0\right) d\beta \tag{4.8}$$

The first integral on the right-hand side can be evaluated in closed form yielding

$$\int_{\beta_1}^{\beta_2} f(\beta)\,d\beta = c_{-1}\left[\log_e(\beta - p)\right]_{\beta_1}^{\beta_2} + c_0\left[\beta\right]_{\beta_1}^{\beta_2} + \int_{\beta_1}^{\beta_2}\left(f(\beta) - \frac{c_{-1}}{\beta - p} - c_0\right)d\beta \quad (4.9)$$

For a small interval (β_1, β_2) about the pole p, the first two terms are sufficient to approximate the integral since the third remainder term is $O(|\beta_2 - \beta_1|^2)$. The resulting expression for an interval (not necessarily small) about the pole p is

$$\int_{\beta_1}^{\beta_2} f(\beta)\,d\beta = c_{-1}\left(-j\pi + \log_e\left(\frac{\beta_2 - p}{p - \beta_1}\right)\right) + c_0(\beta_2 - \beta_1) + \int_{\beta_1}^{\beta_2}\left(f(\beta) - \frac{c_{-1}}{\beta - p} - c_0\right)d\beta \quad (4.10)$$

where it is assumed that $\beta_1 < \mathrm{Re}(p) < \beta_2$ and $\mathrm{Im}(p) \leq 0$. Note that this expression is exact even though the coefficients c_{-1}, c_0 and p may be somewhat approximate values.

For electrically thin structures, the situation is complicated by the fact that this pole moves extremely close to the branch point at k_0. The effect of the branch-point singularity at k_0 must be removed by the previous method (Section 4.2) before applying the pole integration technique.

4.4. References

[1] R. Mittra, T. Itoh and T. S. Li, "Analytical and numerical studies of the relative convergence phenomenon arising in the solution of an integral equation by the moment method," *IEEE Trans. Microwave Theory Tech.*, vol. MTT-20, Feb. 1972, pp. 96-104.

[2] W. F. Richards, J. R. Zinecker, D. R. Wilton, S. Singh, Y. T. Lo and S. Wright, "Acceleration of periodic Green's functions in free space," *Program and Abstracts of the URSI 1983 Spring Meeting*, Houston, TX, p. 81.

5. AUTOMATED REFLECTION COEFFICIENT MEASUREMENTS IN AN ARBITRARY WAVEGUIDE

5.1. Three-term Correction of Reflection Measurements

A common problem in automated network analyzer (ANA) measurements is that of calibration in the waveguide of interest. Historically, the calibration problem is directly analogous to that of determining scattering parameters of a waveguide junction, a problem studied by G. A. Deschamps [1] from a geometric point of view. The calibration problem is perhaps most easily described by looking at the following example.

It is desired to make a measurement of the reflection coefficient in a wave guiding medium such as a microstrip transmission line. However, the network analyzer is capable of making a measurement of the reflection coefficient Γ' in the test port guide which is typically a coaxial transmission line. To connect the microstrip guide to the coax requires a transition network. The transition invariably introduces a distortion of the actual reflection coefficient Γ in the microstrip line. The measured reflection coefficient Γ' is related to the actual coefficient Γ in the microstrip by a bilinear transformation [2], [3] involving the scattering parameters of the transition network, viz.,

$$\Gamma' = S_{11} + \frac{S_{12}\,S_{21}\,\Gamma}{1 - S_{22}\,\Gamma} = \frac{S_{11} - \det(S)\,\Gamma}{1 - S_{22}\,\Gamma} \qquad (5.1)$$

where $\det(S) = S_{11}\,S_{22} - S_{12}\,S_{21}$ is the determinant of the scattering matrix.

The essence of the error correction problem is to determine the actual reflection coefficient Γ (at reference plane 2) from the measured value Γ' (at reference plane 1). It is readily apparent that (5.1) can be solved for Γ in terms of Γ' if the S-parameters (S_{11}, S_{22} and $S_{12} = S_{21}$) are known. In other words, the bilinear transformation is easily inverted. This approach to correcting measurements can be extended inside the ANA [4]. This form of error correction treats everything between the microwave bridges (or directional couplers) where the measurement (Γ') is made to the reference plane in the guide of interest as an "effective network." The S-parameters of the "effective network" are usually referred to as "error coefficients":

Directivity Error: $E_D = S_{11}$

Source Match Error: $E_S = S_{22}$

Reflection Tracking Error: $E_R = S_{12}S_{21}$

For further details on the standard calibration procedures, the reader should refer to the Hewlett-Packard (HP) technical notes on ANA calibration [4].

5.2. Calibration Using Offset Reflection Standards

To take advantage of the "error correction" capabilities of a frequency domain ANA requires the use of reflection standards (terminations with a known reflection coefficient). The standards (Γ_n n=1,2,3,...) are connected to the system and the observed values of the reflection coefficients (Γ_n' n=1,2,3,...) are recorded for each frequency of interest. From these data the unknown "error coefficients" can be determined. Some insight can be gained by arranging the data (at a fixed frequency) in matrix form as follows.

$$S_{11} + \Gamma_n' \Gamma_n S_{22} - \Gamma_n \det(S) = \Gamma_n' \tag{5.2}$$

$$\begin{bmatrix} 1 & \Gamma_1' \Gamma_1 & -\Gamma_1 \\ 1 & \Gamma_2' \Gamma_2 & -\Gamma_2 \\ 1 & \Gamma_3' \Gamma_3 & -\Gamma_3 \\ \vdots & \vdots & \vdots \end{bmatrix} \begin{bmatrix} S_{11} \\ S_{22} \\ \det(S) \end{bmatrix} = \begin{bmatrix} \Gamma_1' \\ \Gamma_2' \\ \Gamma_3' \\ \vdots \end{bmatrix} \tag{5.3}$$

The resulting linear system of equations has a unique solution if three equations (i.e., three standards) are used and the system determinant is nonzero. If more than three reliable standards are available that yield consistent data, more equations can be used forming a rectangular system (5.3), denoted more simply as,

$$[R]\,\underline{S} = \underline{\Gamma} \tag{5.4}$$

The rectangular (overdetermined) system can be solved by a least-square technique. This approach produces a solution which is optimal in the sense that the square-norm of the residual vector has been minimized. The least-square solution results from the solution of the equivalent square system (3 by 3) formed by premultiplication by the conjugate-transpose of the rectangular matrix [R].

$$[R^{\dagger}]\,[R]\,\underline{S} = [R^{\dagger}]\,\underline{\Gamma} \tag{5.5}$$

A frequent problem that occurs is that reflection standards are not readily available in the waveguide of interest. The three standards (short-circuit, quasi-open-circuit and matched load) typically used for calibration in a coaxial guide are often not available in waveguides such as microstrip, slot line or coplanar waveguide. When this situation arises, one often has to take advantage of what is available. The one termination that can be made in almost any guide is a "short-circuit" ($\Gamma = -1$). Also, one can use "offsets" of a known reflection or an unknown reflection to obtain some additional information.

Let the reflection coefficient of an "unknown termination" be $\Gamma_?$. Then the reflection coefficient Γ_n of the termination after it has been "offset" by a distance d_n from the reference plane is given by

$$\Gamma_n = G_n \Gamma_? \quad \text{where} \quad G_n = e^{-2\gamma d_n} \tag{5.6}$$

and γ is the complex propagation constant of the guide. This sequence of reflection coefficients can be substituted into the previous system (5.3) to yield

$$\begin{bmatrix} 1 & \Gamma_1' G_1 & -G_1 \\ 1 & \Gamma_2' G_2 & -G_2 \\ 1 & \Gamma_3' G_3 & -G_3 \\ \vdots & \vdots & \vdots \end{bmatrix} \begin{bmatrix} S_{11} \\ \Gamma_? S_{22} \\ \Gamma_? \det(S) \end{bmatrix} = \begin{bmatrix} \Gamma_1' \\ \Gamma_2' \\ \Gamma_3' \\ \vdots \end{bmatrix} \tag{5.7}$$

in terms of the new unknown quantities S_{11}, $\Gamma_? S_{22}$ and $\Gamma_? \det(S)$. Thus, using "offsets" of a repeatable termination allows one to solve for S_{11} and the ratio $S_{22}/\det(S)$ without ever knowing the reflection coefficient $\Gamma_?$. The additional piece of information required can be supplied by using one "known standard" Γ_0 (most likely a short-circuit) and the corresponding measured value Γ_0' which must satisy Equation (5.2). Up to this point, the "error coefficients" have been obtained using offset standards. However, it has tacitly been assumed that the propagation constant γ is a known function of frequency. Generally, the "dispersion relation" is known only in waveguides of homogeneous cross section that fit one of the solvable geometries. Therefore, to actually implement the above method for an arbitrary guide requires a method for extracting the propagation constant as a function of frequency.

5.3. Extraction of the Propagation Constant of an Arbitrary Waveguide for Automated Measurements

To obtain the propagation constant of the guide from single frequency data, the invariance of the "cross-ratio" can be used. Let four different reflection coefficients Γ_n be derived from offsets of an "unknown standard" $\Gamma_?$ as in (5.6), and the corresponding measured (i.e., uncorrected) coefficients be given by Γ_n'. It is a general property of bilinear transformation that the "cross ratio" defined by

$$\frac{(\Gamma_4'-\Gamma_1')(\Gamma_3'-\Gamma_2')}{(\Gamma_4'-\Gamma_2')(\Gamma_3'-\Gamma_1')} = \frac{(\Gamma_4-\Gamma_1)(\Gamma_3-\Gamma_2)}{(\Gamma_4-\Gamma_2)(\Gamma_3-\Gamma_1)} \tag{5.8}$$

is an invariant quantity [2], [3]. The form of this equation is particularly attractive since the "unknown standard" $\Gamma_?$ divides out leaving a single relation involving the measured coefficients Γ_n' and the "propagators" G_n. Rearranging (5.8) in the form of a function $F(\gamma) = 0$ yields

$$F(\gamma) = (\Gamma_4' - \Gamma_1')(\Gamma_3' - \Gamma_2')\left(\frac{G_4}{G_2} - 1\right)\left(\frac{G_3}{G_1} - 1\right) - (\Gamma_4' - \Gamma_2')(\Gamma_3' - \Gamma_1')\left(\frac{G_4}{G_1} - 1\right)\left(\frac{G_3}{G_2} - 1\right) \tag{5.9}$$

The root γ of this equation can be found by a complex generalization of "Newton's method," viz.,

$$\gamma_{i+1} = \gamma_i - \frac{F(\gamma_i)}{F'(\gamma_i)} \qquad i = 0,1,2,... \tag{5.10}$$

$$F'(\gamma) = -(\Gamma_4'-\Gamma_1')(\Gamma_3'-\Gamma_2')\, 2\left\{(d_4-d_2)\frac{G_4}{G_2}\left(\frac{G_3}{G_1} - 1\right) + (d_3-d_1)\frac{G_3}{G_1}\left(\frac{G_4}{G_2} - 1\right)\right\} + (\Gamma_4'-\Gamma_2')(\Gamma_3'-\Gamma_1')\, 2\left\{(d_4-d_1)\frac{G_4}{G_1}\left(\frac{G_3}{G_2} - 1\right) + (d_3-d_2)\frac{G_3}{G_2}\left(\frac{G_4}{G_1} - 1\right)\right\} \tag{5.11}$$

An initial guess for the propagation constant is given by $\gamma_0 = \frac{j\omega}{c\sqrt{\varepsilon_{eff}}}$, where c is the speed of light, $\omega = 2\pi f$ is the radian frequency, and ε_{eff} is an estimate of the "effective permittivity" of the guide. The number of iterations of (5.10) typically required for convergence of the propagation constant is about 3 to 5 for a relative error of 10^{-4}.

After the propagation constant has been computed at the first frequency of the data set, a better initial guess for each succeeding frequency can be computed by scaling. The following scaling formula is exact for nondispersive guides and is a very good approximation in dispersive guides for a small change in frequency.

$$\gamma_0(\omega_{new}) = \frac{\omega_{new}}{\omega_{old}} \gamma_i(\omega_{old}) \tag{5.12}$$

With initial guess (5.12), the number of iterations required for convergence is usually 2 or at most 3 for a relative error of 10^{-4}.

5.4. References

[1] G. A. Deschamps, "Determination of reflection coefficients and insertion loss of a wave-guide junction," *J. Appl. Phys.*, vol. 24, no. 8, pp. 1046-1050, August 1953.

[2] R. V. Churchill, *Introduction to Complex Variables and Applications*, 1st ed. New York: McGraw-Hill, 1948, pp. 57-63.

[3] K. Knopp, *Elements of the Theory of Functions*, Section II. New York, NY: Dover Publications, 1952, pp. 59-62.

[4] *HP 8510 Network Analyzer System Operating and Programming Manual*, Hewlett-Packard Company, Santa Rosa, CA.

6. NUMERICAL AND EXPERIMENTAL RESULTS

Using the computer program developed in Chapter 3, a number of calculations have been performed for a slot-fed, rectangular-microstrip-patch antenna as shown in Fig. 3.1. Table III shows the values of the parameters that define the antenna geometry.

Table III

Parameters for a slot-line fed rectangular microstrip patch antenna.

Patch Dimensions:	$a \times b = 40.0$ mm $\times$ 25.6 mm
Substrate Dielectric Constant:	$\varepsilon_r = 2.62$
Dielectric Loss Tangent:	$\tan \delta = 0.001$
Substrate Thickness:	$t = 1.5875$ mm (1/16 in)
Conductivity of Cladding:	$\sigma = 2.7 \times 10^4$ S/mm
Slot Length:	$l_s = x_2 - x_1 = 30.0$ mm
Slot Width:	$w_s = 0.20$ mm
Distance Slot Extends Under Patch:	$s = a - x_1 = 10.0$ mm
Coordinates of the Feed Point:	$x_f = 50.0$ mm, $y_f = b/2$ = patch center line
Feed Width:	$w_f = 0.4$ mm

These parameters were chosen such that a model antenna could easily be realized to experimentally verify the presented theory.

To verify the convergence of the moment method solution as the number of basis functions is increased, two cases are examined. When applied to such solutions, the term "convergence" is usually understood to mean "numerical convergence," in the sense that the numerical solution approaches a stable solution as the level of discretization is increased. Convergence in the strict mathematical sense will not be proved.

The first case looks at the convergence as the number of patch modes is increased. The results for the input impedance over the frequency range 3.0 – 3.4 GHz (the first resonance of the antenna) are shown in Fig. 6.1. The solid line denotes the input impedance at the feed point for the case with one J_{mn}^{X} mode (m=1; n=1) and two J_{mn}^{Y} modes (m=0,1; n=1). The dashed line denotes the result for four J_{mn}^{X} modes (m=1,2; n=1,3) and six J_{mn}^{Y} modes (m=0,1,2; n=1,3). The results indicate that only a few patch modes are necessary to adequately represent the currents since a threefold increase in the total number of patch modes produces only a slight change in the observed input impedance. The effect of adding several more modes is to increase the matrix fill time approximately as the square of the number of modes. The additional modes slightly alter the resonant frequency, but produce only a slight change in the impedance locus about the dominant resonance (TM_{01} mode). It is as if the frequency tick marks slide along the locus; however, the curve itself changes only slightly. As a compromise between efficiency and accuracy, it appears that three patch modes (J_{01}^{Y}, J_{11}^{X} and J_{11}^{Y}) are sufficient for most purposes.

The second case looks at the convergence as the number of the slot-line subsectional basis functions is increased. The results for the input impedance at the feed point over the frequency range 3.0 - 3.4 GHz are shown in Fig. 6.2. The solid line denotes the input impedance when fourteen K_m^S subsectional basis functions (m=1,...,14) are used along the 30 mm slot. The dashed line denotes the same situation except the number of basis functions K_m^S is increased to 23. The standing-wave patterns along the slot line are shown for 14 and 23 basis functions in Fig. 6.3 and Fig. 6.4, respectively. These results indicate that the number of basis functions should be on the order of 30 per wavelength or more for adequate resolution of the slot-line field.

To independently verify the program, a slot-line fed microstrip patch as shown in Fig. 3.1 was built with the above parameters. For ease of measurement, the excitation of the slot line was in turn provided by a small 50 Ω coaxial cable (Omni Spectra 0.085"

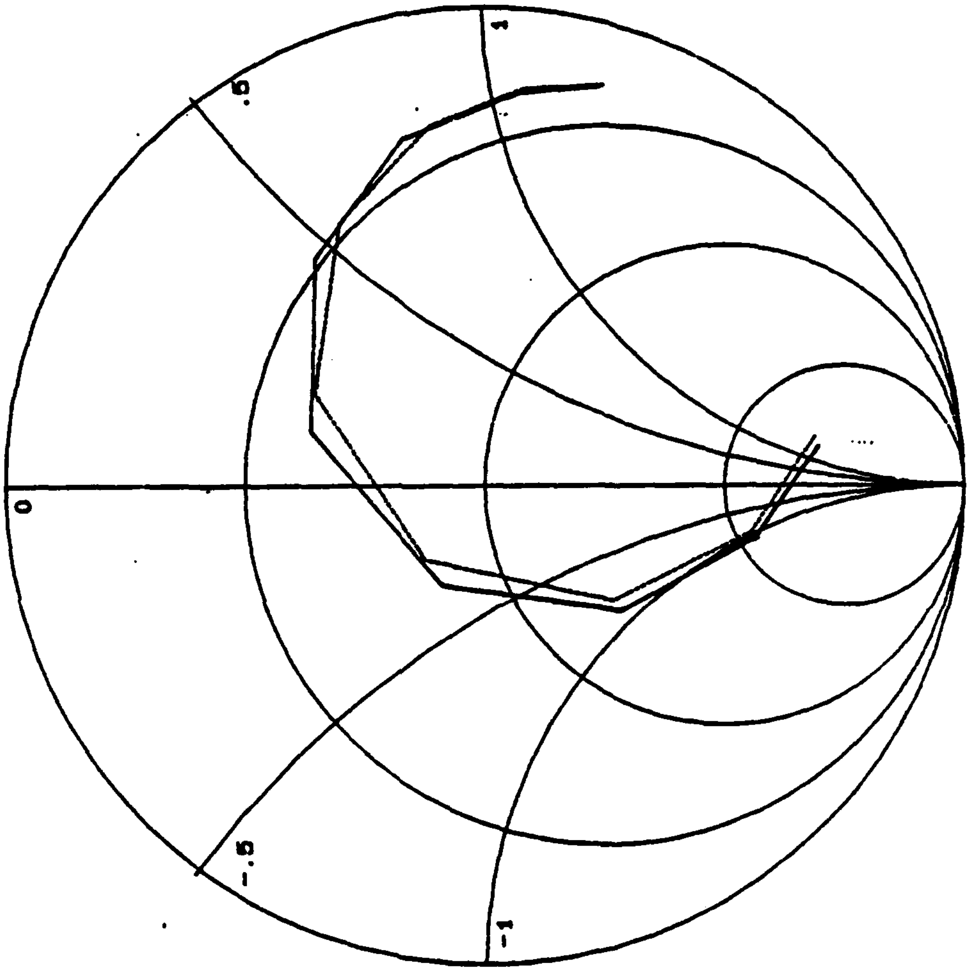

Fig. 6.1 Input impedance of a slot-fed rectangular-patch antenna over the frequency range 3.0 - 3.4 GHz.
Solid line - 3 patch modes. Dashed line - 10 patch modes.

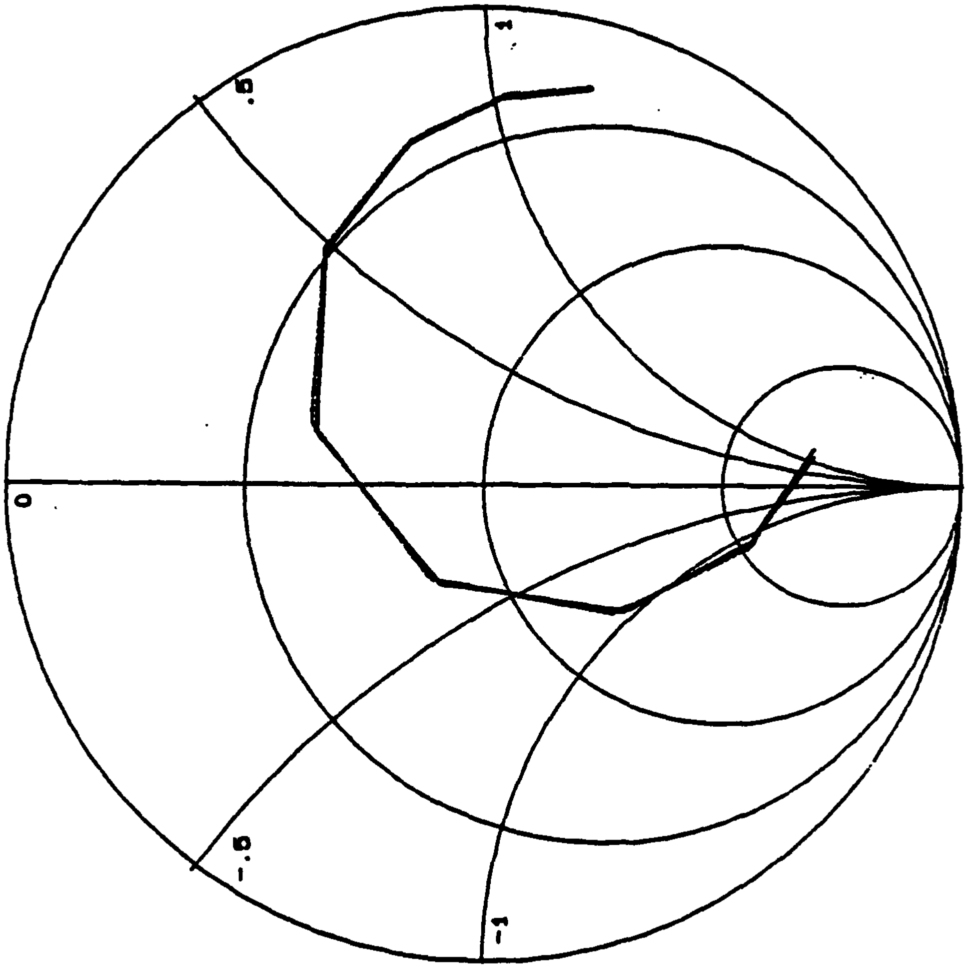

Fig. 6.2 Input impedance of a slot-fed rectangular-patch antenna over the frequency range 3.0 - 3.4 GHz. Solid line - 14 slot basis functions. Dashed line - 23 slot basis functions.

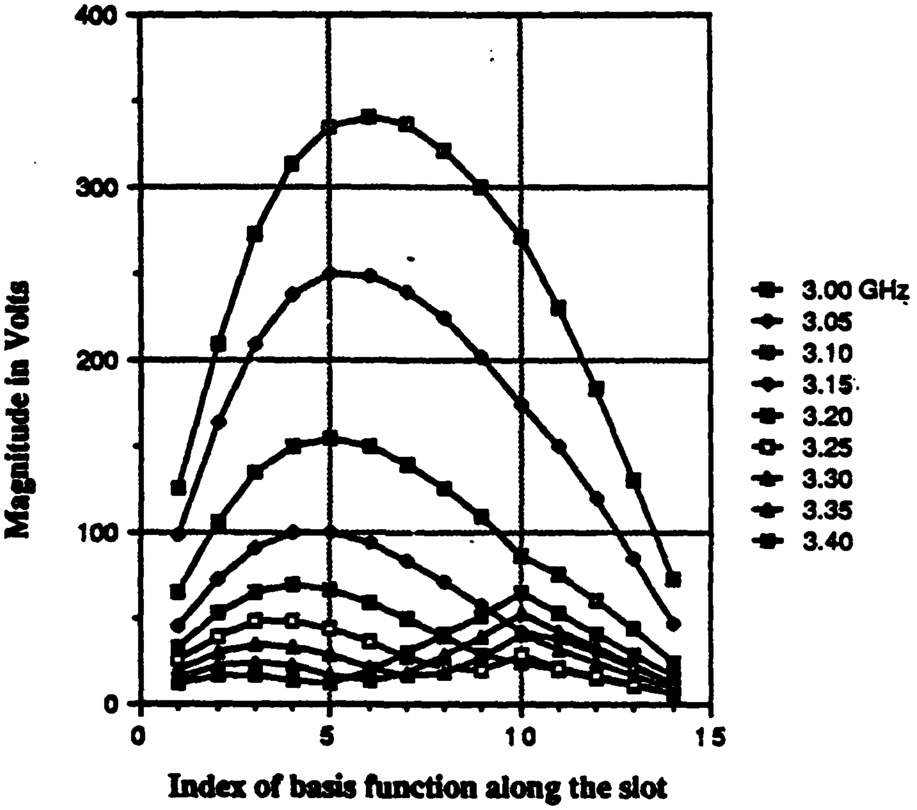

Fig. 6.3 Standing-wave pattern along the slot line for a total of 14 slot-line basis functions over the frequency range 3.0 - 3.4 GHz.

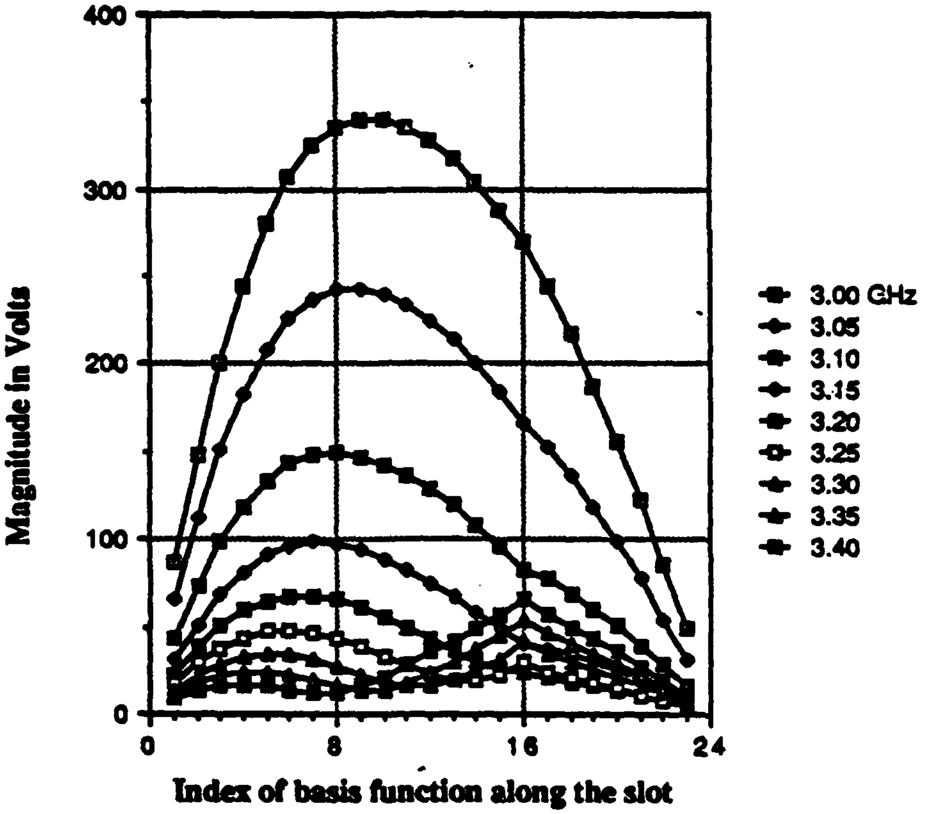

Fig. 6.4 Standing-wave pattern along the slot line for a total of 23 slot-line basis functions over the frequency range 3.0 - 3.4 GHz.

O.D. semirigid). The coaxial center conductor and shield were soldered to each edge of the slot, respectively, at the designated "feed point" (Fig. 3.1).

The reflection measurements were made on an HP8510 automated network analyzer (ANA) with the reference plane adjusted to the end of the coax at the transition to slot line. For the first measurements, only one reflection standard (a short circuit) was available at this plane. In this situation, the measured reflection coefficient Γ' is somewhat contaminated by the effects of the intervening adapters. It should be considered at best as a good approximation to the actual reflection coefficient Γ in the 0.085" cable. The measured coefficient Γ' is related to the actual coefficient Γ by the transformation

$$\Gamma' = S_{11} + \frac{S_{12}\, S_{21}\, \Gamma}{1 - S_{22}\, \Gamma} \tag{6.1}$$

where the S parameters characterize the transition from the test port to the 0.085" cable. Thus, using this approach, the uncertainty in the measurement of Γ is approximately equal to $|S_{11}|$ of the transition (roughly 0.04).

For the second set of measurements much effort was expended to develop reflection standards and software for network analyzer calibration (three-term error model) using the procedure described in Chapter 5. If one is limited to the use of only one-port standards, the only readily available known reflection standards are a "short" and "offset shorts." Using the procedure described in Chapter 5, calibration in the 0.085" coaxial cable was performed using a "short" as a known standard and 4 "quasi-opens" which were identical except for the offset distance. The offsets were chosen to correspond to approximately $\lambda/8$ differential spacing at 3 GHz to assure independence. The results after three-term error correction are compared with the one-term error correction (i.e., extending the reference plane by using electrical delay to correct the phase of a short circuit) in Fig. 6.5 along with the computed data for 3 patch and 14 slot-line basis functions.

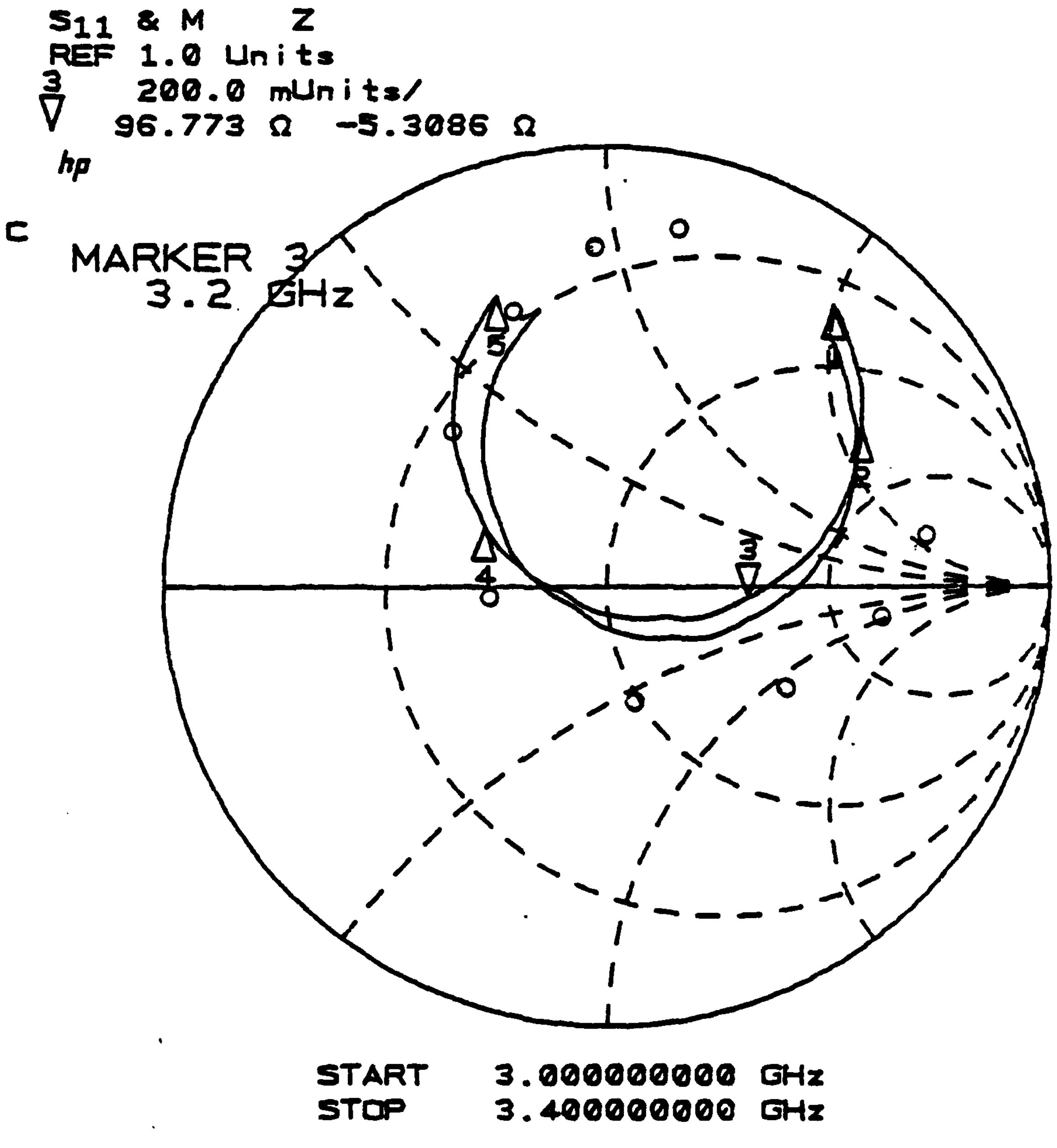

Fig. 6.5 Input impedance of a slot-fed rectangular-patch antenna over the frequency range 3.0 - 3.4 GHz.
Solid line - short only, one-term error correction.
Solid line with markers - three-term error correction.
Circles (O) - computed values at 50 MHz increments.

It is hoped that the three-term error correction can be extended into the slot line. Success requires that enough standards can be found which in turn requires reproducible transitions to the guide of interest and reproducible line sections to realize the reference plane "offsets". Experiments thus far have been successful in measuring the reflection coefficient with three-term error correction in small coaxial lines and also microstrip lines. However, it has been difficult to reproduce narrow slot lines which are considered desirable for minimal radiation losses.

For the design of the antenna feed system, the antenna reflection coefficient in the slot line is more useful than the feed point impedance defined by Equation (3.35). To compute this quantity requires the analysis of the antenna fed by a line long enough to easily extract this information. The following case has parameters as described in Table III except that the slot length has been increased to 80.0 mm. As in the previous case, the slot extends 10.0 mm under the patch. The standing-wave pattern along the slot line is shown in Fig. 6.6 and Fig. 6.7 for 39 slot basis functions and 3 patch modes over the frequency range from 3.00 to 3.40 GHz. These curves clearly show a standing-wave pattern that is characteristic of a single-mode interaction away from the feed point and patch edge. As the frequency is increased the standing-wave ratio (SWR) first decreases, reaching a minimum at 3.25 GHz, and then increases.

The slot line does not appear to be well matched to the antenna since the minimum SWR attained is about 5. The high impedance point of the standing-wave pattern near the patch edge suggests that the SWR can be decreased by reducing the distance that the slot extends under the patch. Figure 6.8 and Fig. 6.9 show the standing-wave patterns when the slot extends 8.0 mm under the patch. Similarly, allowing the slot to extend only 6.0 mm under the patch yields the standing-wave patterns shown in Fig. 6.10 and Fig. 6.11. As expected, reducing the slot length under the patch improved the "match" between the antenna and the slot line. In Figure 6.11, the standing-wave pattern at 3.35 GHz indicates that very little energy (approximately 0.5 %) is reflected by the antenna.

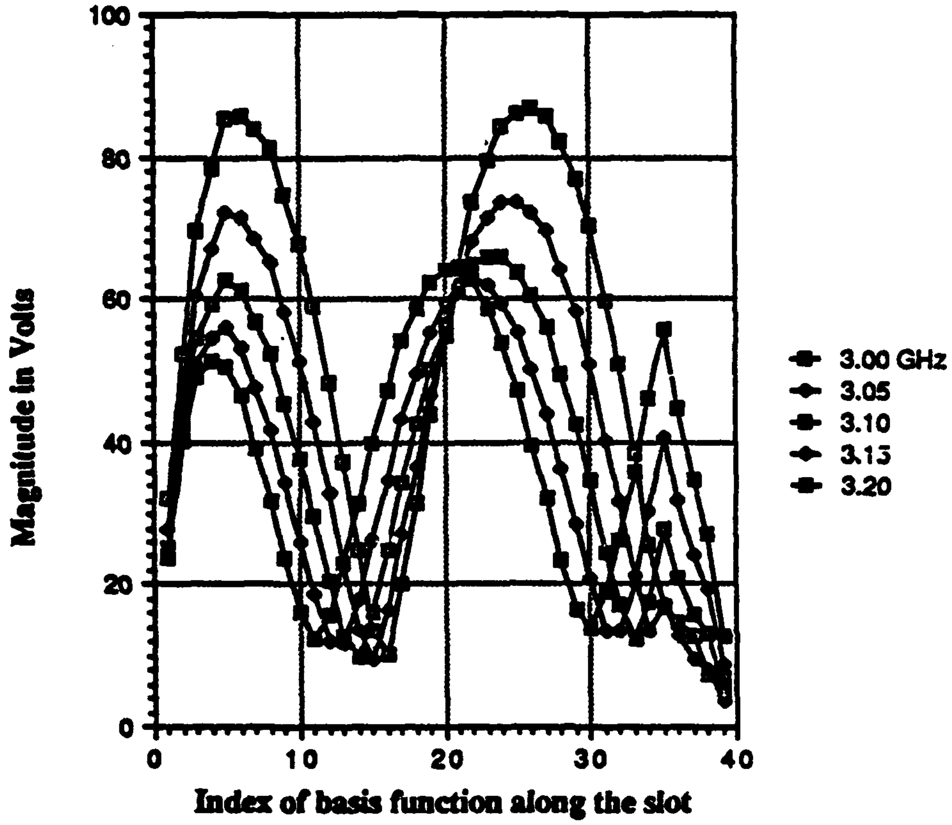

Fig. 6.6 Standing-wave pattern along an 80.0 mm slot line with 39 basis functions over the frequency range 3.00 - 3.20 GHz. Slot line extends 10.0 mm under the patch. The feed point is located at the 35th basis function.

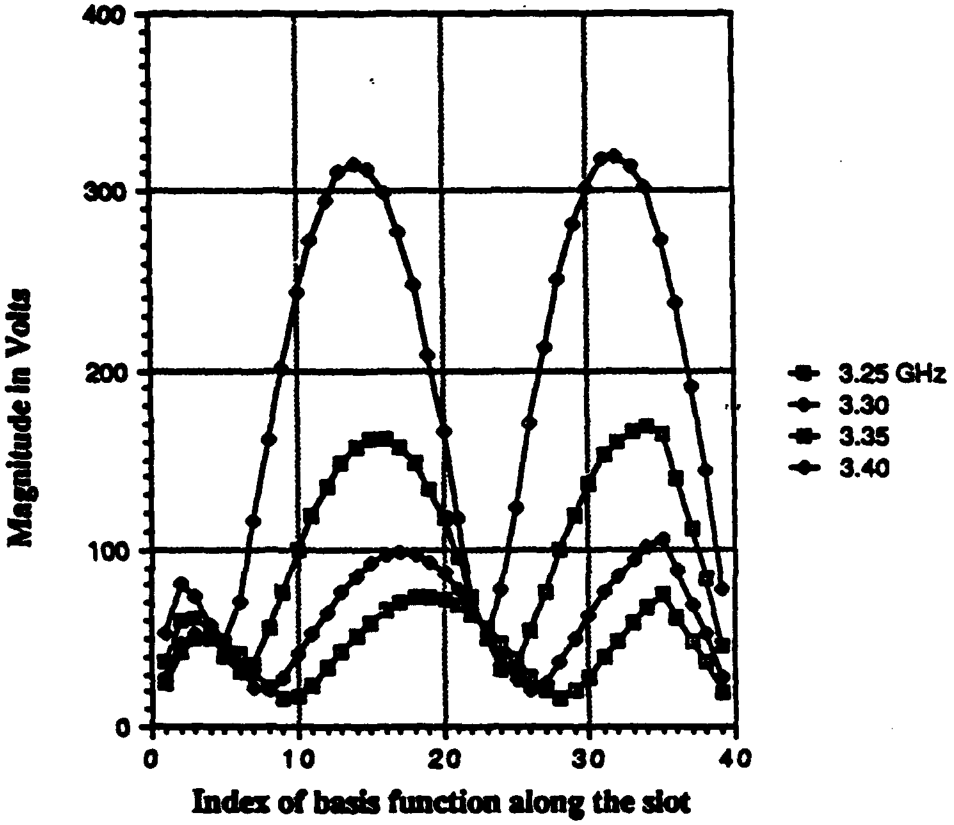

Fig. 6.7 Standing-wave pattern along an 80.0 mm slot line with 39 basis functions over the frequency range 3.25 - 3.40 GHz. Slot line extends 10.0 mm under the patch. The feed point is located at the 35th basis function.

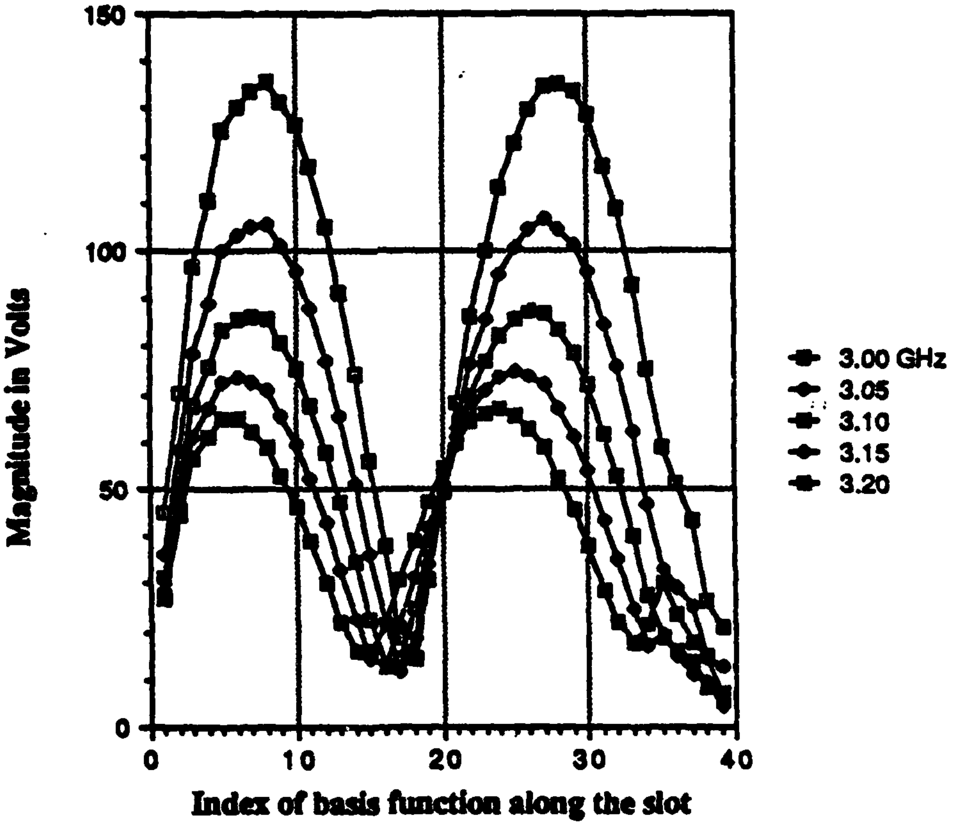

Fig. 6.8 Standing-wave pattern along an 80.0 mm slot line with 39 basis functions over the frequency range 3.00 - 3.20 GHz. Slot line extends 8.0 mm under the patch. The feed point is located at the 35th basis function.

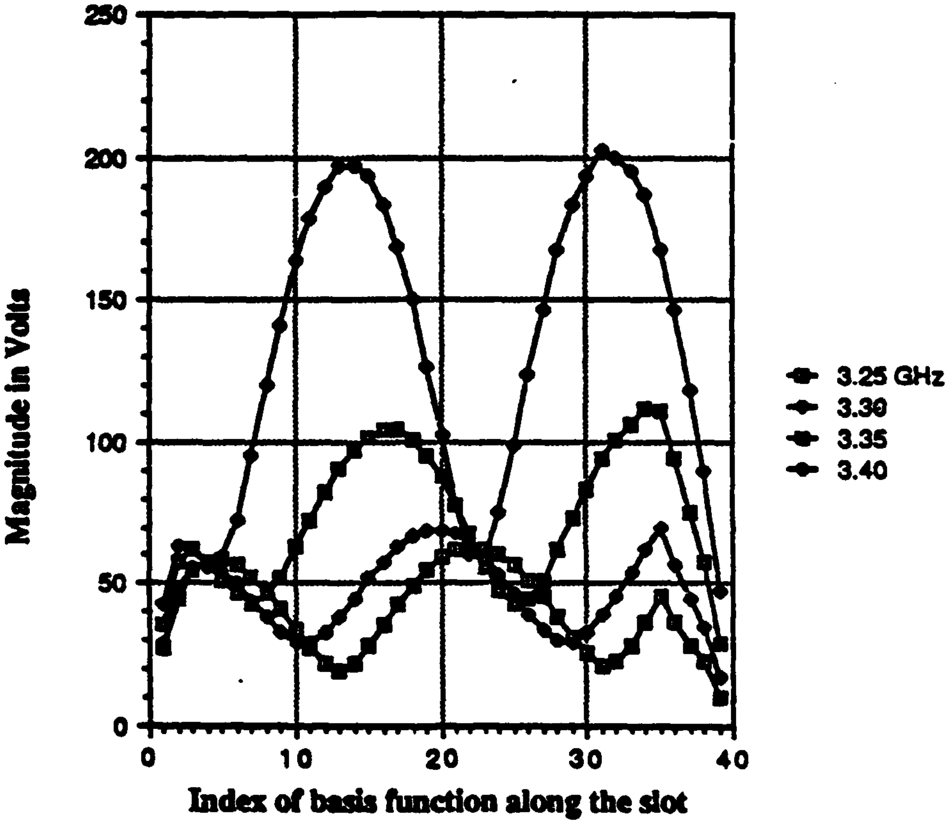

Fig. 6.9 Standing-wave pattern along an 80.0 mm slot line with 39 basis functions over the frequency range 3.25 - 3.40 GHz. Slot line extends 8.0 mm under the patch. The feed point is located at the 35th basis function.

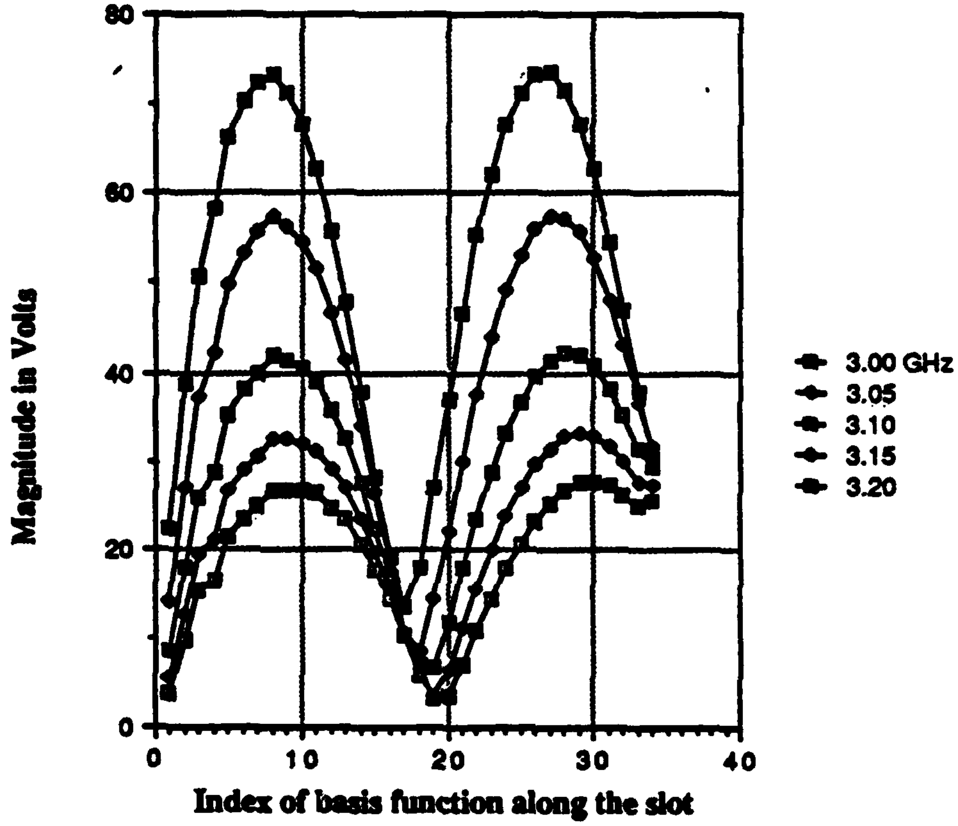

Fig. 6.10 Standing-wave pattern along an 70.0 mm slot line with 34 basis functions over the frequency range 3.00 - 3.20 GHz. Slot line extends 6.0 mm under the patch. The feed point is located at the 34th basis function.

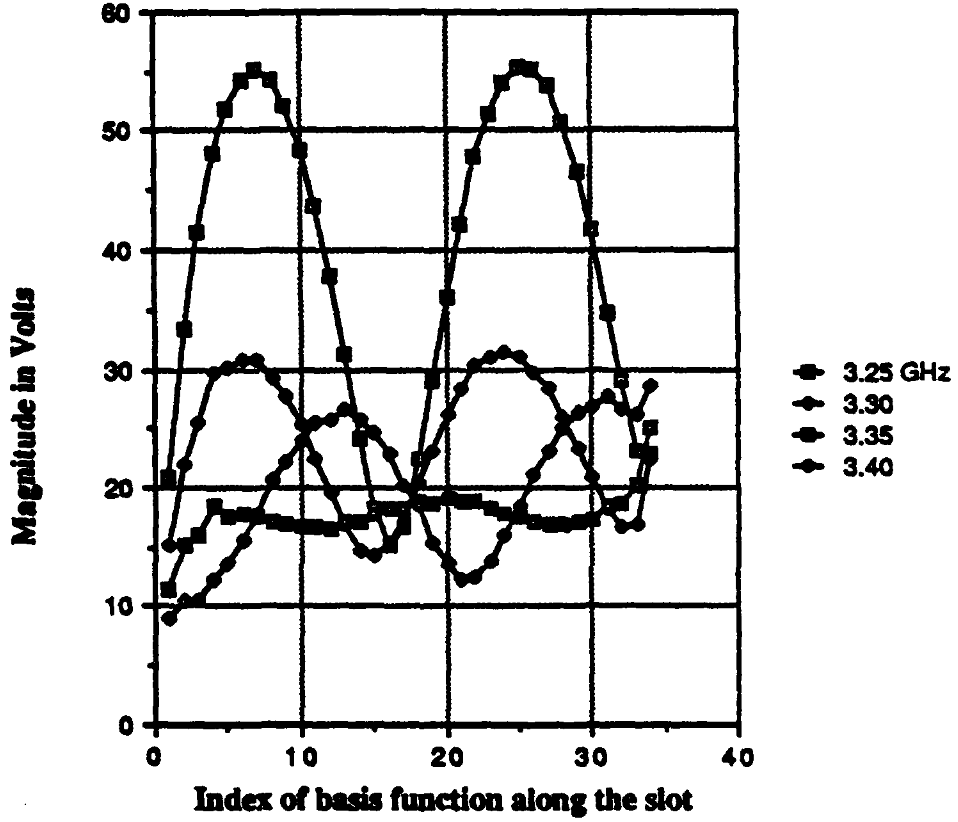

Fig. 6.11 Standing-wave pattern along an 70.0 mm slot line with 34 basis functions over the frequency range 3.25 - 3.40 GHz. Slot line extends 6.0 mm under the patch. The feed point is located at the 34th basis function.

Figure 6.12 summarizes the behavior of the SWR versus frequency for slot lines extending 6, 8 and 10 mm under the patch.

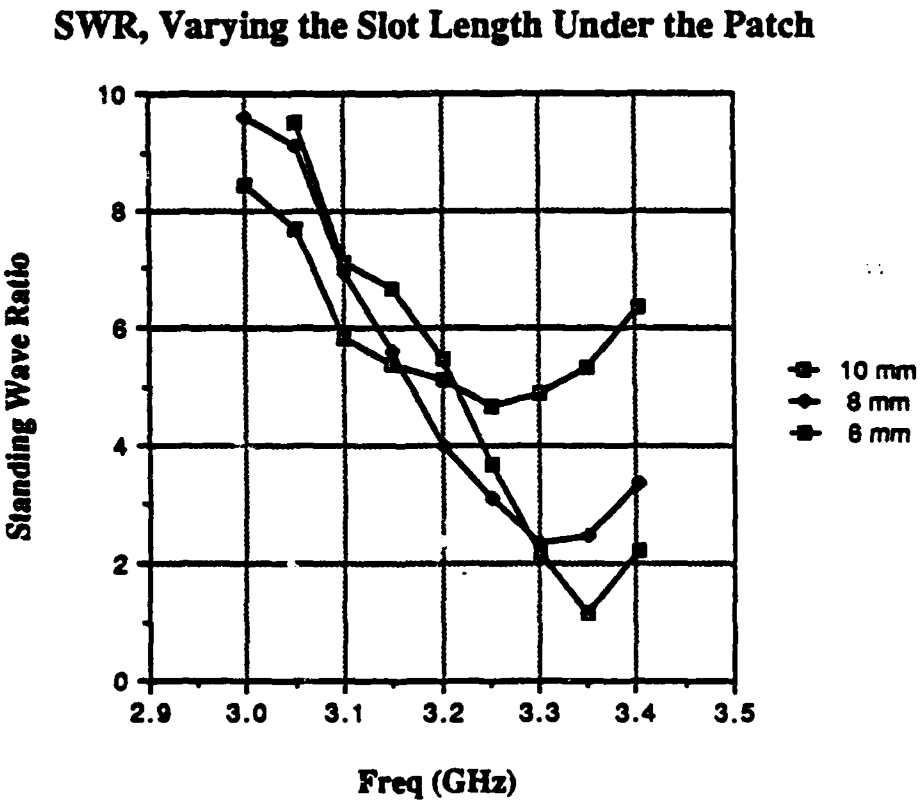

Fig. 6.12 Standing-wave ratio versus frequency for various slot-line extensions under the patch.

7. CONCLUSIONS

In summary, this report describes some important numerical methods for modeling microwave integrated circuits and antennas. The theory for dyadic Green functions in stratified media was derived in the spectral domain. The straightforward use of these Green functions inevitably involves the evaluation of slowly convergent integrals as the spectral radius increases. The slow decay or lack of decay in the transform domain Green functions is a direct result of the transform domain representation of corresponding differential operations in the space domain. The recognition of the space domain differential operations from the corresponding transform domain representation is of paramount importance. It is necessary to improve the convergence of, or even attach a meaning to, some of the spectral domain integrals. The convergence enhancement techniques described in Chapter 4 are useful to reduce the various improper integrals often encountered to ordinary integrals which are amenable to efficient numerical integration on the computer.

A slot-line fed rectangular microstrip patch antenna was analyzed with the above theory. The antenna configuration is an attractive candidate for use in monolithic arrays which incorporate active devices such as amplifiers and phase shifters. Computed and experimental results were compared and found to be in reasonably good agreement. Adjusting the extention of the slot line under the patch was found to be an effective method for matching the slot line to the patch.

The difficulty in obtaining measurements of the reflection coefficient in the guide of interest has led to the investigation of more sophisticated measurement and error correction techniques. Further work and some new approaches are planned in this area. Also, improved fabrication techniques are needed to reproduce slot lines and transitions within the tolerances required.

APPENDIX A: THE STATIC INTERACTION BETWEEN TWO SURFACE CHARGE PULSES

The purpose of this appendix is to compute the following singular integral for the interaction of two rectangular surface charge pulses. This formula is then used for the quasi-static interaction between two "rooftop" magnetic currents.

Consider the rectangular pulse of unit moment

$$P(x,y) = \begin{cases} (ab)^{-1}, & |x| < a/2, \ |y| < b/2 \\ 0, & \text{otherwise.} \end{cases} \tag{A.1}$$

In the moment method it is desired to compute the scalar potential of a surface charge pulse. This scalar potential is then evaluated at the centroid of a second pulse. A further improvement in the satisfaction of the boundary conditions can be obtained by averaging the scalar potential of the first pulse over the second pulse. This process produces in essence a double average of the scalar Green function (R^{-1}) over the first and second pulse. Since the double average of the scalar Green function also has inverse length units, it is convenient to define the *average inverse distance function* D^{-1}. The average inverse distance function depends only on the relative separation of the two surface charge pulses. It can be expressed as a double convolution $D^{-1} = P * R^{-1} * P$. If the surface charge pulses are in the same (z = constant) plane, this formula simplifies with $R(x,y) = \sqrt{x^2 + y^2}$ and * becomes two-dimensional convolution.

Making use of the identity

$$\left(\frac{\partial^2}{\partial x^2} + \frac{\partial^2}{\partial y^2}\right) R(x,y) = R^{-1}(x,y) \tag{A.2}$$

along with the associative and derivative properties of convolution yields

$$\begin{aligned} D^{-1} &= (P * P) * \left(\frac{\partial^2}{\partial x^2} + \frac{\partial^2}{\partial y^2}\right) R \\ &= R * \frac{\partial^2}{\partial x^2}(P * P) + R * \frac{\partial^2}{\partial y^2}(P * P) \end{aligned} \qquad \text{(A.3)}$$

where

$$P * P = \begin{cases} (a - |x|)\,(b - |y|)\,(ab)^{-2}, & |x| < a,\ |y| < b, \\ 0, & \text{otherwise,} \end{cases} \qquad \text{(A.4)}$$

$$\frac{\partial^2}{\partial x^2}(P*P) = \begin{cases} [\delta(x+a) - 2\,\delta(x) + \delta(x-a)]\,(b - |y|)\,(ab)^{-2}, & |y| < b, \\ 0, & \text{otherwise,} \end{cases} \qquad \text{(A.5)}$$

$$\frac{\partial^2}{\partial y^2}(P*P) = \begin{cases} (a - |x|)\,[\delta(y+b) - 2\,\delta(y) + \delta(y-b)]\,(ab)^{-2}, & |x| < a, \\ 0, & \text{otherwise.} \end{cases} \qquad \text{(A.6)}$$

Therefore, to compute (A.3), consider the following elementary integral,

$$I(x,y,a) = R(x,y) * X(x)\,\delta(y) \qquad \text{(A.7)}$$

where

$$X(x) = \begin{cases} a - |x|, & |x| < a, \\ 0, & \text{otherwise.} \end{cases}$$

The convolution integral (A.7) can be expressed as

$$I(x,y,a) = (a-x) \int_{x-a}^{x} R(u,y)\,du + \int_{x-a}^{x} u\,R(u,y)\,du$$
$$+ (a+x) \int_{x}^{x+a} R(u,y)\,du - \int_{x}^{x+a} u\,R(u,y)\,du \qquad (A.8)$$

The following indefinite integrals are required to evaluate (A.8)

$$\int x\,R(x,y)\,dx = R^3(x,y) / 3 \qquad (A.9)$$

$$\int R(x,y)\,dx = F(x,y) \qquad (A.10)$$

where $F(x,y) = \frac{1}{2}\left\{ x\,R(x,y) + y^2 \operatorname{arcsinh}\left(\frac{x}{|y|}\right) \right\}$

Thus, integral (A.7) evaluates to

$$I(x,y,a) = (a+x)\,[F(x+a,y) - F(x,y)] + (a-x)\,[F(x,y) - F(x-a,y)]$$
$$-\frac{1}{3}\left[R^3(x+a,y) - 2\,R^3(x,y) + R^3(x-a,y)\right] \qquad (A.11)$$

This integral is an even function of x and y. The function D^{-1} is easily found by combining (A.3), (A.5), (A.6) and (A.11) which yields the following result.

$$D^{-1}(x,y,a,b) = \{\, I(x,y+b,a) - 2\,I(x,y,a) + I(x,y-b,a)$$
$$+ I(y,x+a,b) - 2\,I(y,x,b) + I(y,x-a,b) \,\}\,(ab)^{-2} \qquad (A.12)$$

To check this result, note that this integral should approach R^{-1} when $\sqrt{a^2 + b^2} << \sqrt{x^2 + y^2} = R(x,y)$. The average inverse distance function D^{-1} for the case of two square (a=b=1) pulses and the function R^{-1} are plotted versus x for y=0 in Fig. A.1.

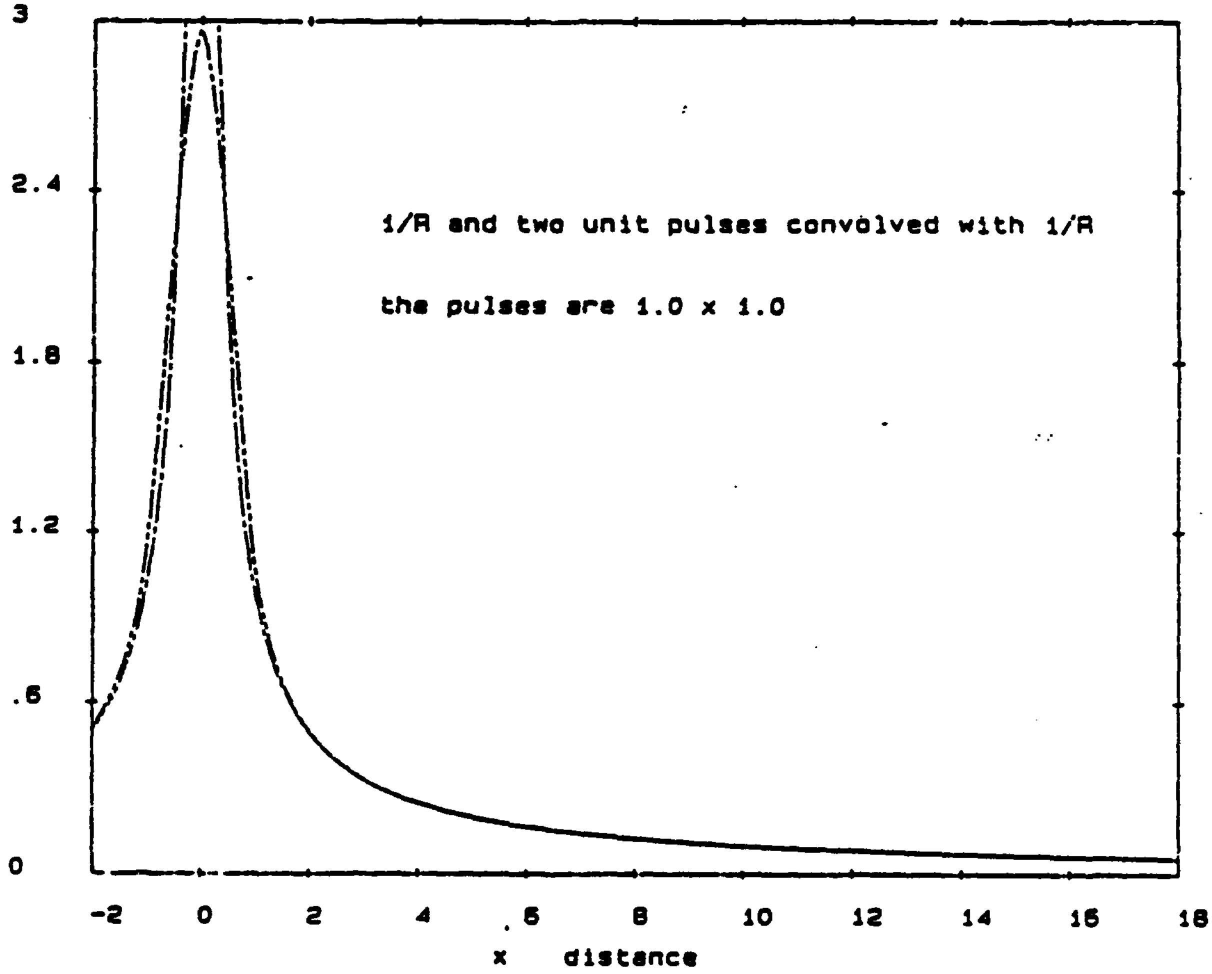

Fig. A.1. Plot of $R^{-1}(x,y)$ and $D^{-1}(x,y) = P * R^{-1} * P$ versus x for $y = 0$.

APPENDIX B: THE QUASI-STATIC INTERACTION BETWEEN TWO "ROOFTOP" CURRENT ELEMENTS

The static interaction between two rectangular pulses can now be applied to the computation of the quasi-static interaction between two "rooftop" basis-test functions used to model the slot line. The quasi-static approximation to the mutual admittance for two x-directed magnetic currents is given by

$$Y^{XX}_{mn} = \langle \nabla_t \cdot K^X_m \; A * \nabla_t \cdot K^X_n \rangle \tag{B.1}$$

where the quasi-static Green function involving the permeability immediately above and below the ground plane is

$$A(R) = \left(\frac{1}{\mu^+} + \frac{1}{\mu^-} \right) \frac{1}{j\omega \, 2\pi R} \tag{B.2}$$

$$K^X_m(x,y) = K^X(x-x_m, y-y_m) \tag{B.3}$$

$$K^X(x,y) = \begin{cases} (h_x - |x|) / (h_x h_y), & |x| < h_x, \ |y| < h_y/2 \\ 0, & \text{otherwise,} \end{cases} \tag{B.4}$$

$$\nabla_t \cdot K^X(x,y) = \begin{cases} -1 / (h_x h_y), & 0 < x < h_x, \ |y| < h_y/2 \\ +1 / (h_x h_y), & -h_x < x < 0, \ |y| < h_y/2 \\ 0, & \text{otherwise.} \end{cases} \tag{B.5}$$

From (B.5) each "rooftop" function is seen to consist of two charge domains. Therefore, the interaction (B.1) can be computed by applying the previously derived integral (A.12).

$$Y_{mn}^{xx} = \{ 2\,D^{-1}(x, y, h_x, h_y) - D^{-1}(x+h_x, y, h_x, h_y) - D^{-1}(x-h_x, y, h_x, h_y) \} \frac{1}{j\omega 2\pi}\left(\frac{1}{\mu^{+}} + \frac{1}{\mu^{-}}\right) \tag{B.6}$$

where the separation between the basis functions is $x = x_m - x_n$ and $y = y_m - y_n$.

VITA

David Robert Tanner was born in Muscatine, Iowa, on December 22, 1956. He attended the Thornton Community College of South Holland, Illinois, where he received the A.S. degree in engineering in 1977 along with awards for outstanding achievement in Physics and Mathematics. He completed his undergraduate education at the University of Illinois at Urbana-Champaign. Graduating in 1979 with high honors, he received the B.S. degree in electrical engineering.

David entered the graduate program at the University of Illinois and joined the Aeronomy Laboratory. As a research assistant he studied the use of high power VHF radar for probing the ionosphere. His research involved the design of a new "coherent-scatter" VHF radar antenna which was to be the largest of its kind (10^5 m^2) in the United States. He completed the M.S. degree in electrical engineering in January 1983, and was the recipient of the ninth annual Schlumberger Foundation fellowship. His interest in electromagnetics and antennas compelled him to pursue the Ph.D. degree with the University of Illinois, Electromagnetics Laboratory. As a research assistant, his interests have been in electromagnetic theory and the design of broad-band and phased-array antennas. He worked on the numerical modeling of low profile, cavity-backed slot and microstrip antennas and received the Doctor of Philosophy degree in January 1988. His current research interests include precision microwave measurements, radar cross section of antennas, remote sensing and the application of supercomputers to electromagnetic modeling. He is a member of Eta Kappa Nu and the Institute of Electrical and Electronics Engineers.

Part II.

A Study of Feeding Networks for Microstrip Antennas and Arrays Integrated with Amplifiers

by

P. Aoyagi, Y. T. Lo and S. L. Chuang

TABLE OF CONTENTS

CHAPTER 1

INTRODUCTION

This past year of research can be divided into three parts. The first part consisted of devising a corporate feed network using the coplanar line which is amenable to an MMIC active phased array with microstrip antennas. The second part examined experimentally the feasibility of such a feed with an active device as well as some general guidelines for the array design. The third part consisted of analytically characterizing the transmission line, i.e., coplanar line, needed to realize the feed.

Chapter 2 considers the possibility of using a coplanar line rather than the conventional microstrip line in the design of MMIC phased array networks. It is pointed out that proximity feeds, as opposed to feeds that are physically connected to the antenna elements, will be desirable for MMIC active array applications. Though these networks can be realized using either the coplanar or microstrip lines, the former offers advantages over the latter such as the ease of grounding active devices, heat dissipation and less dispersion. To illustrate the potential application of a coplanar line in active antenna design, results from a single element (receiver only) microstrip antenna integrated with a coplanar amplifier are presented. The prototype demonstrated an approximate 13 dB gain in the radiation pattern over the passive antenna and a return loss of 7 dB.

Chapter 3 presents radiation pattern measurements of a four-element microstrip antenna array suitable for MMIC phased array design. The array is fed by a coplanar/slot line proximity feed network. It is shown that the most significant problem with the array is the level of radiation from the back of the array (approximately 16 dB below main beam maximum). Additional measurements of the array with coplanar/slot line feeds of various lengths show that the level of back radiation of both principal planes cannot be reduced below 18 dB even though it is possible to reduce the back radiation in one plane below 22 dB. Hence, it is suggested that possible methods to reduce the back radiation of the array might be to decrease the slot widths used in the feed or by placing a ground plane behind the antenna. Some preliminary measurements also show that it may be possible to adjust the input impedance of the array by changing the feed geometry without significantly changing the radiation pattern of the antenna from its optimum pattern.

Chapter 4 quantitatively discusses the dispersion characteristics of the coplanar line which is needed in the design of the proximity feed networks discussed in Chapters 2 and 3. A brief description of the moment method used is presented as well as a comparison with previous analytical and experimental work. It is found that the results of the full wave analysis of this work show significantly better agreement with experiment and quasi-static analysis than those reported previously in the literature. In addition, a comparison of the dispersion and dielectric loss characteristics of coplanar line with microstrip line on 100 micron gallium arsenide (GaAs, resistivity = 10^7 ohm-cm) substrates for a frequency range from 10 to 100 GHz is also presented. It is found that though the dispersion of coplanar line is less than that of the microstrip line, the effective dielectric constant of microstrip line is greater than that of coplanar line. In addition, though the coplanar line is slightly less lossy than that of microstrip line, the dielectric loss for both transmission lines is insignificant in comparison with conductor losses. Preliminary curves are also shown which indicate that it is possible to adjust the thickness of the coplanar line substrate so that the dispersion of high speed digital pulses propagating in the line is reduced.

Chapter 5 discusses possible areas for future research. This includes the experimental and analytical determination of design guidelines for the coplanar/slot line proximity feed presented in Chapter 3. In particular, a full wave analysis in conjunction with experiment is needed in order to examine the relation between the coplanar/slot line dimensions and the input impedance of the antenna array. In addition, work needs to be done on characterizing multi-layered microstrip antenna arrays, in order to more accurately evaluate the actual MMIC environment likely to be used in the future active arrays. Experimental and theoretical studies need to be conducted in order to find ways to reduce the back radiation of the array.

CHAPTER 2

MONOLITHIC INTEGRATION OF THE MICROSTRIP ANTENNAS WITH ACTIVE DEVICES USING THE COPLANAR LINE

2.1 Introduction

One of the most important issues in the MMIC active phased array concept is the question of the types of antennas suitable for monolithic integration. Clearly, in order to facilitate integration with solid state devices, the antenna must be amenable to fabrication using standard etching techniques. In addition, the antenna should be planar and light weight so that it is compatible with fragile gallium arsenide substrates. These requirements have led people to consider the printed dipole and the microstrip patch antenna. Both antennas are conformal in nature, light weight, and inexpensive to fabricate using standard etching. Though the printed dipole will undoubtedly play an important role in the development of MMIC phased arrays, this work will concentrate mainly on the role of the microstrip patch antenna in MMIC phased arrays.

Recently, it has been pointed out [1] that in order to monolithically integrate large numbers of solid state devices with a microstrip array, one must use a multilayered approach. In Sec. 2.2, the implications of using a multilayered structure in a microstrip antenna feed are discussed. In particular, it is pointed out that the array must be proximity fed rather than fed from a physical connection. Because this proximity feed can be realized using either the microstrip or coplanar line, the relative merits of using microstrip and coplanar transmission lines in proximity feed and microwave circuit designs are examined.

In Sec. 2.3, an experimental application of the coplanar line in active antenna array design is presented. In particular, experimental results of a narrow-band, electromagnetically coupled, microstrip patch/amplifier receiving element at 4.0 GHz is presented. The prototype was designed using standard amplifier design techniques in conjunction with computer-aided design (CAD). The preliminary results show that a gain of 13 dB (over that of the antenna without the amplifier) and a return loss of -7 dB can be achieved.

2.2 Comparison of Microstrip and Coplanar Lines for Use in MMIC Phased Array Feed Networks

Recently [1], it has been pointed out that the monolithic integration of the solid state devices and array elements must be done using a multilayered approach. Specifically, the antenna array should be fabricated separately on one substrate while the solid state circuitry, consisting of bias networks, phase shifters and amplifiers, should be fabricated on one or more different substrates (Fig. 2.1) [1]. There are two reasons for adopting such an approach.

One reason is the limited substrate surface area. By integrating phase shifters, amplifiers and their associated bias circuitry, one automatically puts a premium on the space available on a single substrate. By imposing the spacing requirements of the antenna elements, the amount of available surface area becomes even more critical. A simple solution to this problem is to fabricate the circuits on several layers so that one can overlap the circuitry as shown in Fig. 2.1.

Another reason for adopting the multilayered approach has to do with the conflicting requirements of the printed circuit antenna and the solid state devices. In particular, to radiate efficiently, these antennas must be fabricated on a low dielectric substrate, such as duroid (ε_r=2.2). The solid state devices, on the other hand, must be fabricated on high permittivity semiconductors, such as GaAs (ε_r=12.91). Hence, in order to satisfy their conflicting needs, at least two different substrates should be used.

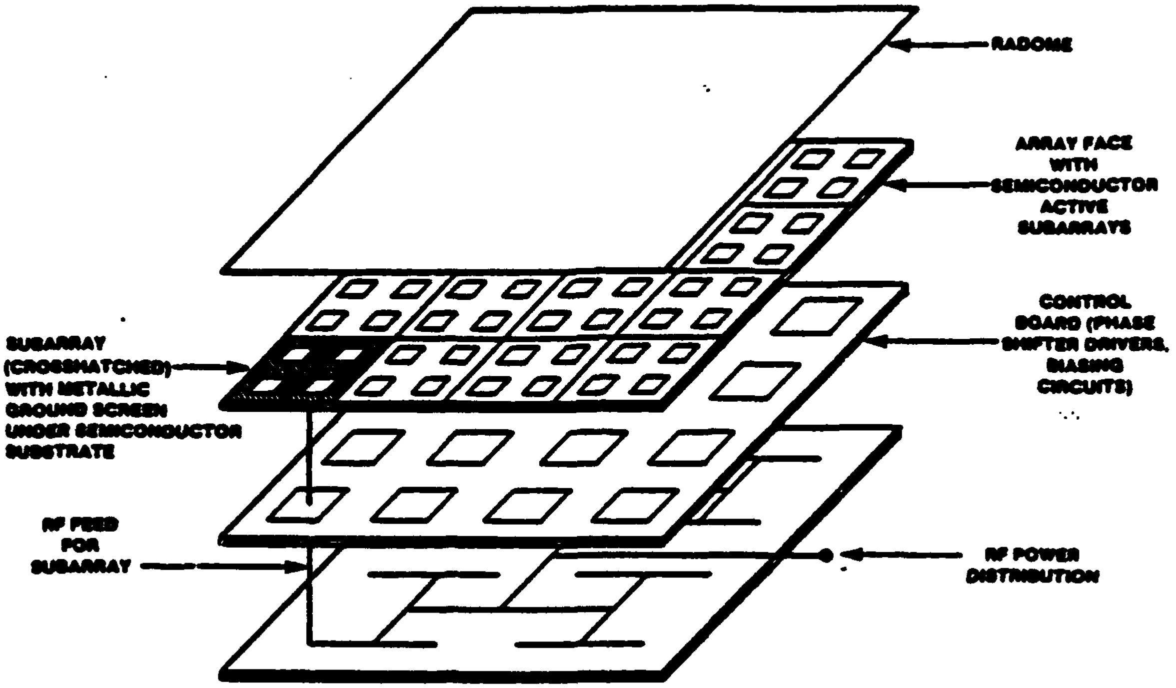

Fig. 2.1 A possible MMIC active phased array using multilayered substrates.

The multilayered configuration, however, itself imposes a restriction on the design of the active phased array. Due to the fabrication difficulties associated with making physical connections that are not planar, i.e., normal to the substrate plane, one must consider alternate methods of interfacing the antenna array with the active circuitry. A convenient way of interfacing the two is to use proximity feeds, which electromagnetically couple energy into the antenna from the circuits via planar transmission lines. There are essentially two transmission lines with which one can realize proximity feeds suitable for MMIC active phased arrays. They are the microstrip transmission line and the coplanar waveguide. Each can be used as an open-end feed (Figs. 2.2-2.3) or in combination with slots which couple into the patch (Figs. 2.4-2.5). In the past, there has been a great deal of work done on proximity feeds but, they have dealt mostly with the use of the microstrip line rather than the coplanar line. In order to fully compare the relative advantages and disadvantages of both transmission-line types in proximity feeds, it would be desirable to carry out a quantitative investigation of the impedance characteristics and coupling efficiency of the antennas in Figs. 2.2-2.5. Such a task, however, would require a long range study and is left for future research. There are, however, some important qualitative observations one can easily make about the strengths and weaknesses of the coplanar and microstrip-line proximity feeds. For instance, one weakness of the coplanar line for use in proximity feeds is the possible propagation of nonattenuating higher-order modes. Specifically, an asymmetry in the configuration of the coplanar line, i.e., one slot is not identical to the other, will cause an asymmetry in the field distribution which can result in even mode propagation. This will tend to occur whenever bends in the coplanar line are

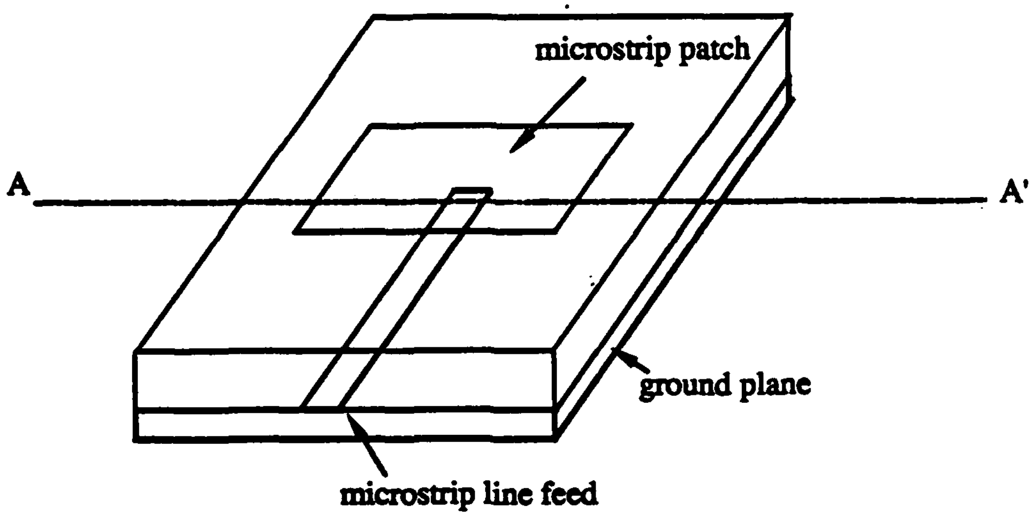

a) perspective

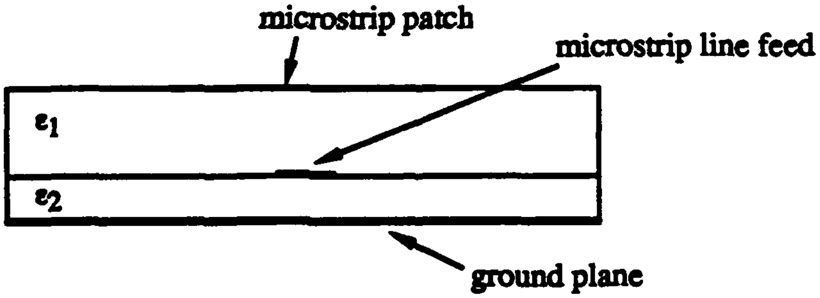

b) cross section of AA'

Fig. 2.2 Microstrip antenna fed with an open-ended microstrip line.

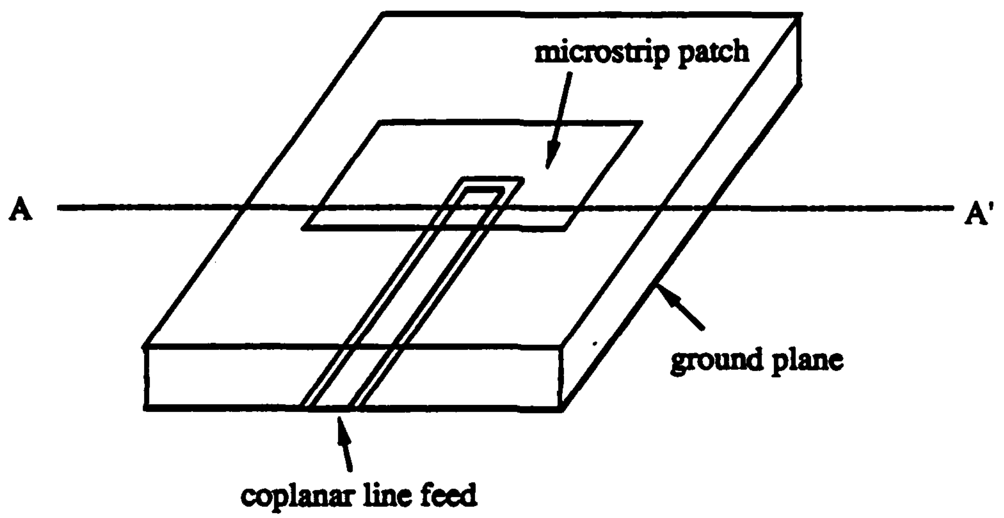

a) perspective

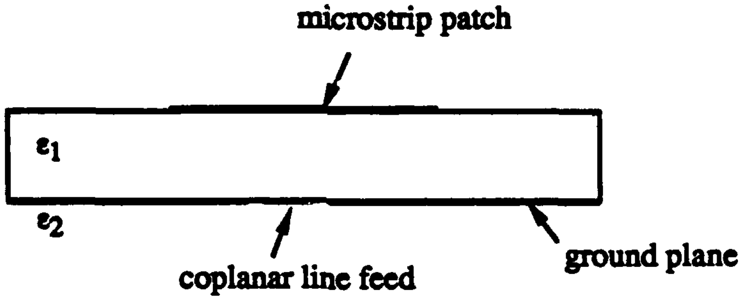

b) cross section of AA'

Fig. 2.3 Microstrip antenna fed with an open-ended coplanar line.

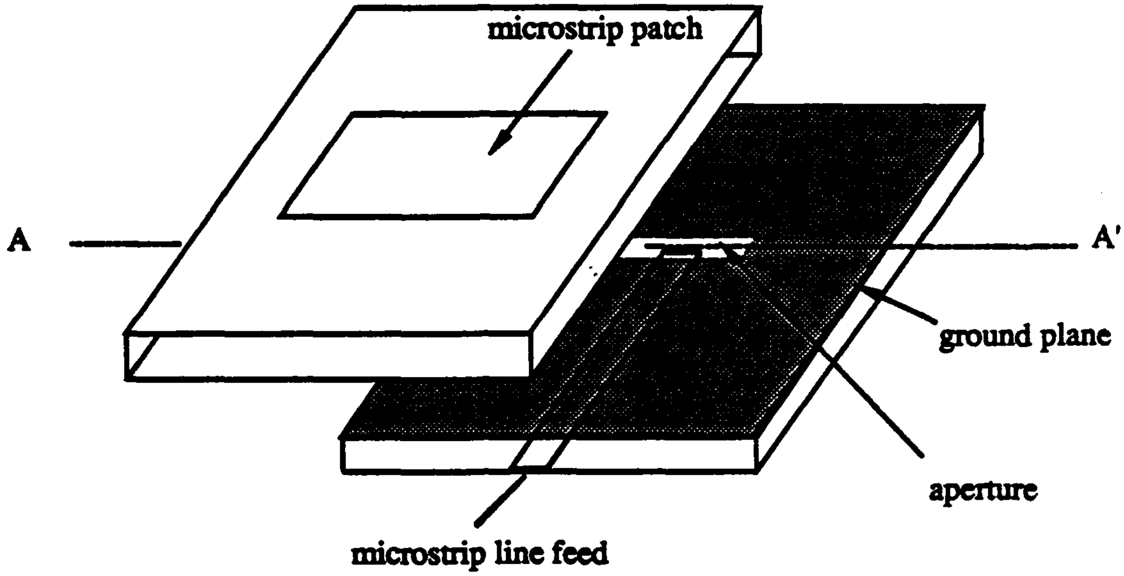

a) perspective
(disassembled)

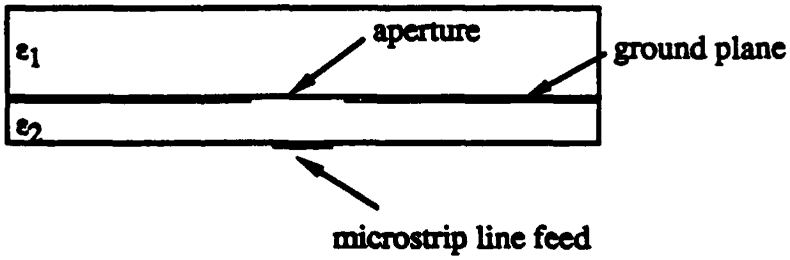

b) cross section of AA'

Fig. 2.4 Microstrip antenna fed with an aperture coupled microstrip line.

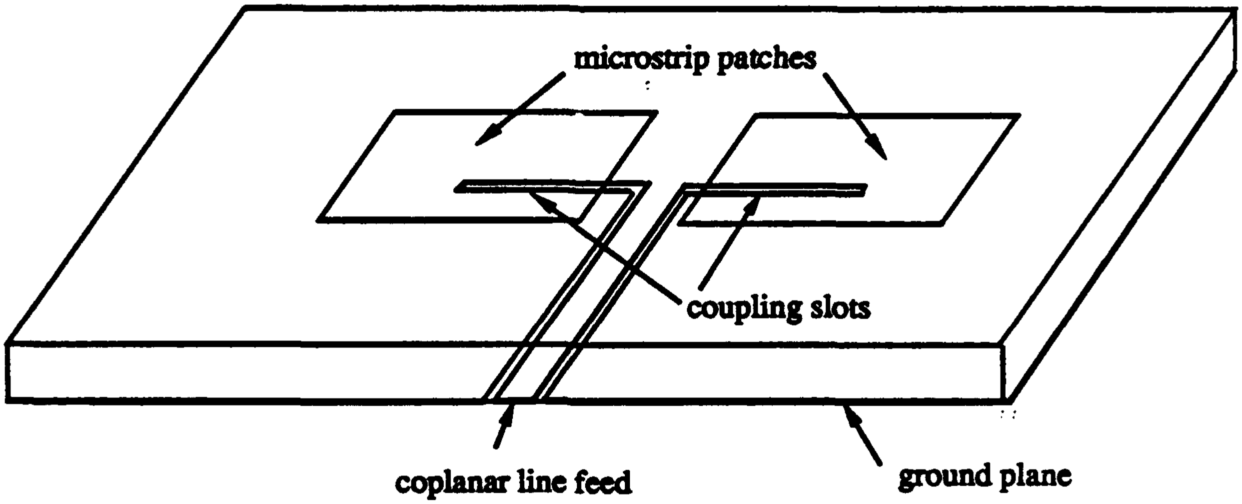

Fig. 2.5 Microstrip antenna fed with a combination of coplanar line and slot line.

required. These modes can have deleterious effects on the amplifier and phase shifters since both are designed for TEM waves. One way to suppress these modes is to place air bridges periodically along the line. The addition of these air bridges, however, adds to the complexity and cost of the feed. The microstrip line, on the other hand, can be bent in many different directions without similar complications.

Perhaps the biggest disadvantage in using the coplanar guide, not only for MMIC phased array design but in microwave circuit design in general, is the lack of theoretical and experimental data with which to characterize coplanar discontinuities. Though there has been experimental work reported in the past, i.e., [2], [3], [4], they are of limited use to the microwave engineer because there were no useful design formulas or curves. To aggravate matters further, computer-aided design tools are currently unavailable for optimizing coplanar circuit design. The microstrip line, on the other hand, has been used extensively in industry and its characteristics are well understood. Though the two most popular computer-aided design programs, SUPERCOMPACT and Touchstone, may not be applicable to MMIC design for frequencies >15 GHz (due to the radiation losses and the breakdown of the quasi-TEM approximations), most microwave engineers are likely to have a better "feel" for using the microstrip line at the higher frequencies than the seldom used coplanar line.

Despite shortcomings, the coplanar line has several important advantages over the microstrip line for use in MMIC phased arrays. The first of these advantages is the ease in which solid state devices, such as FETs, can be grounded. Unlike the microstrip line, the ground plane is located on the same plane as the center or "hot" conductor. This means that expensive, low yield via hole etching, which is used to ground devices on the microstrip, can be avoided, hence, simplifiying the fabrication process and lowering the cost. The coplanar line offers more design flexibility in realizing the characteristic impedance.

Specifically, for a fixed substrate thickness, the characteristic impedance of a coplanar line can be obtained using different "hot" conductor widths whereas the microstrip cannot. This is because the coplanar line impedance is dependent on the "hot" conductor width-to-slot-width ratio. This is in contrast with the microstrip line which is dependent solely on the "hot" conductor width-to-substrate-thickness ratio. Hence, for a given substrate thickness, there is an additional freedom for the engineer using the coplanar line in being able to change the "hot" conductor width without changing the impedance. This freedom, for example, may allow a circuit designer to use a variety of GaAs substrate thicknesses to fabricate the solid state devices and without having to worry about 50-ohm transmission line interconnects that may have unusually large or small microstrip line widths.

2.3 Integration of a Proximity-fed Microstrip Antenna with a *Distributed Amplifier* Using the Coplanar Line

To illustrate the possible use of the coplanar line in MMIC active phased arrays, a 4.0 GHz, single element, microstrip patch antenna fed with an open-end, coplanar proximity feed was integrated with an amplifier. For simplicity, the prototype was designed as a receiving element. The design procedure can be divided into two parts: 1) the antenna design and 2) the amplifier design.

2.3.1 Microstrip patch antenna design

The microstrip antenna was designed using standard design rules[1]. Briefly, the patch was designed to operate in the TM (0,1) mode. This was accomplished by designing side b (Fig. 2.6) to be approximately equal to 0.5 λ_g, where λ_g is the wavelength of the

---

[1] The design details of the rectangular microstrip patch antenna are discussed in the next chapter.

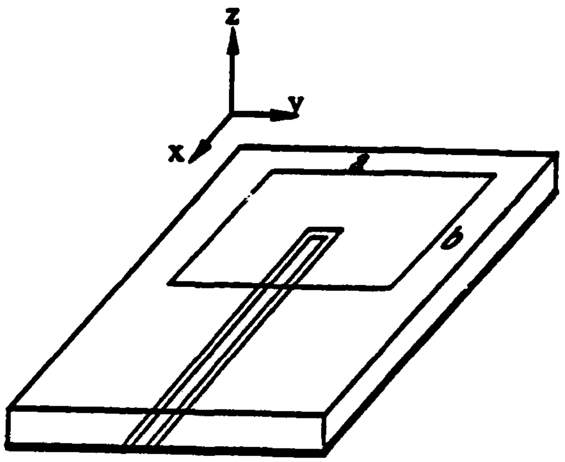

a = 3.4 cm

b = 2.3 cm (approx. 0.5 λ_g)

Fig. 2.6 Configuration of the microstrip antenna used in the integration with the amplifier.

operating frequency inside the substrate. To simplifiy the design of the amplifier and to illustrate the good impedance characteristics of the coplanar proximity feed, the open end of the coplanar line was positioned so that a 50-ohm input impedance was achieved. However, because there were no design rules or theoretical analysis for this type of antenna structure, this input impedance was achieved through experimental trial and error. After several iterations, a satisfactory 50-ohm impedance at antenna resonance was achieved at approximately 3.78 GHz. The return loss was found to be 16.0 dB.

2.3.2 Amplifier design using coplanar line

The amplifier was designed using the coplanar line rather than the commonly used microstrip line. This was necessary for the integration of the amplifier with the proximity feed. The design can be summarized in essentially three steps. The first step was to obtain accurate S-parameters of the FET (packaged NEC 700) to be used in the amplifier. The second step was to design a lumped element matching network which would result in a conjugate match between the antenna and FET. The third and final step was to replace the lumped prototype with various coplanar discontinuities to approximate the lumped elements.

Steps one and two are fairly routine and straightforward in nature [5]. Hence, only the results are shown in Figs. 2.7 and 2.8. To simplify the amplifier design, as well as help circumvent the lack of coplanar discontinuity design equations, the lumped matching networks were designed for maximum available gain operation rather than for a wide bandwidth which is mainly limited by the antenna itself. Although there were many amplifier designs that could have achieved maximum available gain, the lumped element design shown in Fig. 2.8 was chosen due to its simplicity. The lumped elements were then approximated by using various lengths of high and low impedance coplanar transmission

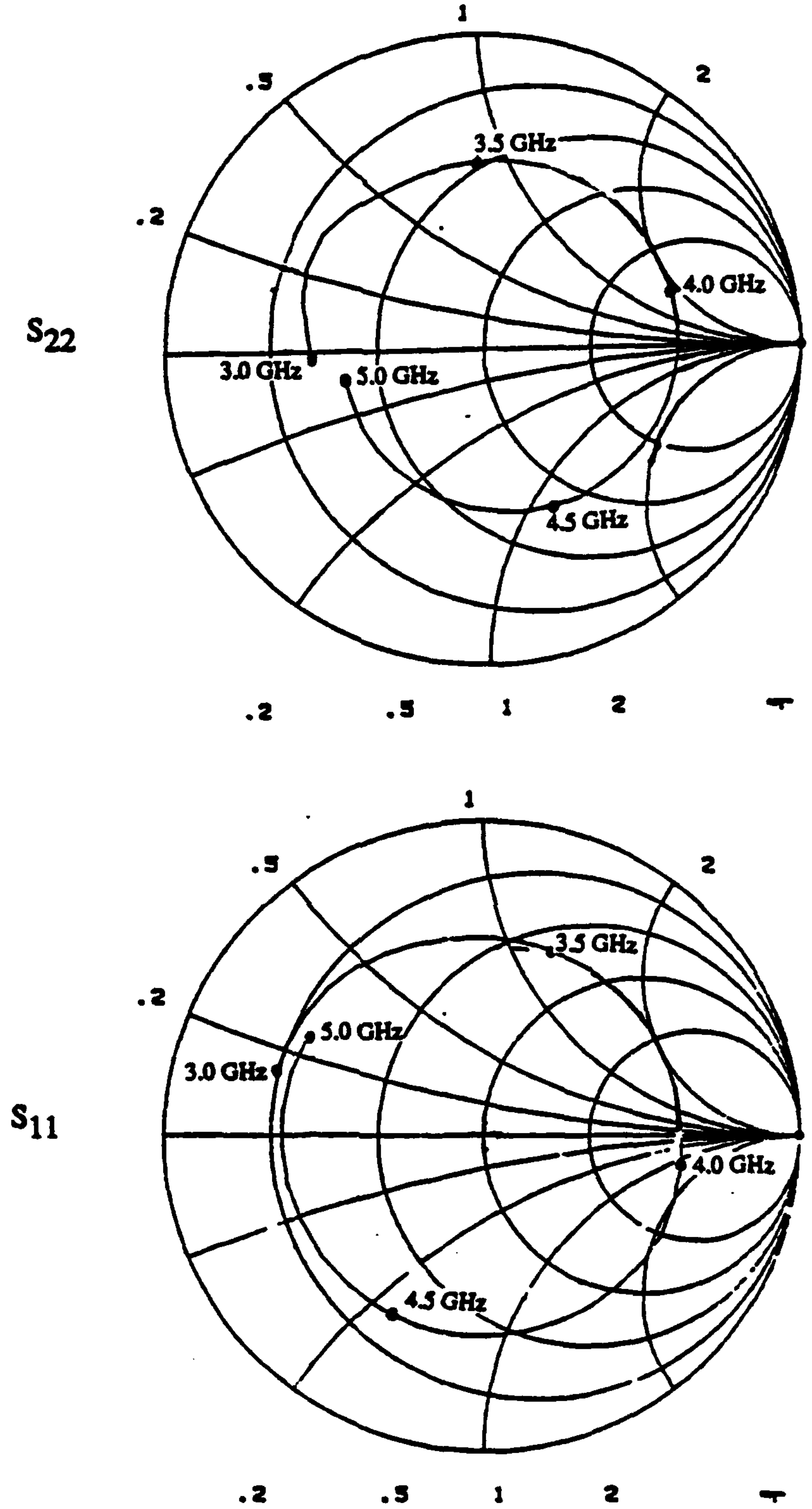

Fig. 2.7 Experimentally de-embedded S_{11} and S_{22} parameters of the NE 70083 GaAs MESFET used in the amplifier design.
Q point: drain voltage, $V_{ds} = 3$ V
drain current, $I_{ds} = 30$ mA

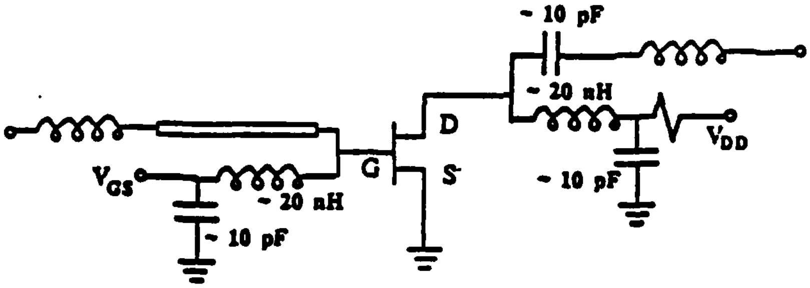

Fig. 2.8 Lumped element model of the amplifier used in the integration with the antenna.

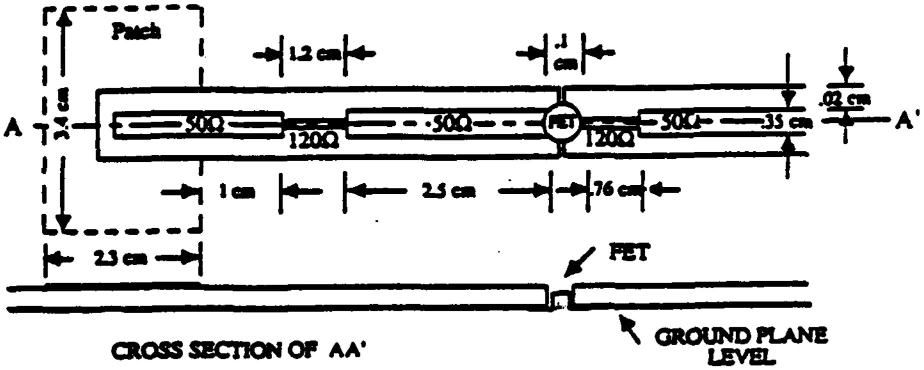

Fig. 2.9 Dimension of the integrated antenna /amplifier realized using coplanar line.

lines connected in series. By using these transmission-line approximations[2], it was possible to avoid the use of coplanar discontinuities and coplanar tuning stubs (both of which have yet to be studied either analytically or experimentally) in the distributed circuit. In addition, these approximations were also amenable to a certain degree of modeling on SUPERCOMPACT.

2.3.3 Results of the antenna/amplifier integration

The final optimized coplanar transmission line amplifier, which was fabricated on 62.5 mil rexolite, is shown in Fig. 2.9. All coplanar transmission-line characteristics such as effective dielectric constant and characteristic impedance were calculated using quasi-static formulas. Figures 2.10 and 2.11 show the E- and H- plane radiation patterns of the integrated antenna/amplifier. They are superimposed on the radiation pattern of a "passive" element with the same feed structure but without the amplifier. The difference in the relative power levels indicates that the amplifier adds approximately 13 dB of gain to the antenna element. This is approximately 3 dB less than that predicted by SUPERCOMPACT. This discrepancy is attributed to the presence of the biasing network, i.e., the dc blocking capacitor, which was assumed to have negligible effect, and the step discontinuities in the coplanar line which were ignored in the design. The ripple in the radiation pattern is caused by the diffraction from the ground plate edges. The slight asymmetry in the E-plane is most likely due to the presence of the coplanar feed and amplifier circuitry.

---

[2] It should be noted that, in general, this approximation cannot be used due to its narrow-band nature as well as its excessive physical length requirements. In the future, coplanar discontinuities with broader bandwidths will be needed for practical MMIC design. Because the microstrip patch is inherently narrow band and the length of the distributed amplifier is not of major concern for this study, this approximation has been implemented.

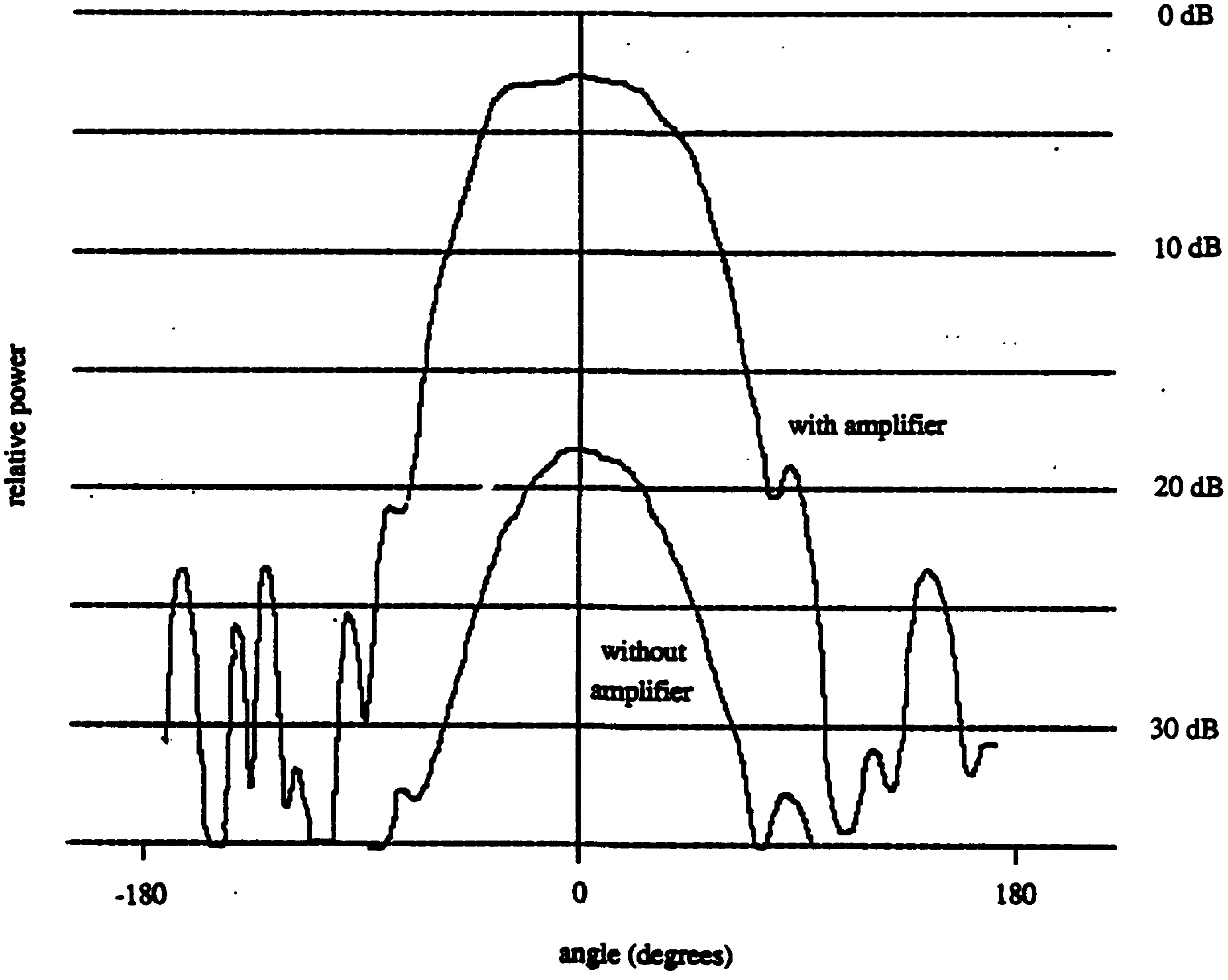

Fig. 2.10 Experimental H-plane radiation patterns of the microstrip antenna with and without amplifier.

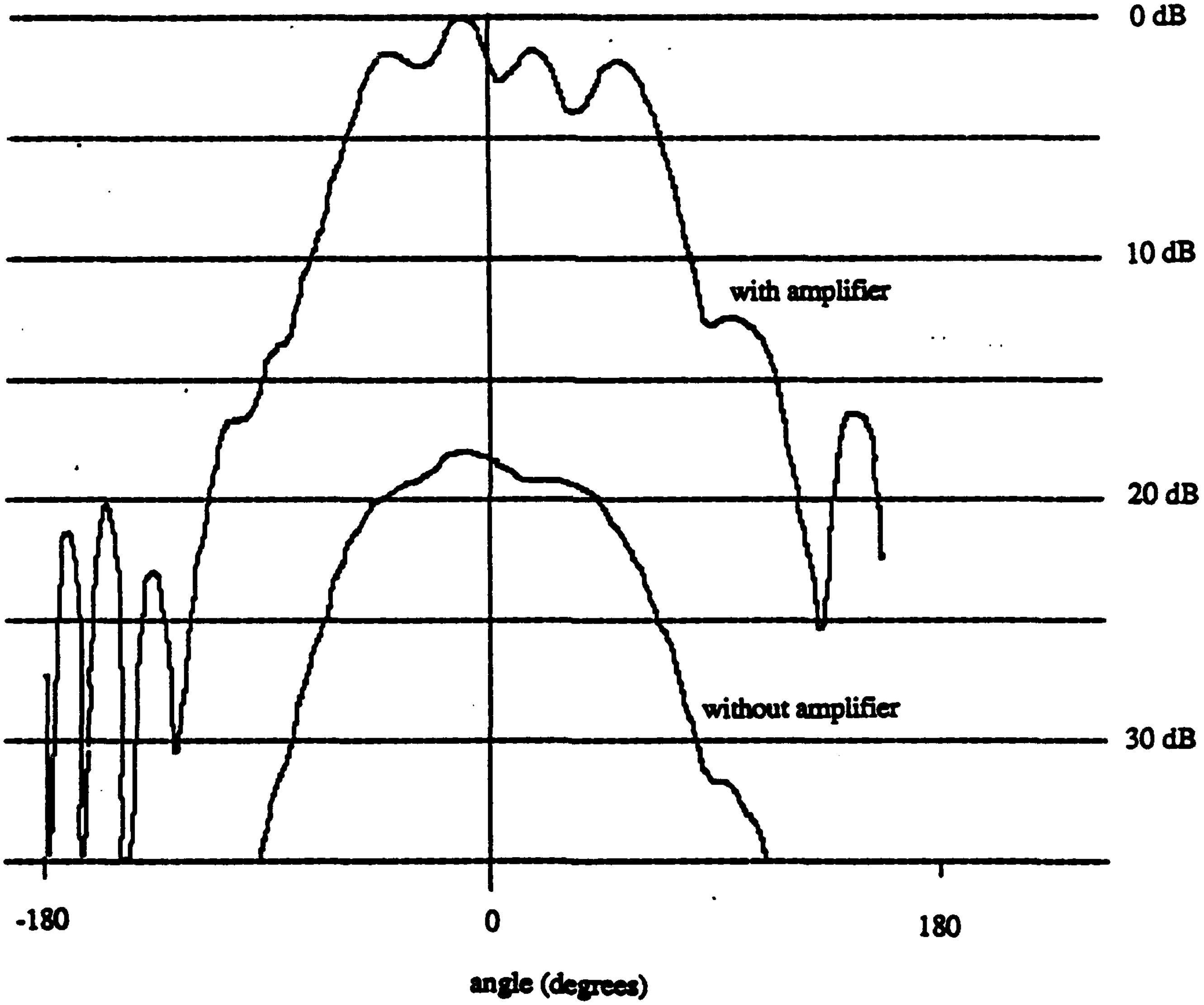

Fig. 2.11 Experimental E-plane radiation patterns of the microstrip antenna with and without amplifier.

2.4 Summary

A qualitative discussion on the need to use a multilayered approach in MMIC phased array design, in particular for the microstrip patch antenna, was presented. Some of the motivations for adopting such an approach were the conflicting substrate requirements of the active devices and microstrip antennas and space requirements. The need for proximity feeds that electromagnetically couple energy into the microstrip antennas was also discussed. Various proximity feed configurations made up of coplanar and microstrip transmission lines were also presented as well as a discussion of their relative merits for use in MMIC circuit design. It was found that the coplanar line has certain advantages over the microstrip line such as ease of grounding solid state devices and the capability of achieving a given characteristic impedance with many different center or "hot" conductor widths on a fixed substrate. The major disadvantages of using a coplanar line rather than a microstrip line were due to the possibility of even mode (non-TEM) propagation in complicated proximity feed networks as well as the lack of design equations and computer-aided design packages.

To illustrate the feasibility of this new integrated feeding technique, a proximity fed microstrip patch antenna with amplifier realized entirely on a coplanar line was studied. In particular, the E- and H- plane radiation patterns of the antenna with and without the amplifier were compared. The antenna with the amplifier was found to have approximately 13 dB more gain than the antenna without the amplifier.

CHAPTER 3

EXPERIMENTAL CHARACTERIZATION OF A MICROSTRIP ARRAY FED WITH A COPLANAR/SLOT PROXIMITY FEED

3.1 Introduction

In Chapter 2, the experimental results of a single-element proximity-fed microstrip antenna/amplifier were presented. Though the results were good, the open-end, coplanar proximity feed used in the design may not necessarily be the scheme best suited for feeding an array of microstrip antennas. Recently, it was suggested [6] that the coplanar line in combination with the slot line can also be used as a means of realizing proximity feeds for microstrip antennas (Fig. 3.1). By using the coplanar line in conjunction with the slot line, a considerable reduction in the amount of transmission line needed to connect the array elements can be achieved. This savings can reduce transmission line losses as well as simplify the feed network. In addition, the coplanar/slot configuration can also reduce the number of air bridges needed to suppress even-mode propagation.

In Section 3.2, a qualitative description of the coupling mechanism between the coplanar/slot proximity feed and the microstrip patch antenna is presented. For simplicity, the description is given in the context of the microstrip antenna cavity model [7].

In Section 3.3, the design and experimental results of a four-element coplanar/slot proximity fed microstrip antenna [8] suitable for array applications are presented. Preliminary results show that the antenna has good broadside E- and H- plane radiation characteristics, but that the radiation from the back of the antenna is somewhat high (approximately 15 dB down from the main lobe). It is believed that this back radiation can be reduced by changing the slot width or by using a ground plane. Additional experimental results are shown which imply that the radiation patterns of the array are essentially unaffected by different coplanar/slot feed configurations. This, in turn, implies that the input impedance of the array may be adjusted simply by changing the feed geometry without degrading the radiation characteristics of the antenna.

3.2 Coupling Between the Proximity Feed and the Microstrip Antenna

The physics behind the coupling mechanism between the microstrip antenna and the coplanar/slot line proximity feed is most easily discussed in terms of the microstrip antenna cavity model. In this model, the microstrip patch antenna on thin substrates can be viewed as a resonant cavity with perfect magnetically conducting walls (Fig. 3.2). Hence, the field distributions inside the patch may be viewed as modes which satisfy the boundary condition of the patch. Clearly, these boundary conditions imply that for the dominant (0,1) mode only the electric field in the z-direction and the magnetic field in the x-direction are nonzero. The thin substrate criterion implies that these fields have no z-variation. Hence, the fields inside the cavity may be described in terms of transverse (to the z-direction) magnetic cavity modes without z-dependence.

In previous works, it has been shown that the TM (0,1) mode of the microstrip patch corresponds to the highest efficiency of the antenna. This will result in radiation from the b side or long side of the patch. As with rectangular cavities with perfect electrically conducting walls, a particular mode in the microstrip antenna may be excited by orienting an electric or magnetic current source inside the patch such that

$$\mathbf{E}\cdot\mathbf{J} \neq 0 \text{ or } \mathbf{H}\cdot\mathbf{M} \neq 0$$

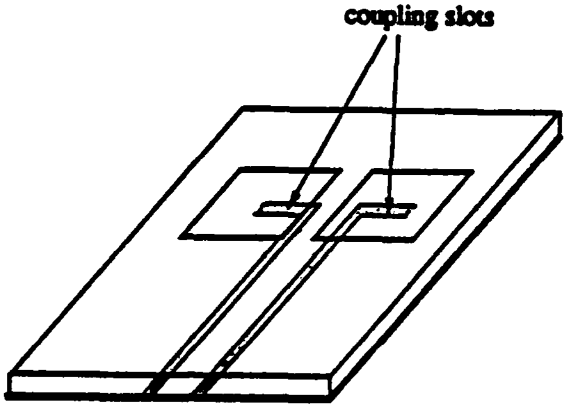

Fig. 3.1 An example of a coplanar/slot line proximity feed for a two-element microstrip array.

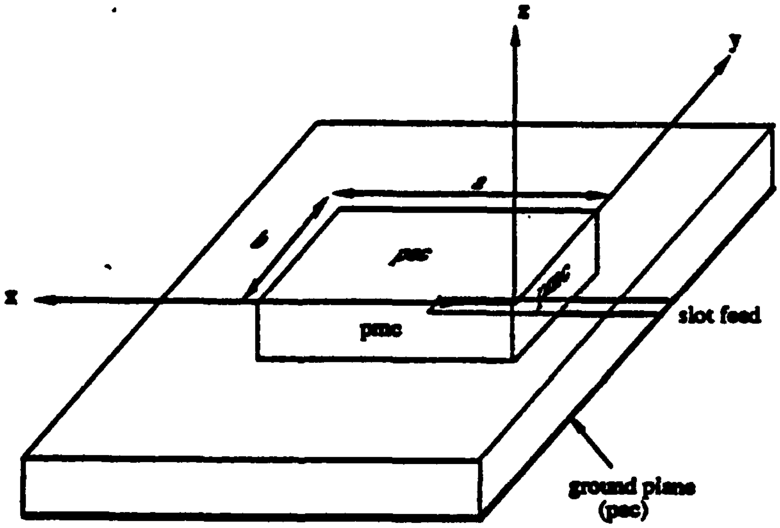

Fig. 3.2 Cavity model of a microstrip patch antenna proximity fed from a slot.

where **E, H** = the electric and magnetic fields of the cavity mode, respectively,

J = electric current source

M = the magnetic current source.

Hence, it is possible to excite primarily the TM (0,1) mode inside the patch by either placing an electric current source in the z-direction or by placing a magnetic current source in the x-direction, preferably at a location where **E** or **H** is a maximum.

This ability to excite the proper cavity mode with a magnetic current source is the crux of the operation of the coplanar/slot proximity-fed microstrip antenna. The slot has a field distribution (dictated by the even- or odd-mode propagation of the coplanar line) which, from the equivalence principle, can be expressed in terms of equivalent magnetic and electric current sources. In particular,

$$\mathbf{M}_{equiv} = -\,\mathbf{n}\mathrm{x}\mathbf{E}_{slot}$$

$$\mathbf{J}_{equiv} = \mathbf{n}\mathrm{x}\mathbf{H}_{slot}$$

where $\mathbf{M}_{equiv}$, $\mathbf{J}_{equiv}$ = equivalent magnetic and electric current sources, respectively,

n = unit normal to the plane of the slot.

By assuming that the electric field inside the narrow slots is polarized solely in the y-direction, the equivalence principle implies that the length of the slot line (which will herein be referenced as the "primary slot feed") acts like a magnetic current source in the x-direction. This source can, in turn, excite the TM (0,1) mode of the antenna. In the case of the four-element array (see Fig. 3.3) to be discussed in the next section, it can be deduced that in order to excite the antenna elements in phase the odd mode of the coplanar line must propagate.

3.3 Design and Measurement of a Four-Element, Coplanar/Slot Fed Microstrip Array

A diagram of the four-element coplanar/slot fed array is shown in Fig. 3.3. Though the design of the microstrip patches is well known, there are presently no formulas for the design of a corresponding coplanar/slot-proximity feed. Due to the complicated numerical analysis required for this system, one of the main objectives of this work was to experimentally determine design guidelines. This was accomplished by fabricating and measuring several four-element arrays of identical operating frequency but different coplanar/slot geometries.

3.3.1 Initial design of the array and proximity feed

The approximate dimensions of the four-element prototype that was eventually tested are shown in Fig. 3.4. The microstrip patch antennas used in this study were designed to have an operating frequency around 5.0 GHz. This was accomplished by designing the b side of the patch to be approximately 0.5 λ_g, where λ_g is the wavelength inside the dielectric substrate. Their aspect ratio (a/b) was designed to be 1.5 in order to maximize radiation efficiency and reduce the cross polarization. In order to avoid grating lobes the patches were then positioned in a 2x2 array such that the adjacent patch edges were 1 cm apart from the edges of the neighboring patches.

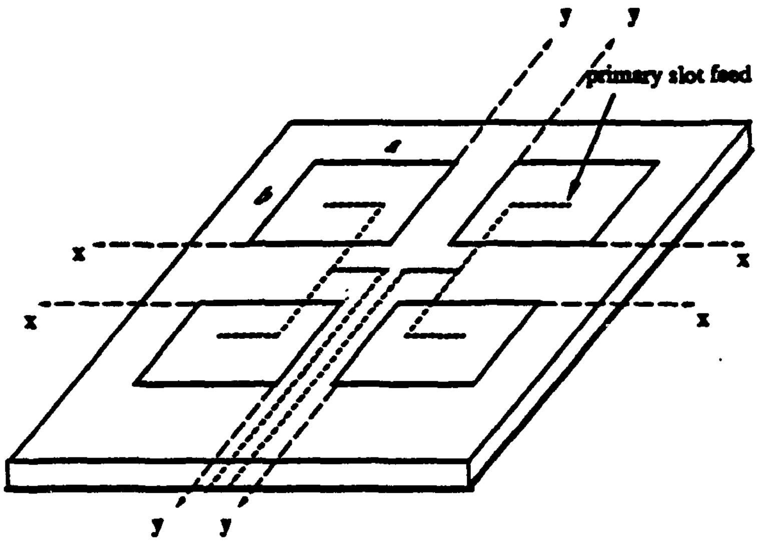

Fig. 3.3 Configuration of the four-element, coplanar/slot fed microstrip patch array.

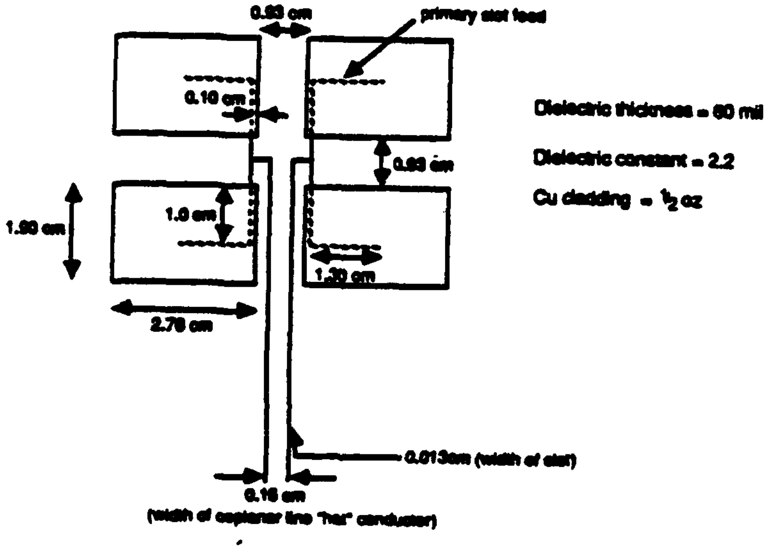

Fig. 3.4 Dimensions of the four-element array used in this study. f_0, the operating frequency, = 4.8 GHz

Though the design of the microstrip antenna has been well studied, the design of the coplanar/slot proximity feed has not. Hence, the design of the proximity feed used in the prototype was somewhat arbitrary, based on a combination of qualitative physical intuition and limitations in fabrication. The coplanar line was designed to have a characteristic impedance of 50-ohms commonly used in microwave circuits for power transfer. The actual physical dimensions of the coplanar line were chosen such that the amount of radiation from the slots would be minimized. This was done by making its slots as narrow as could be fabricated while adjusting the "hot" conductor width to maintain a 50-ohm impedance. For this study, a slot width of approximately 0.1 mm and a center conductor width of 1.5 mm were used. Broadside radiation from the slot line was reduced by placing as much of the slot under the patch as possible. The width of the slot line was arbitrarily chosen to be the same width as that of the coplanar line. The primary slot feed length and its y-axis position under each patch were left variable so that their optimum dimensions (with regard to the antenna radiation) could be determined.

3.3.2 Comments about the fabrication and measurement procedure

Before an actual discussion of the experimental results of the array can be done, two important comments about the experimental procedure used in this study are in order. First, due to the lack of adequate facilities, the antennas were not etched using photolithography but were made by hand cutting. Moreover, the microstrip patches used in this array were fabricated from copper tape which had a tendency to curl up along the edges of the patch due to the adhesive wearing down. Hence, the patch had to be replaced periodically during the measurements. This may have affected the repeatability of the measurements. Second, the repeatability of the measurements may have also been affected by the antiquatedequipment setup used to measure the radiation patterns in which the alignment between the transmit and receive antennas was done by human sight rather than with laser beam sighting.

In spite of these potential causes of experimental error, it is believed that the frequency of operation was low enough so that the measurements of the array were not severely affected.

3.3.3 Experimental results

Figures 3.5 and 3.6 show the measured E- and H- plane radiation patterns for a four-element array fed with the primary slot feed located at the center of each patch (y=b/2) with a length of 7 mm. The antennas are found to have low cross polarization (>20 dB) and low side-lobe levels (>20 dB). In general, the array is found to have very good radiation characteristics except for the somewhat high levels of radiation from the back of the antenna (approximately 15 dB down from the main lobe).

Figures 3.7 - 3.9 show the H-plane radiation patterns of several four-element arrays of identical construction to the one tested earlier, but with different primary slot-feed lengths. These figures indicate that changing these lengths has a dual effect on the level of radiation emitted from the back of the array. In particular, it can be seen that by varying primary slot-feed lengths it is possible to reduce the amount of back radiation in the H-plane to approximately 20 dB down from the main beam. The amount of back radiation in the E-plane radiation pattern (not shown), however, was found to increase whenever this minimum occurs. This effect suggests the levels of back radiation in

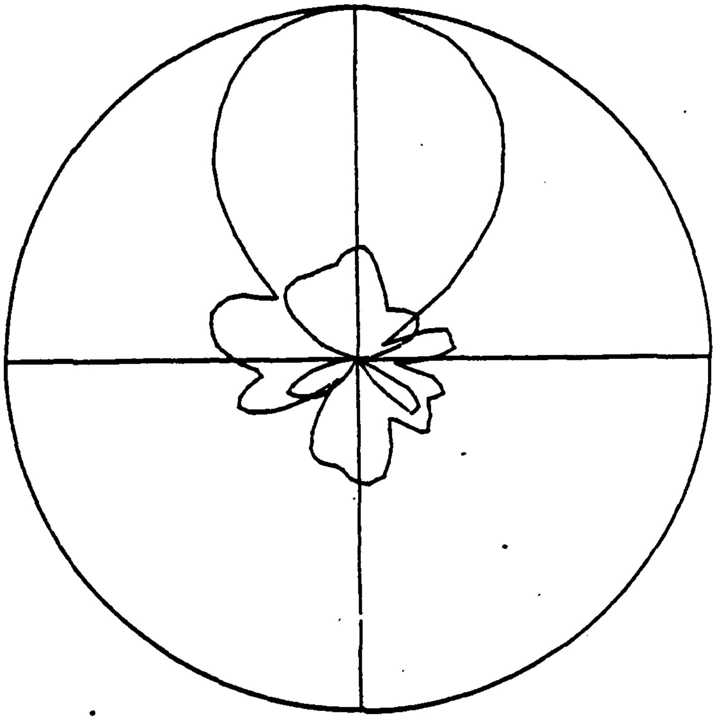

Fig. 3.5 H-plane polar plot of the four-element array with a primary slot feed: x = 7 mm, y = b/2.

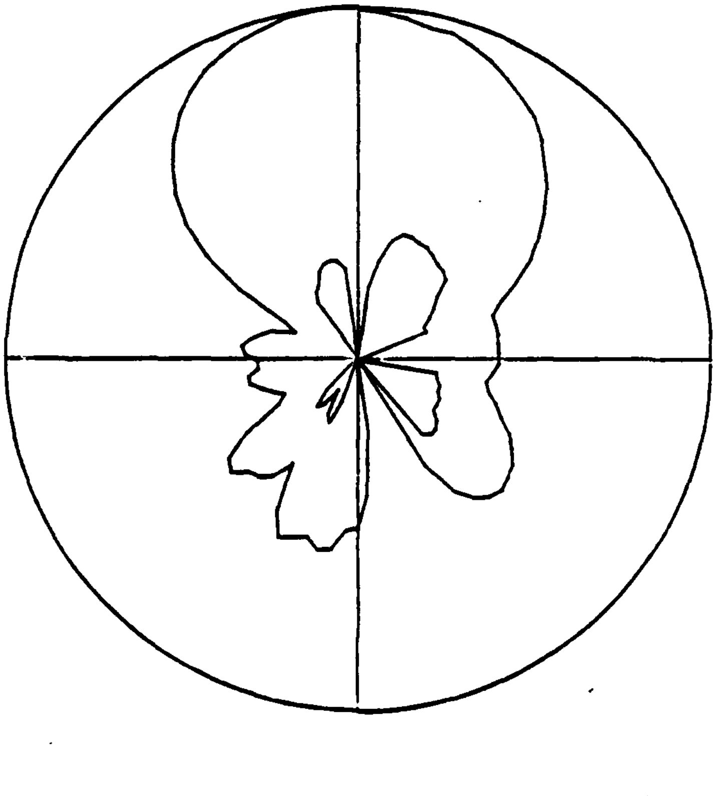

Fig. 3.6 E-plane polar plot of the four-element array with a primary slot feed: x = 7 mm, y = b/2.

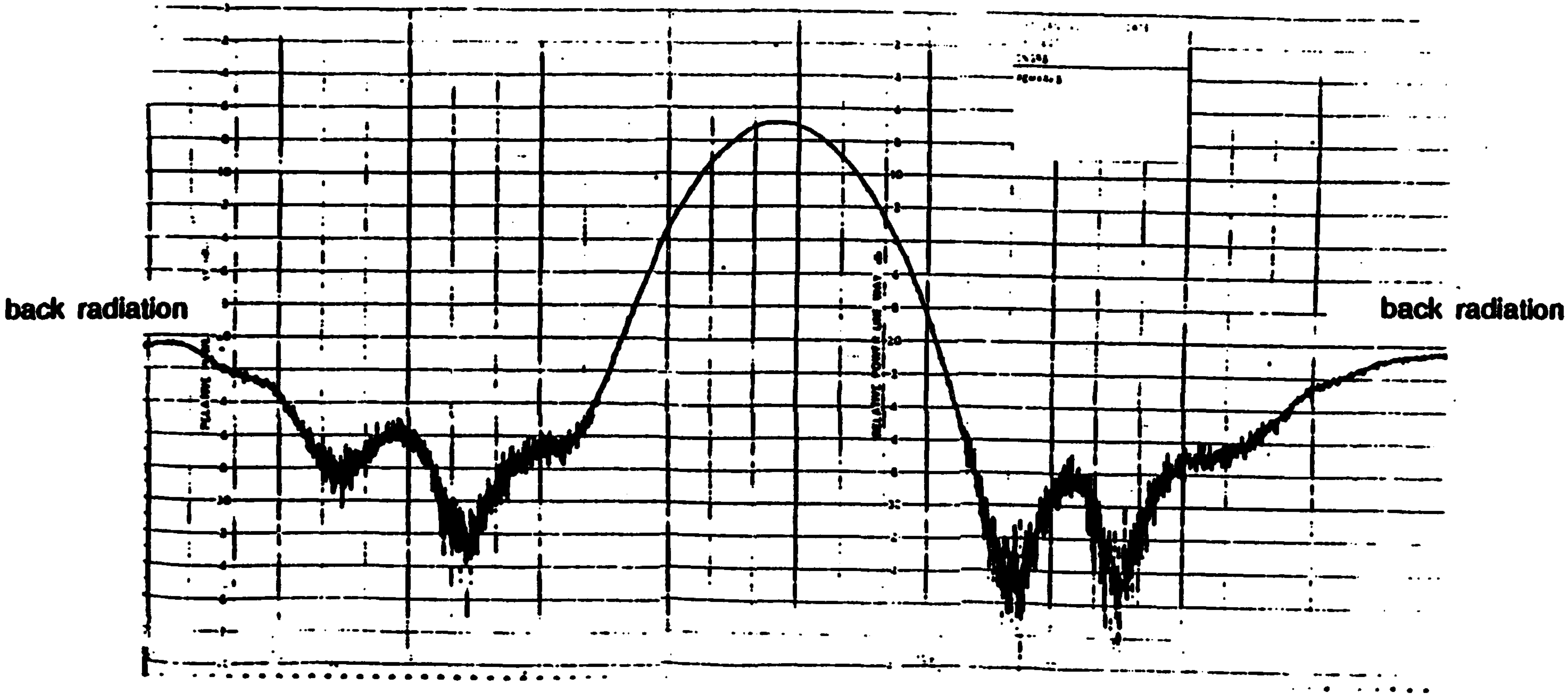

Fig. 3.7 H-plane radiation pattern of the four-element array with primary slot feed: x = 3 mm, y = b/2.

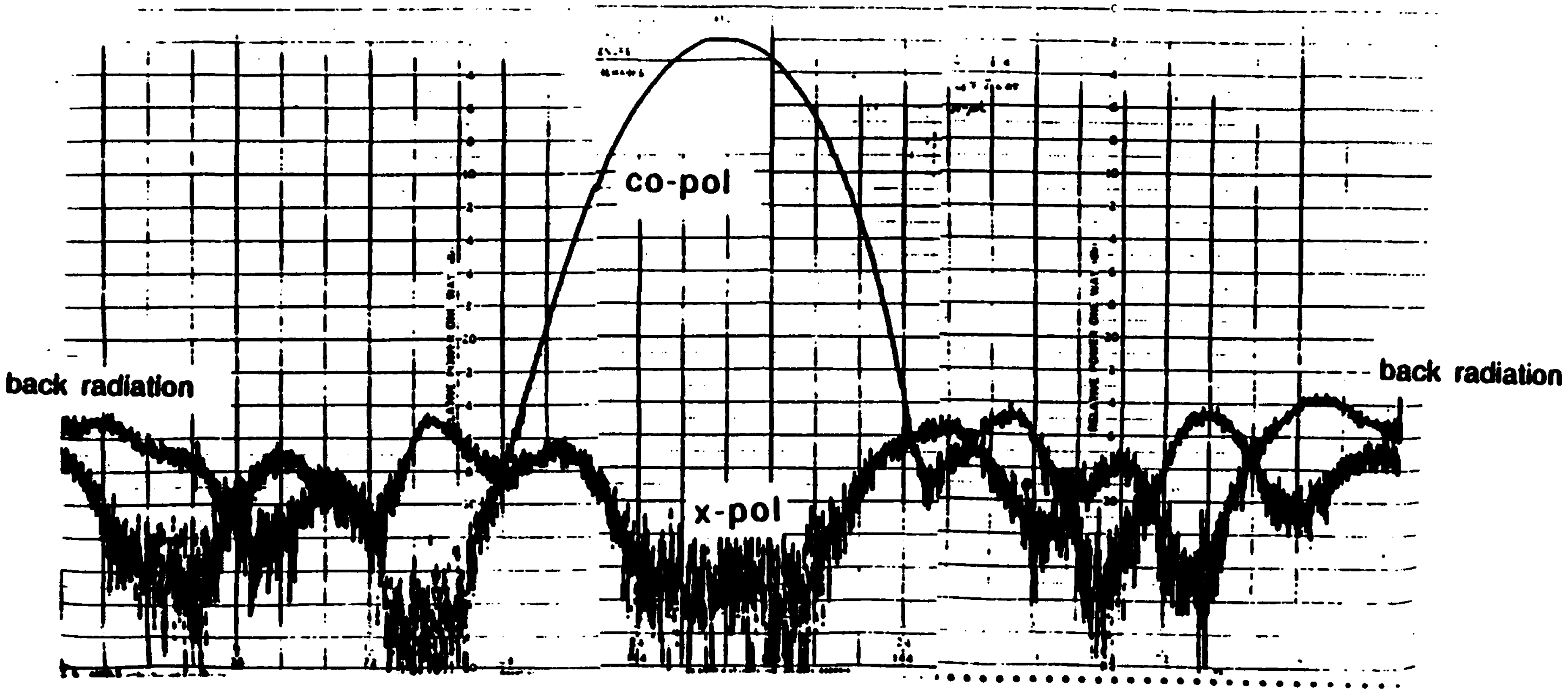

Fig. 3.8 H-plane radiation pattern of the four-element array with primary slot feed length: x = 7.2 mm, y = b/2.

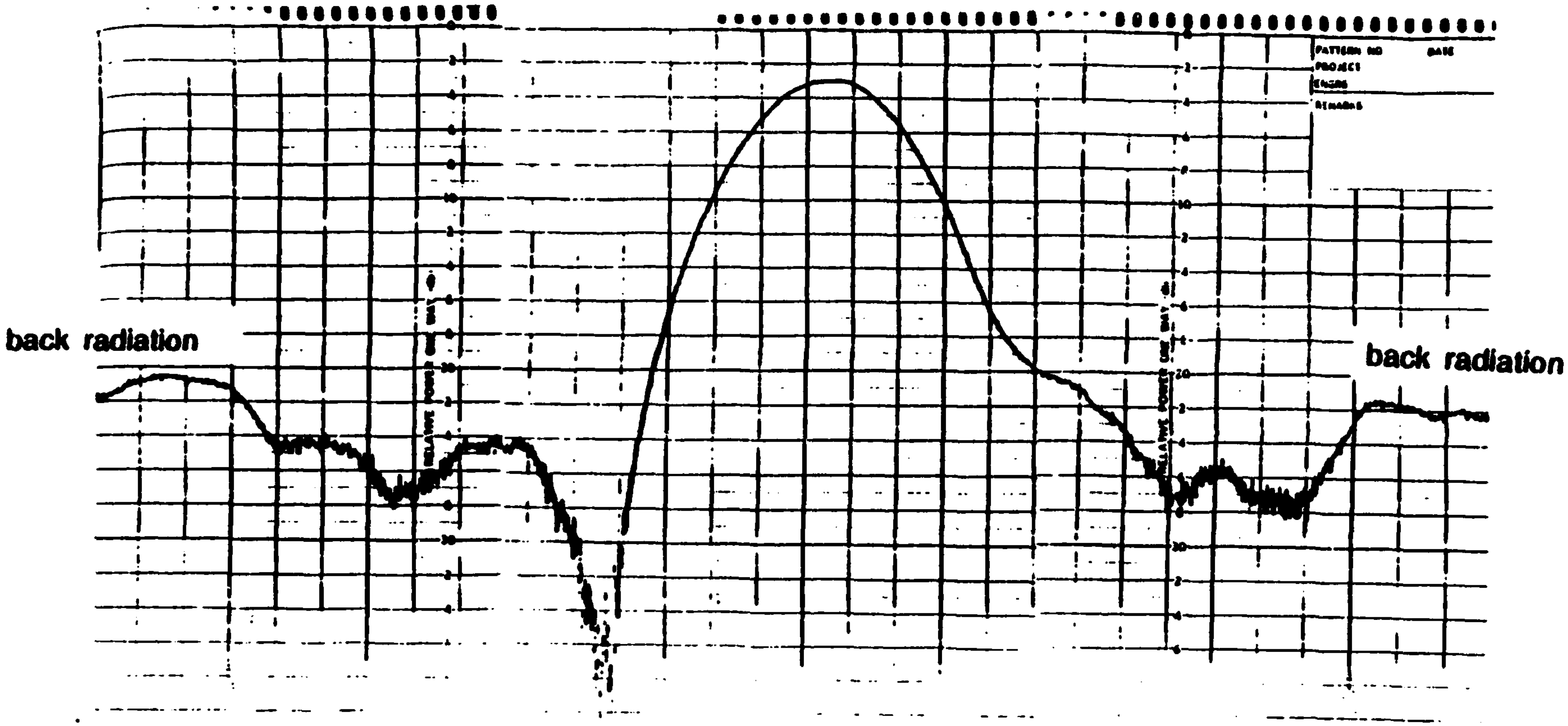

Fig. 3.9 H-plane radiation pattern of the four-element array with primary slot feed length: x = 13 mm, y=b/2.

the E- and H-planes are inversely proportional to one another, i.e., as the back radiation from the E-plane increases the back radiation from the H-plane decreases. Hence, it appears that one cannot reduce the level of back radiation of both the E- and H-planes simply by changing the primary slot length alone. Further experimental work needs to be done to research this relationship.

Figures 3.10-3.13 show the E- and H-plane radiation patterns of the array with the primary slot feed positioned at various locations along the y axis, while keeping the length of the slot fixed at 9 mm. It can be seen that, although the shape of the pattern appears to change slightly, the side-lobe levels and back-radiation level appear to be constant. Since changing the slot configuration will inevitably have an effect on the input impedance into the antenna, this result implies that it may be possible to change the input impedance without degrading the radiation characteristics.

3.3.4 Evaluation of the array

The coplanar/slot line proximity-fed array appears to have one major drawback: the relative level of back radiation to broadside radiation. This problem is not unexpected. In previous work [9], it has been shown that a coplanar/slot feed virtually identical to the one used in this study can, in fact, be used as an efficient antenna element which radiates bidirectionally. It should also be pointed out that this back radiation problem is not unique to the feed network being considered here. Preliminary results of another proximity feed scheme [10] being considered for MMIC phased-array applications consisting of a microstrip/slot line configuration (the so-called "aperture coupled" microstrip line feed discussed briefly in Chapter 2) have been found to exhibit back radiation comparable to that measured for the coplanar/slot feed used in this study. Possible ways to reduce the back

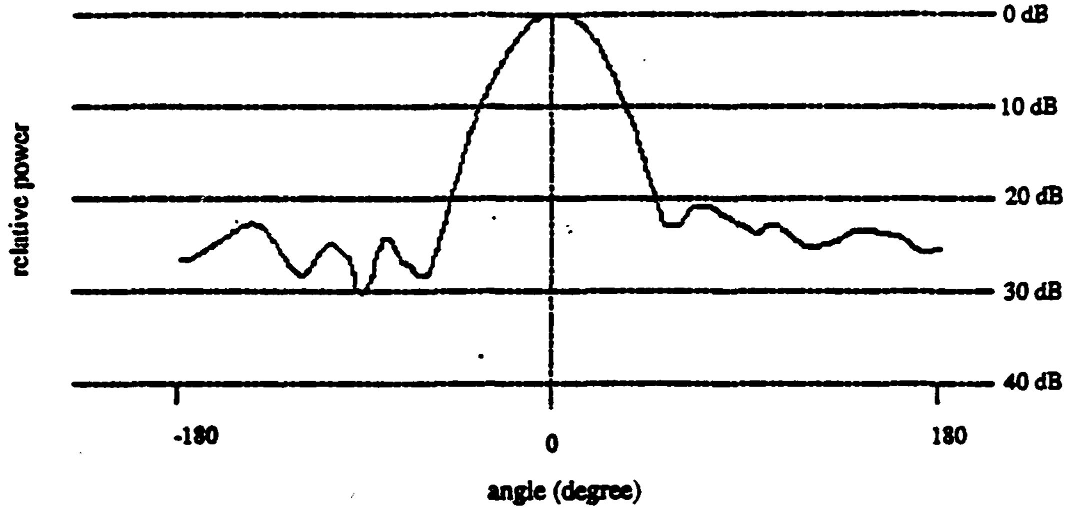

Fig. 3.10 H-plane radiation pattern of the four-element array with a primary slot feed: x = 9 mm, y= b/2.

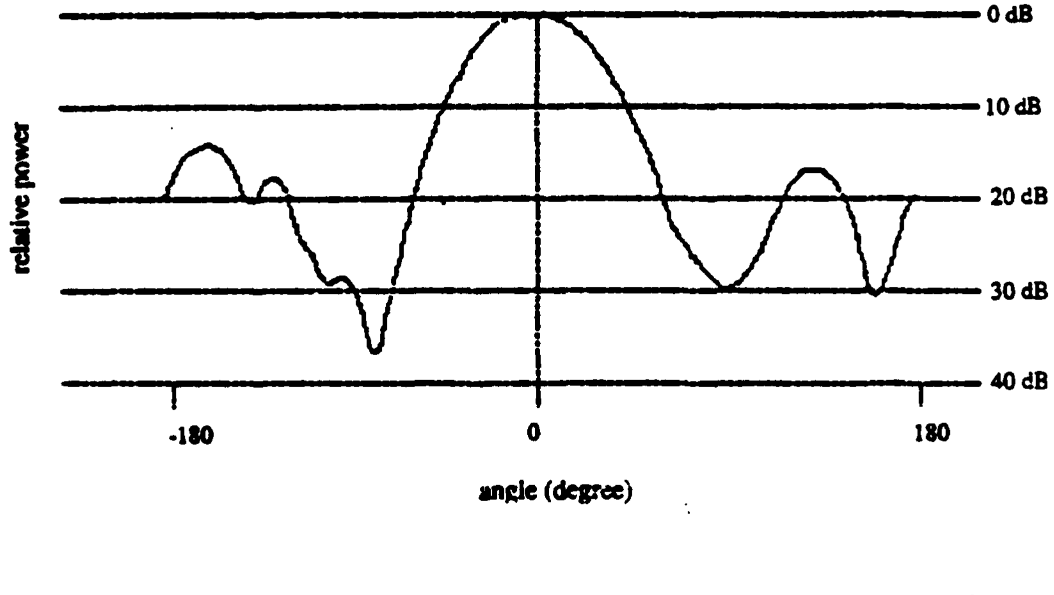

Fig. 3.11 E-plane radiation pattern of the four-element array with a primary slot feed: x = 9 mm, y= b/2.

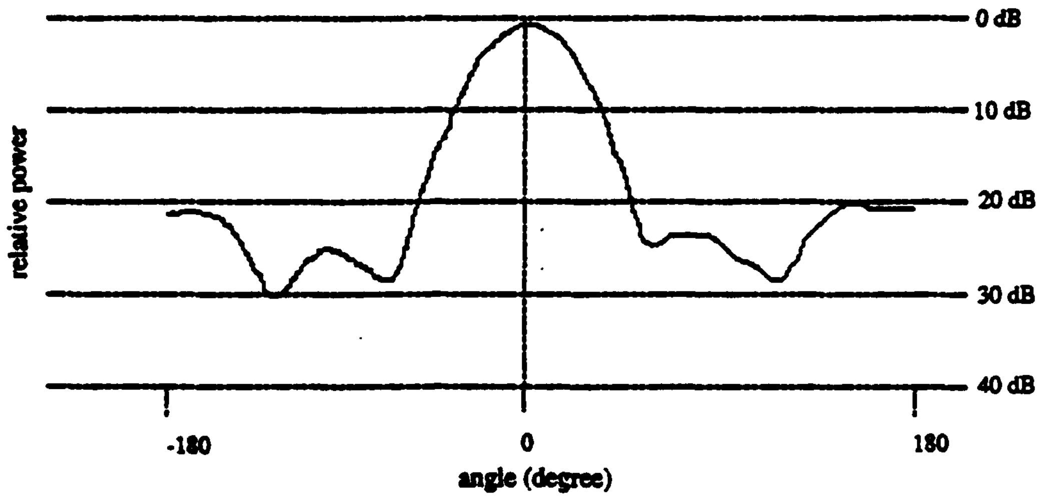

Fig. 3.12 H-plane radiation pattern of the four-element array with a primary slot feed: x = 9 mm, y= (b+1)/2.

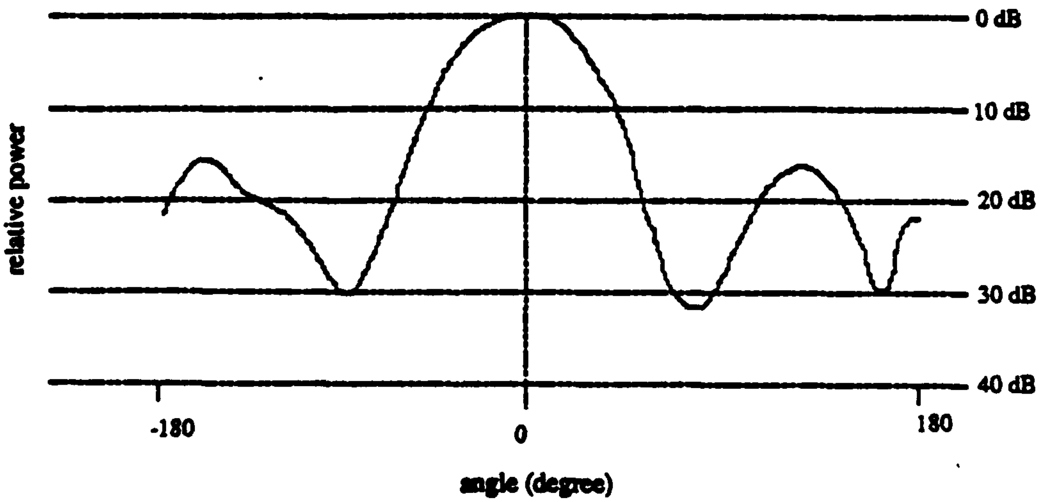

Fig. 3.13 H-plane radiation pattern of the four-element array with a primary slot feed: x = 9 mm, y= (b+1)/2.

radiation for both feed schemes are 1) narrower feed slots and 2) the addition of another ground plane.

Decreasing the width of the slots may reduce the level of back radiation relative to the broadside radiation from purely physical arguments, i.e., a larger aperture radiates more power than a smaller aperture. Further experimental and theoretical work is needed to determine how much of an improvement is possible.

The addition of a ground plane behind the slot feed will almost certainly eliminate the back radiation of not only the coplanar/slot line-fed array but of the aperture-coupled microstrip-fed case as well. Unfortunately, the addition of such a ground plane can result in the propagation of parallel-plate waveguide modes that can result in scan blindness [11]. It is also possible that such propagation may result in unwanted coupling between microwave circuits. Research needs to be done to investigate these potential problems.

3.4 Summary

This chapter presented an evaluation of the performance of a coplanar/slot proximity feed suitable for MMIC phased array applications. A qualitative description of the coupling between the feed and the antenna elements was presented. Preliminary experimental results of a 2x2 rectangular microstrip array with an operating frequency of 5.0 GHz were also presented. It was found that the array had very good characteristics, such as low side lobes and low cross polarization but that the back radiation is about 17 dB below the main beam. Additional measurements taken on arrays with modified slot-line feeds were shown which indicated that though it was possible to reduce the level of back radiation in the H-plane to as low as 23 dB below the main lobe, this had a tendency to increase the level of back radiation in the E-plane as high as 14 dB below the main lobe. Hence, it was concluded that it was not possible to reduce the back radiation by changing the slot-line configuration but that perhaps changing the slot width or adding a ground plane might resolve this problem. Further research needs to be done to explore this possibility.

CHAPTER 4

CHARACTERIZATION OF THE COPLANAR LINE FOR USE IN MMIC DESIGN

4.1 Introduction

In the preceding chapters there has been a great deal of emphasis on the possible application of the coplanar transmission line in MMIC phased arrays, particularly as a means of proximity feeding the array. But, as pointed out earlier, using a coplanar line in this manner implies that a significant portion of the microwave device circuitry as well as the interconnects must also be realized using the coplanar line. It is therefore important to determine the dispersion and loss characteristics of the coplanar line at frequencies that are being considered for MMIC fabrication, i.e., 10 to 100 GHz.

In Section 4.2, the importance of using both the static and full-wave analysis in determining the characteristics of the coplanar and microstrip transmission lines is reviewed. A discussion of their relative merits is also presented. In particular, the rationale behind using a full-wave analysis, rather than a static analysis, in the characterization of the planar transmission lines for general MMIC design is given.

In Section 4.3, a brief summary of the moment method (specifically, Galerkin's method) formulation used to compute the dispersion characteristics, i.e., the propagation constant of the line and the dielectric losses of the coplanar and microstrip lines, is presented.

In Section 4.4, the results obtained using the full-wave analysis developed in this study are compared with previously published experimental work [12]. Specifically, the frequency dependent nature of the coplanar line effective dielectric constant is examined. It is shown that the agreement between the two is very good. Moreover, a comparison of the results obtained using the full-wave analysis of this study with previously published full-wave results [13] shows that the analysis of this study is in better agreement with measured results. This is attributed to the use of basis and testing functions which, unlike the previous analysis, incorporates the so-called "edge condition" of the electric fields.

In Section 4.5, the dispersion and dielectric loss for a coplanar and microstrip line on a 100 micron GaAs substrate is compared. A discussion of the implications of this comparison is presented in the context of MMIC design. It is found that the coplanar line is less dispersive than the microstrip line for narrow-band applications, but that its effective dielectric constant is less than that of the microstrip line. In addition, it is found that, for typical "hot" conductor widths < 100 microns and substrate resistivities greater than 10^5 ohm-cm, the dielectric losses of both the coplanar and microstrip lines are negligible compared to the conductor losses.

In Section 4.6, preliminary results are presented which show that for single substrate coplanar waveguides with "hot" conductor widths approximately one half the substrate thickness, the propagation constant of the line undergoes "strong dispersion" in which the effective dielectric constant of the line increases dramatically with increasing frequency. In particular, the effective dielectric constant changes 30% from 10 GHz to 60 GHz. It is pointed out that, though undesirable for MMIC phased array applications, such coplanar lines may be useful in reducing the dispersion of broadband high-speed digital pulses.

4.2 The Static and Full-Wave Analyses

There are two ways to solve for the propagation characteristics of not only the coplanar line but any planar transmission line. They are 1) the static analysis and 2) the full-wave analysis.

The static analysis is based on the approximation that the electromagnetic wave propagating in the transmission line has transverse electric and magnetic fields (TEM) with respect to the direction of propagation. This approximation makes it possible to use the scalar potential Green's function in conjunction with the moment method to numerically compute the effective dielectric constant[3] and characteristic impedance of the coplanar line for any arbitrary stratified media. Another form of static analysis is to use conformal mapping techniques [14], [15], with which one can obtain simple analytic expressions for the effective dielectric constant and characteristic impedance of the coplanar line. Such analysis, however, is restricted to a limited number of coplanar geometries.

Unlike the static analysis, the full-wave analysis does not make the approximation that the propagation along the line is TEM. Instead, the actual non-TEM electric and magnetic field distributions along the transmission line are taken into account in an electric field dyadic Green's function. This allows one to numerically compute the frequency dependence of not only the effective dielectric constant (which is equivalent to computing the dispersion) but that of the dielectric loss and characteristic impedance. The full-wave analysis is amenable to any stratified media and is most easily implemented in the spectral domain.

4.2.1 Comparison of the static and full-wave analyses

The static analysis is usually much easier and more convenient to implement than the full-wave analysis. It tends to be easier to formulate and, more importantly, requires less computational effort. The major disadvantage of using the static analysis is that one cannot

---

[3] The effective dielectric constant is defined as the dielectric constant of an equivalent homogeneous , isotropic medium in which a TEM plane wave will travel at the same speed as the quasi TEM fields along the waveguide. In general, this quantity is frequency dependent.

compute the frequency characteristics of the geometry. For low microwave frequencies[4] , i.e., < 15 GHz, this deficiency is insignificant (this will be shown later). Hence, most microwave computer-aided design packages, such as SUPERCOMPACT or Touchstone, use formulas based on a static analysis with minor empirical corrections. At frequencies > 15.0 GHz, however, the TEM approximation becomes appreciably worse, particularly for dimensions on the order of millimeters. The transmission line characteristics start to differ markedly from the static values. As a result, a rigorous full-wave analysis must be carried out in order to accurately characterize the line for MMIC design between 10 and 100 GHz.

4.3 Full-Wave Analysis of the Coplanar Line

As stated earlier, a full-wave analysis used to calculate the effective propagation constant and the characteristic impedance is most easily done in the spectral domain. This is because the convolution integral relating the electric fields, electric currents and the dyadic Green's function can be simplified to a multiplication. By using Parseval's theorem, it is possible to relate the spectral domain equations with the spatial domain parameters to obtain the effective propagation constant of the line. The steps for formulating this spectral domain matrix equation and for solving the transmission-line characteristics may be summarized in three steps: 1) computation of the dyadic Green's function in the spectral domain, 2) formulation of a matrix equation relating the electric field with the electric current using the admittance matrix and 3) computation of the propagation constants using Galerkin's method in conjunction with a root-finding routine.

---

[4] At this juncture, this statement is somewhat vague. The frequencies of validity for the quasi-static analysis are *very much dependent* on the geometries and dielectric constants being considered. The smaller the dimensions compared to the wavelength of interest the more accurate the approximation becomes. For the dimensions being considered for MMIC design, i.e., 100 micron substrate thickness and a "hot" conductor width around 75 microns, frequencies less than 15 GHz will result in a value of less than 0.1 change in effective dielectric constant.

4.3.1 The spectral domain dyadic Green's function

There are many ways to calculate the spectral domain dyadic Green's function for planar sources (and no y components) in stratified media. These methods include 1) expanding the electric field in each region of the stratified media and matching the field and current at the interfaces (the "direct" method), 2) expanding the electric and magnetic fields in each region in terms of the magnetic vector potential and matching at the source plane (the "indirect" method), and 3) using the transmission-line analogy to match effective field impedances at the source plane (the so-called "spectral domain immitance technique") [16]. Since the spectral domain immitance technique is by far the simplest and most efficient method, it has been adopted in this study.

For the single substrate coplanar line geometry, the dyadic Green's function was found to be

$$\tilde{G}_{xx} = \frac{-\gamma_1\gamma_2}{j\omega}\left[\frac{\varepsilon_2\gamma_1 + \varepsilon_1\gamma_2\tanh\gamma_2 d}{2\varepsilon_1\varepsilon_2\gamma_1\gamma_2 + (\varepsilon_1^2\gamma_2^2 + \varepsilon_2^2\gamma_1^2)\tanh\gamma_2 d}\right]\frac{k_x^2}{k_x^2 + k_z^2} + \left[\frac{-j\omega\mu(\gamma_2 + \gamma_1\tanh\gamma_2 d)}{2\gamma_1\gamma_2 + (\gamma_1^2 + \gamma_2^2)\tanh\gamma_2 d}\right]\frac{k_z^2}{k_x^2 + k_z^2} \tag{4.1a}$$

$$\bar{G}_{xz} = \bar{G}_{zx} = \left(\frac{-\gamma_1\gamma_2}{j\omega}\left[\frac{\varepsilon_2\gamma_1 + \varepsilon_1\gamma_2 \tanh\gamma_2 d}{2\varepsilon_1\varepsilon_2\gamma_1\gamma_2 + (\varepsilon_1^2\gamma_2^2 + \varepsilon_2^2\gamma_1^2)\tanh\gamma_2 d} \right] - \left[\frac{-j\omega\mu(\gamma_2 + \gamma_1 \tanh\gamma_2 d)}{2\gamma_1\gamma_2 + (\gamma_1^2 + \gamma_2^2)\tanh\gamma_2 d} \right] \right) \frac{k_x k_z}{k_x^2 + k_z^2} \tag{4.1b}$$

$$\bar{G}_{zz} = \frac{-\gamma_1\gamma_2}{j\omega}\left[\frac{\varepsilon_2\gamma_1 + \varepsilon_1\gamma_2 \tanh\gamma_2 d}{2\varepsilon_1\varepsilon_2\gamma_1\gamma_2 + (\varepsilon_1^2\gamma_2^2 + \varepsilon_2^2\gamma_1^2)\tanh\gamma_2 d} \right] \frac{k_z^2}{k_x^2 + k_z^2} + \left[\frac{-j\omega\mu(\gamma_2 + \gamma_1 \tanh\gamma_2 d)}{2\gamma_1\gamma_2 + (\gamma_1^2 + \gamma_2^2)\tanh\gamma_2 d} \right] \frac{k_x^2}{k_x^2 + k_z^2} \tag{4.1c}$$

where d= substrate thickness

$k_{1,2}$= wave number in region 1,2

k_x= transform variable of x

k_z= transform variable of z

$\gamma_{1,2} = \sqrt{k_x^2 + k_z^2 - k_{1,2}^2}$

4.3.2 The spectral domain matrix equation

Once the spectral domain Green's function has been calculated, the matrix equation at some fixed y can be written using an impedance matrix formulation

$$\begin{bmatrix} \bar{Z}_{xx}(k_x,y) & \bar{Z}_{xz}(k_x,y) \\ \bar{Z}_{zx}(k_x,y) & \bar{Z}_{zz}(k_x,y) \end{bmatrix} \begin{bmatrix} \bar{J}_x(k_x,y) \\ \bar{J}_z(k_x,y) \end{bmatrix} = \begin{bmatrix} \bar{G}_{xx}(k_x,y) & \bar{G}_{xz}(k_x,y) \\ \bar{G}_{zx}(k_x,y) & \bar{G}_{zz}(k_x,y) \end{bmatrix} \begin{bmatrix} \bar{J}_x(k_x,y) \\ \bar{J}_z(k_x,y) \end{bmatrix} = \begin{bmatrix} \bar{E}_x(k_x,y) \\ \bar{E}_z(k_x,y) \end{bmatrix} \tag{4.2}$$

where the electric current is considered the unknown quantity, or equivalently, with an admittance matrix formulation,

$$\begin{bmatrix} \tilde{Y}_{xx}(k_x,y) & \tilde{Y}_{xz}(k_x,y) \\ \tilde{Y}_{zx}(k_x,y) & \tilde{Y}_{zz}(k_x,y) \end{bmatrix} \begin{bmatrix} \tilde{E}_x(k_x,y) \\ \tilde{E}_z(k_x,y) \end{bmatrix} = \begin{bmatrix} \tilde{G}_{xx}(k_x,y) & \tilde{G}_{xz}(k_x,y) \\ \tilde{G}_{zx}(k_x,y) & \tilde{G}_{zz}(k_x,y) \end{bmatrix}^{-1} \begin{bmatrix} \tilde{E}_x(k_x,y) \\ \tilde{E}_z(k_x,y) \end{bmatrix} = \begin{bmatrix} \tilde{J}_x(k_x,y) \\ \tilde{J}_z(k_x,y) \end{bmatrix} \tag{4.3}$$

where the electric field is considered the unknown quantity.

In a moment method solution of these matrix equations, it is necessary to eliminate either the electric field or the electric current both of which are unknown at this point. It turns out that the geometry of the problem determines which formulation should be used. In particular, the formulation will depend on whether the electric field or the electric current can be most easily expanded in terms of basis functions. For microstrip line configurations, the finite nature of the "hot" conductor at a fixed y-plane makes it convenient to expand the electric current and formulate the problem using the impedance matrix. For the coplanar line configuration, the finite nature of the slots at a fixed y-plane makes it convenient to expand the electric field and fomulate the problem using the admittance matrix.

4.3.3 Solution of admittance equation using Galerkin's method

To calculate the propagation constant of a coplanar transmission line (refer to Fig. 4.1, [17]), one must first formulate the spectral admittance matrix equation using the electric field in the slots. Possible solutions to this equation are then found by first expanding this field in the spatial domain as a sum of weighted basis functions. In particular, if there are z and x components of the electric field, this expansion would be of the form

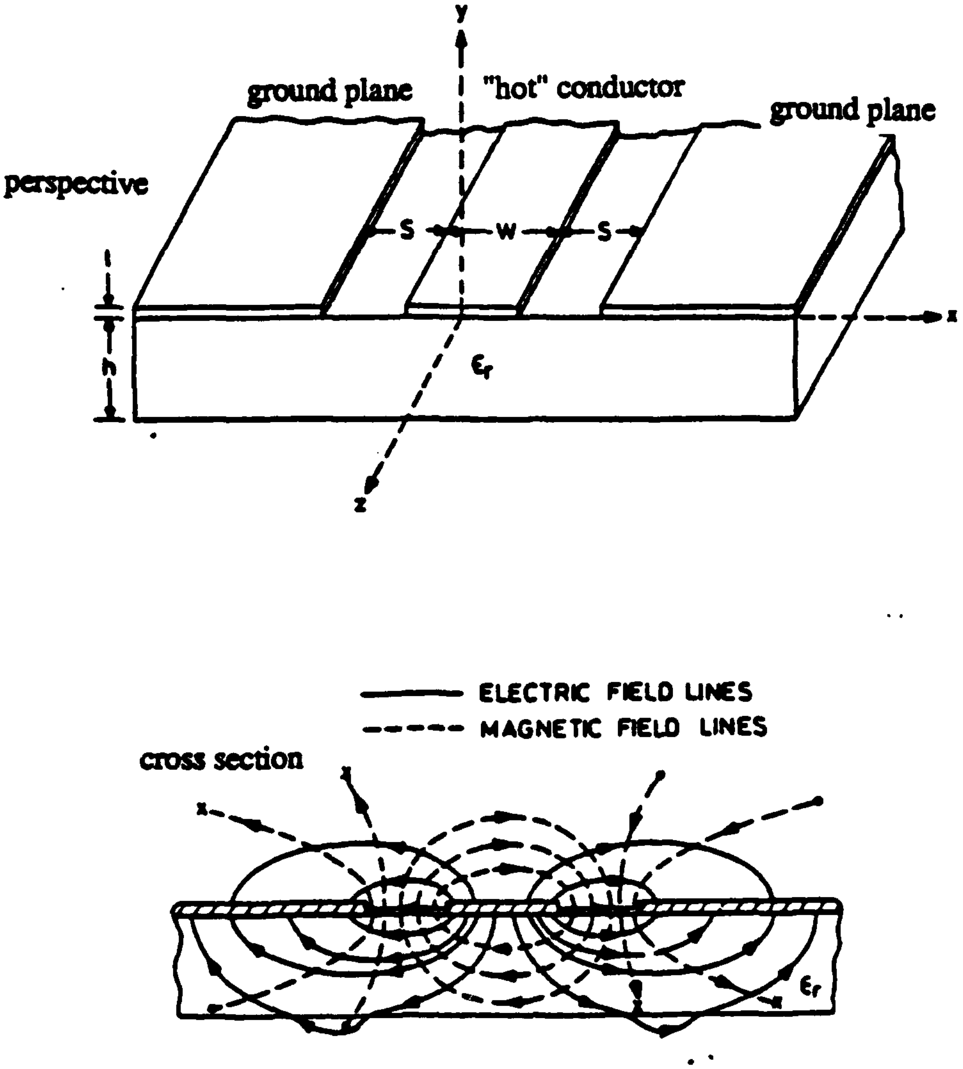

Fig. 4.1 The coplanar waveguide.

$$E_z \approx \sum_{n=0}^{N} b_n \theta_n(x,y) \tag{4.4}$$

$$E_x \approx \sum_{n=0}^{N} a_n \phi_n(x,y) \tag{4.5}$$

where b_n and a_n are weighting coefficients, $\theta_n(x,y)$, $\phi_n(x,y)$ are the basis functions and N is a finite integer. We note that with these two field components E_x and E_z tangent to the ground plane, all the other field components E_y, H_x, H_y and H_z are uniquely defined.

Due to the variational nature of Galerkin's method, the basis functions in the spatial domain should be chosen such that they approximate as closely as possible the actual field distribution. This will reduce the number of basis functions needed to represent the electric field components, which will, in turn, greatly reduce the numerical labor, which will be elaborated on shortly. For the analysis of the coplanar line, this implies that the basis function should satisfy the so-called "edge condition" in the slots, specifically, that the E_x component goes to infinity at the ground edge and that E_z go to zero. The following basis functions that have been commonly used in the analysis of coplanar structures satisfy these criteria and are adopted for this study:

$$E_z \text{ basis function: } \theta_n = \begin{cases} \dfrac{p_1(x)\cos\left(\frac{n\pi}{s}(x-.5(w+s))\right)}{\sqrt{(.5s)^2-(x-.5(w+s))^2}} + \dfrac{p_2(x)\cos\left(\frac{n\pi}{s}(x+.5(w+s))\right)}{\sqrt{(.5s)^2-(x+.5(w+s))^2}} & n = 1, 3, 5 \quad (4.6a) \\[2ex] \dfrac{p_1(x)\sin\left(\frac{n\pi}{s}(x-.5(w+s))\right)}{\sqrt{(.5s)^2-(x-.5(w+s))^2}} - \dfrac{p_2(x)\sin\left(\frac{n\pi}{s}(x+.5(w+s))\right)}{\sqrt{(.5s)^2-(x+.5(w+s))^2}} & n = 2, 4, 6 \quad (4.6b) \end{cases}$$

$$E_x \text{ basis function: } \phi_n = \begin{cases} \dfrac{p_1(x)\cos\left(\frac{n\pi}{s}(x-.5(w+s))\right)}{\sqrt{(.5s)^2-(x-.5(w+s))^2}} - \dfrac{p_2(x)\cos\left(\frac{n\pi}{s}(x+.5(w+s))\right)}{\sqrt{(.5s)^2-(x+.5(w+s))^2}} & n=0,2,4 \qquad (4.7a) \\ \dfrac{p_1(x)\sin\left(\frac{n\pi}{s}(x-.5(w+s))\right)}{\sqrt{(.5s)^2-(x-.5(w+s))^2}} + \dfrac{p_2(x)\sin\left(\frac{n\pi}{s}(x+.5(w+s))\right)}{\sqrt{(.5s)^2-(x+.5(w+s))^2}} & n=1,3,5 \qquad (4.7b) \end{cases}$$

where both θ_n and ϕ_n are defined for y in the plane of the slots and $p_1(x)$ and $p_2(x)$ are defined to be pulse functions equal to unity for $-((w/2)+s) < x < -(w/2)$, $(w/2) < x < ((w/2)+s)$, respectively, zero elsewhere (see Fig. 4.2).

The Fourier transforms of these functions can be readily shown to be

$$\tilde{\theta}_n = \begin{cases} \frac{1}{2}\cos\left(k_x\frac{s+w}{2}\right)\left[J_0\left(\frac{k_x s+n\pi}{2}\right)+J_0\left(\frac{k_x s-n\pi}{2}\right)\right] & n=1,3,5\ldots \qquad (4.8a) \\ \frac{1}{2}\sin\left(k_x\frac{s+w}{2}\right)\left[J_0\left(\frac{k_x s+n\pi}{2}\right)-J_0\left(\frac{k_x s-n\pi}{2}\right)\right] & n=2,4,6\ldots \qquad (4.8b) \end{cases}$$

$$\tilde{\phi}_n = \begin{cases} \frac{j}{2}\sin\left(k_x\frac{s+w}{2}\right)\left[J_0\left(\frac{k_x s+n\pi}{2}\right)+J_0\left(\frac{k_x s-n\pi}{2}\right)\right] & n=0,2,4\ldots \qquad (4.9a) \\ -\frac{j}{2}\cos\left(k_x\frac{s+w}{2}\right)\left[J_0\left(\frac{k_x s+n\pi}{2}\right)-J_0\left(\frac{k_x s-n\pi}{2}\right)\right] & n=1,3,5\ldots \qquad (4.9b) \end{cases}$$

where $J_0(\ )$=Bessel function of the first kind, zeroth order

k_x=transform variable

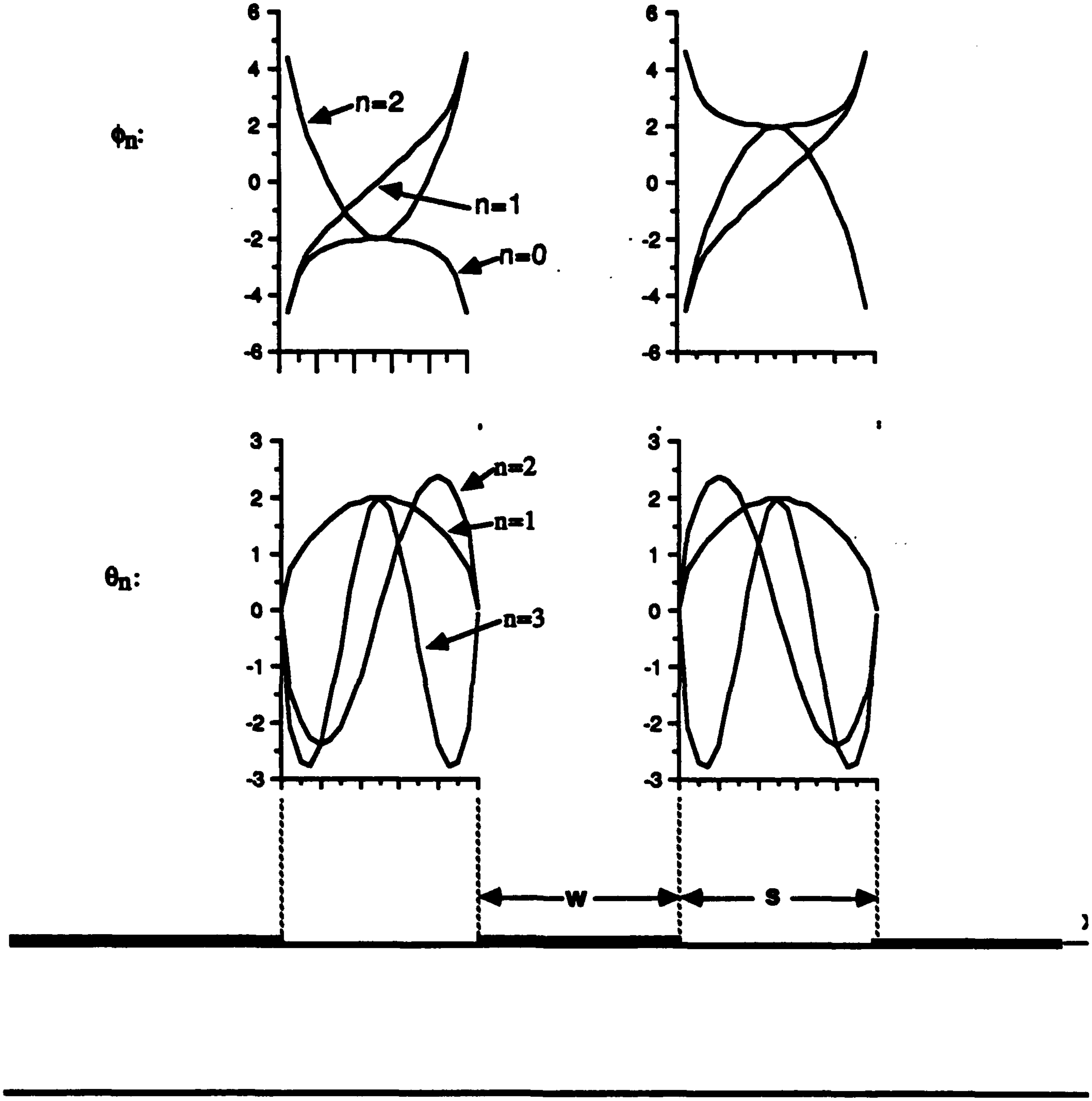

Fig. 4.2 Diagram of the basis functions used to expand the electric field inside the slots of the coplanar line.

It should be noted that these basis functions have been constructed with the implicit assumption that the odd mode is propagating. By substituting the expansions of E_Z and E_X into the admittance matrix formulation and testing each side with functions equal to the basis functions, Parseval's theorem is invoked to eliminate the unknown currents on the right-hand side. The result is a system of 2N homogeneous equations in 2N unknowns, which can be represented as

$$\begin{bmatrix}
\langle\tilde{Y}_{xx}\tilde{\phi}_1,\tilde{\phi}_1\rangle & \langle\tilde{Y}_{xx}\tilde{\phi}_2,\tilde{\phi}_1\rangle & \cdots & \langle\tilde{Y}_{xx}\tilde{\phi}_N,\tilde{\phi}_1\rangle & \langle\tilde{Y}_{xz}\tilde{\theta}_1,\tilde{\phi}_1\rangle & \langle\tilde{Y}_{xz}\tilde{\theta}_2,\tilde{\phi}_1\rangle & \cdots & \langle\tilde{Y}_{xz}\tilde{\theta}_N,\tilde{\phi}_1\rangle \\
\langle\tilde{Y}_{xx}\tilde{\phi}_1,\tilde{\phi}_2\rangle & \langle\tilde{Y}_{xx}\tilde{\phi}_2,\tilde{\phi}_2\rangle & \cdots & \langle\tilde{Y}_{xx}\tilde{\phi}_N,\tilde{\phi}_2\rangle & \langle\tilde{Y}_{xz}\tilde{\theta}_1,\tilde{\phi}_2\rangle & \langle\tilde{Y}_{xz}\tilde{\theta}_2,\tilde{\phi}_2\rangle & \cdots & \langle\tilde{Y}_{xz}\tilde{\theta}_N,\tilde{\phi}_1\rangle \\
\cdot & \cdot & \cdots & \cdot & \cdot & \cdot & \cdots & \cdot \\
\cdot & \cdot & \cdots & \cdot & \cdot & \cdot & \cdots & \cdot \\
\cdot & \cdot & \cdots & \cdot & \cdot & \cdot & \cdots & \cdot \\
\langle\tilde{Y}_{xx}\tilde{\phi}_1,\tilde{\phi}_N\rangle & \langle\tilde{Y}_{xx}\tilde{\phi}_2,\tilde{\phi}_N\rangle & \cdots & \langle\tilde{Y}_{xx}\tilde{\phi}_N,\tilde{\phi}_N\rangle & \langle\tilde{Y}_{xz}\tilde{\theta}_1,\tilde{\phi}_N\rangle & \langle\tilde{Y}_{xz}\tilde{\theta}_2,\tilde{\phi}_N\rangle & \cdots & \langle\tilde{Y}_{xz}\tilde{\theta}_N,\tilde{\phi}_1\rangle \\
\langle\tilde{Y}_{zx}\tilde{\phi}_1,\tilde{\theta}_1\rangle & \langle\tilde{Y}_{zx}\tilde{\phi}_2,\tilde{\theta}_1\rangle & \cdots & \langle\tilde{Y}_{zx}\tilde{\phi}_N,\tilde{\theta}_1\rangle & \langle\tilde{Y}_{zz}\tilde{\theta}_1,\tilde{\theta}_1\rangle & \langle\tilde{Y}_{zz}\tilde{\theta}_2,\tilde{\theta}_1\rangle & \cdots & \langle\tilde{Y}_{zz}\tilde{\theta}_N,\tilde{\theta}_1\rangle \\
\langle\tilde{Y}_{zx}\tilde{\phi}_1,\tilde{\theta}_2\rangle & \langle\tilde{Y}_{zx}\tilde{\phi}_2,\tilde{\theta}_2\rangle & \cdots & \langle\tilde{Y}_{zx}\tilde{\phi}_N,\tilde{\theta}_2\rangle & \langle\tilde{Y}_{zz}\tilde{\theta}_1,\tilde{\theta}_2\rangle & \langle\tilde{Y}_{zz}\tilde{\theta}_2,\tilde{\theta}_2\rangle & \cdots & \langle\tilde{Y}_{zz}\tilde{\theta}_N,\tilde{\theta}_2\rangle \\
\cdot & \cdot & \cdots & \cdot & \cdot & \cdot & \cdots & \cdot \\
\cdot & \cdot & \cdots & \cdot & \cdot & \cdot & \cdots & \cdot \\
\cdot & \cdot & \cdots & \cdot & \cdot & \cdot & \cdots & \cdot \\
\langle\tilde{Y}_{zx}\tilde{\phi}_1,\tilde{\theta}_N\rangle & \langle\tilde{Y}_{zx}\tilde{\phi}_2,\tilde{\theta}_N\rangle & \cdots & \langle\tilde{Y}_{zx}\tilde{\phi}_N,\tilde{\theta}_N\rangle & \langle\tilde{Y}_{zz}\tilde{\theta}_1,\tilde{\theta}_N\rangle & \langle\tilde{Y}_{zz}\tilde{\theta}_2,\tilde{\theta}_N\rangle & \cdots & \langle\tilde{Y}_{zz}\tilde{\theta}_N,\tilde{\theta}_N\rangle
\end{bmatrix}
\begin{bmatrix} a_1 \\ a_2 \\ \cdot \\ \cdot \\ \cdot \\ a_N \\ b_1 \\ b_2 \\ \cdot \\ \cdot \\ \cdot \\ b_N \end{bmatrix}
=
\begin{bmatrix} 0 \\ 0 \\ \cdot \\ \cdot \\ \cdot \\ 0 \\ 0 \\ 0 \\ \cdot \\ \cdot \\ \cdot \\ 0 \end{bmatrix}
\tag{4.10}$$

where $\langle\tilde{Y}\tilde{\phi},\tilde{\theta}\rangle = \int_{-\infty}^{\infty} \tilde{Y}(k_x,y,k_z)\,\tilde{\phi}(k_x,y)\,\tilde{\theta}(k_x,y)\,dk_x \equiv$ inner product

a_N, b_N = unknown weighting coefficients

$\tilde{Y}$, $\tilde{\phi}$, $\tilde{\theta}$ = Fourier transforms of Y, ϕ, θ, respectively, with respect to k_x.

From basic linear algebra theory, nontrivial values of the weighting coefficients (corresponding to nonzero values of the electric field) can exist if and only if the determinant is equal to zero. This condition can only be satisfied for certain values (otherwise known as eigenvalues) of the propagation constant, k_z. It should be noted that, in general, k_z will be complex if the dielectric constant of the stratified medium used in the derivation of the dyadic Green's function is complex.

In this study, the lowest-order eigenvalue corresponding to the quasi-TEM odd mode propagation is of interest. This value of k_z is found using an International Mathematics and Sciences Library (IMSL) root-finding routine based on Muller's method. This is a numerically intensive process, however, since the moment matrix must be recomputed for a range of possible k_z's, which, in turn, requires that the inner product must be recomputed for each k_z.

4.4 Comparison Between Experimental and Full-Wave Dispersion for a Coplanar Line on a Single Substrate

Though a single substrate line is unlikely to be used for phased arrays, it is useful for an MMIC circuit design of amplifiers or phase shifters. It may also provide some insight into the propagation characteristics of more complicated multilayered media which can be used in MMIC phased array design.

Figure 4.3 compares the effective dielectric constant versus frequency curves obtained using the full-wave analysis of this study with those of the static analysis [18] and published experimental results [12]. The agreement between all three results is found to be very good. As expected, the agreement between the static results and the full-wave results is best for frequencies < 5.0 GHz with the agreement worsening as the frequency increases. It is noted also that the static results and the full-wave results are, in general, slightly larger than the experimental results. This discrepancy can, in part, be accounted for by noting that Mueller cited approximate rather than exact dimensions for the coplanar lines used in his experiments.

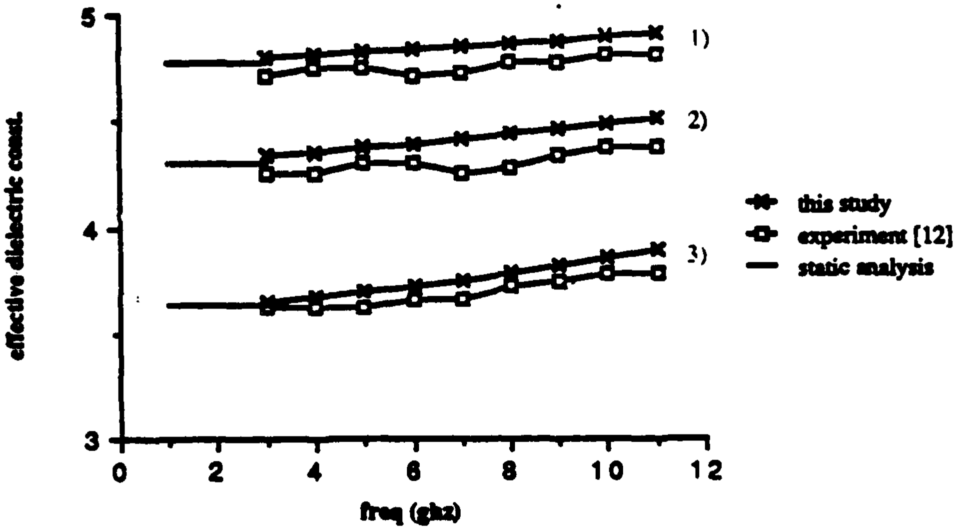

Fig. 4.3 Comparison of the full-wave coplanar line dispersion curves with experimental results [12].
(1) w/h=2.04, s/h=0.15
(2) w/h=1.95, s/h=0.66
(3) w/h=1.85, s/h=1.80
where w is the "hot" conductor width
h, the substrate thickness, =0.65mm
ε_r,, the substrate permittivity, =9.8

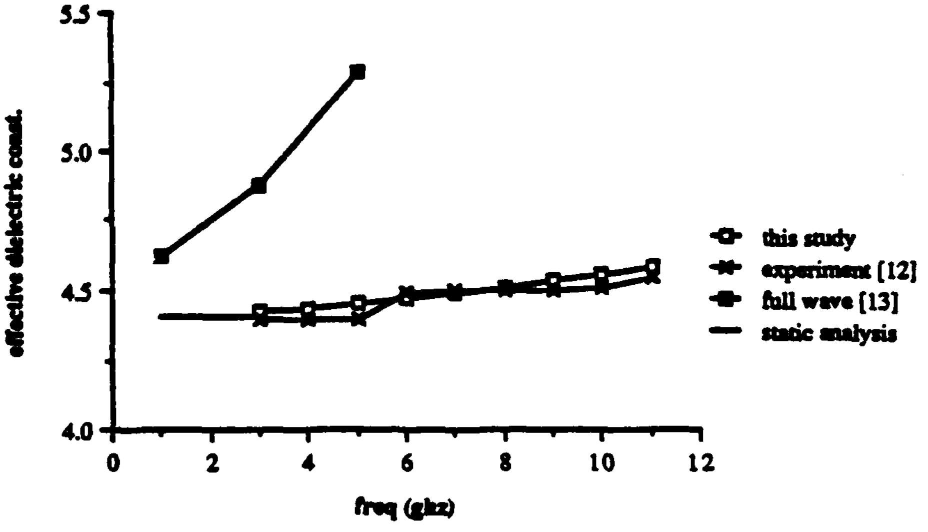

Fig. 4.4 Comparison of the full-wave coplanar line dispersion curves with reference [13] and experimental results [12].
w/h=1.00, s/h=1.09
where w is the "hot" conductor width
h, the substrate thickness, =0.65mm
ε_r,, the substrate permittivity, =9.8

Consequently, the physical dimensions that were input into the full-wave analysis and static analysis may have been in error resulting in the disagreement.

Figure 4.4 compares one dispersion curve obtained using the full-wave analysis of this study with the results from [12] and a previous full-wave analysis [13]. It can be seen that the results obtained in this study are in much better agreement with experimental and static analysis values than the previous analysis cited above. Moreover, the dispersion curve computed in this study predicts the frequency dependence much more accurately. The reason for this better agreement is most likely due to the different basis and testing functions used in this study compared to those used in the previous study. The previous study neglected to incorporate the proper edge conditions into their pulse basis and testing functions. In addition, the previous study probably did not use more than a single basis function in the description of the electric field components due to limited computing capabilities.

4.5 Coplanar Line vs. Microstrip Line for MMIC Design

One of the current issues in MMIC circuit design concerns the kind of planar transmission lines to be used as interconnects. In Chapter 2, this issue was discussed qualitatively. In this chapter, we quantitatively discuss the differences between the coplanar and microstrip line with regards to the dispersion and dielectric loss (Fig. 4.5, [17]) on a 100-micron GaAs substrate. Though a quantitative comparison between the microstrip line and coplanar line has been done previously [19], there have been, to the best of our knowledge, few frequency-dependent comparisons between them with respect to effective dielectric constant and dielectric loss. In this section, results for coplanar and microstrip lines with geometries likely to be used for MMIC design are presented and compared.

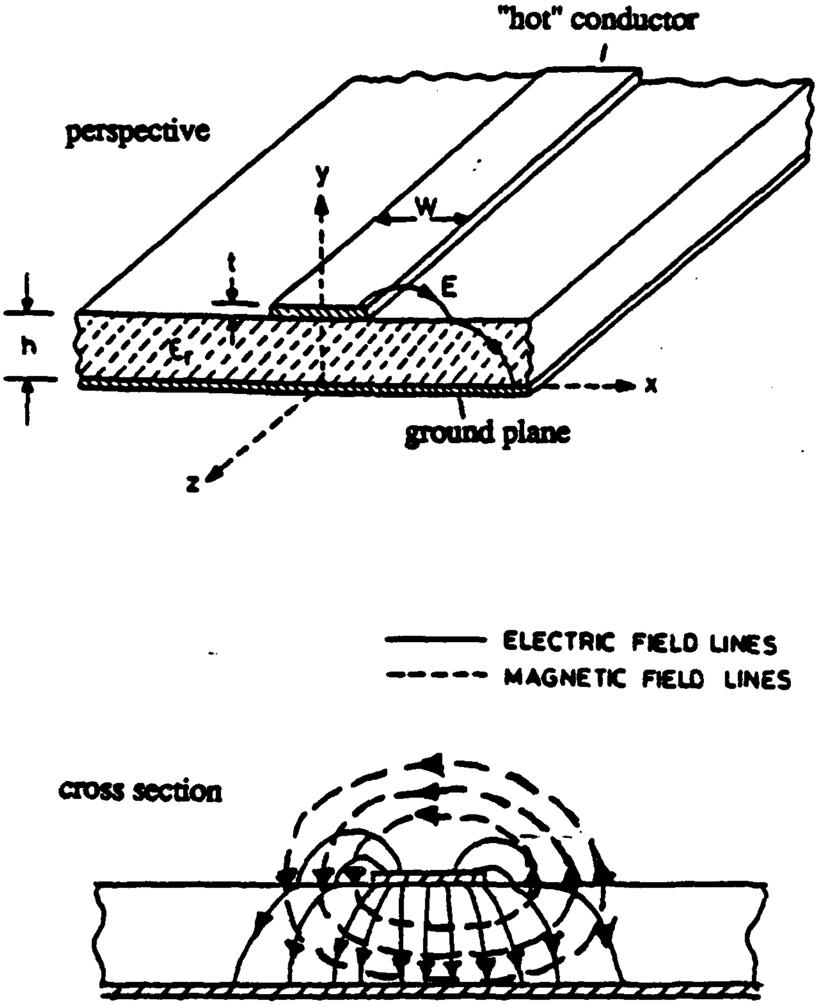

Fig. 4.5 The microstrip line.

4.5.1 Comparison of dispersion

Figure 4.6 shows the dispersion characteristics for several different microstrip and coplanar lines on a 100 micron GaAs substrate (e_r=12.91, ρ=10^7 ohm-cm). Each of the curves corresponds to the dispersion of either a coplanar line or microstrip line of approximately constant characteristic impedance[5]. There are essentially two major differences between the coplanar line and microstrip line that can be seen from this figure: 1) the coplanar line is less dispersive and 2) the microstrip line has a much higher effective dielectric constant.

For the typical MMIC geometries used in this comparison, the change in the effective dielectric constant is less than 4.0% from 10 to 100 GHz for a 50-ohm coplanar line whereas the change in the corresponding 50-ohm microstrip line is approximately 10.0%. This implies that for a circuit design between 10 and 100 GHz, an MMIC circuit design realized with the coplanar line will suffer less from the detrimental effects of dispersion than those realized in a microstrip line.

Though more dispersive than the coplanar line, the microstrip line has a significantly larger effective dielectric constant than that of the coplanar line, i.e., the approximate difference in wavelength of the 50-ohm microstrip line is 10.0% that of a wavelength of a comparable 50-ohm coplanar line for a 73 micron "hot" conductor on a 100 micron GaAs substrate. This is desirable since the distributed circuit elements realized in the microstrip line can be made smaller than that for the coplanar line, hence, making more economical use of the substrate.

The differences between the dispersion characteristics of the coplanar line and those of the microstrip line can be explained qualitatively. For example, the microstrip line has a larger

---

[5] These impedance values were calculated using a static formula. Though the characteristic impedances of both the coplanar and microstrip lines will change with frequency, this change can be shown to be < 6 ohms between 10 to 100 GHz.

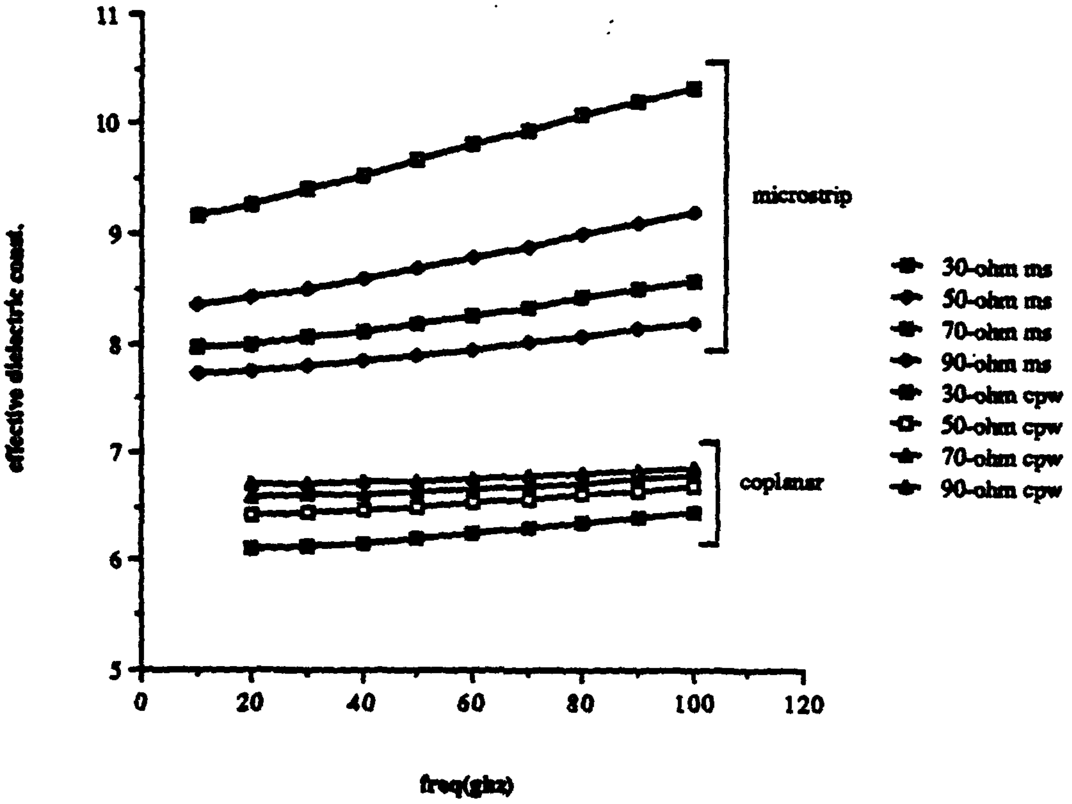

Fig. 4.6 Comparison of the coplanar line and microstrip line effective dielectric constant vs. frequency for equivalent impedances and "hot" conductor width, w.

coplanar line:30-ohm, $w/h=1.94$, $s/h=0.20$ microstrip line: 30-ohm, $w/h=1.95$
50-ohm, $w/h=0.73$, $s/h=0.45$ 50-ohm, $w/h=0.73$
70-ohm, $w/h=0.30$, $s/h=0.60$ 70-ohm, $w/h=0.30$
90-ohm, $w/h=0.12$, $s/h=0.65$ 90-ohm, $w/h=0.12$

where s is the coplanar line slot width
h, the substrate thickness, = .1mm
ε_r, the relative substrate permittivity, = 12.91.

effective dielectric constant because the ground plane is located underneath the substrate, whereas the coplanar line ground plane is located on the same plane. Since the field lines of the "hot" conductor must terminate on the ground plane, there is a much higher concentration of fields inside the GaAs substrate in the microstrip line case than in the coplanar line case. This implies that most of the electromagnetic energy propagating in the microstrip line, relative to the coplanar line case, can travel no faster than the speed of light inside the substrate. This has a tendency to increase the effective propagation constant of the microstrip line.

4.5.2 Comparison of dielectric loss

Figures 4.7 and 4.8 show the dielectric losses of coplanar and microstrip lines corresponding to the geometries used in the calculation of the dispersion curves. Unlike most dielectric loss analyses, which are based on some sort of perturbation method, these values were computed rigorously with the full-wave analysis. From the log scale plots it can be seen that the dielectric loss appears to be essentially constant over the 10 to 100 GHz range and these values are quite small, i.e., on the order of 10^{-4} dB/cm. Because of the small magnitudes involved[6], extensive computer time and accuracy are needed to obtain accurate results. By graphing these values on a linear scale, however, it can be seen that the coplanar and microstrip losses are actually increasing slightly with frequency. One notes that there are some anomalies in these curves, particularly in the 30-ohm case, in which the dielectric loss curves are not smooth. This is due to a numerical error resulting from the extremely small losses involved. Figure 4.7 shows that as the characteristic impedance of the coplanar line is decreased the dielectric loss decreases. Figure 4.8, on the other hand, shows that as the characteristic impedance of the microstrip line is decreased the dielectric loss increases. Both figures,

---

[6] For this case, the asymptotic value for the dielectric loss is 4.56×10^{-5} dB/cm.

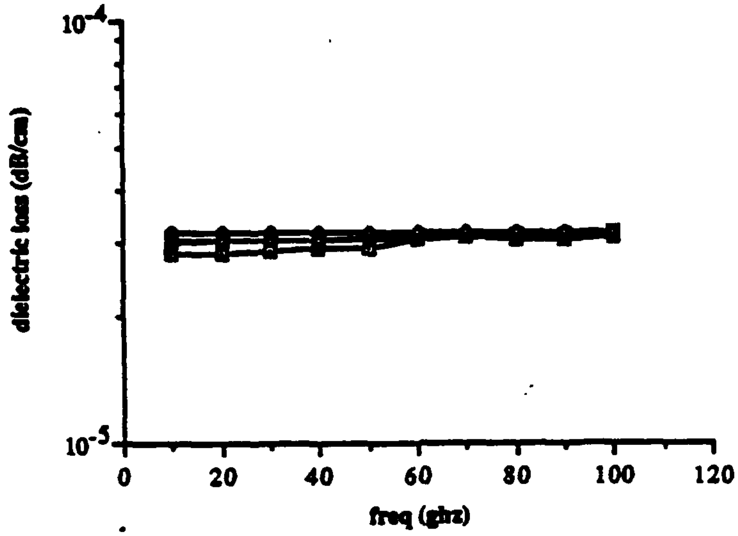

a) log scale

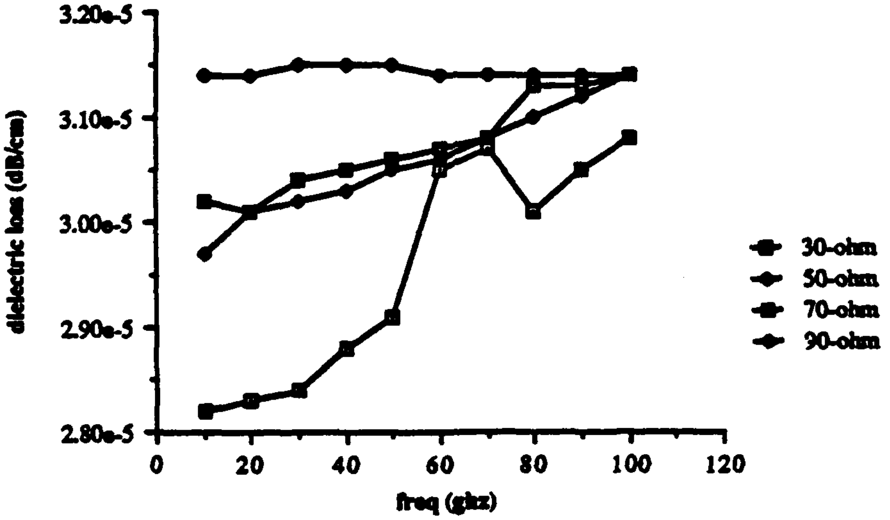

b) linear scale

Fig. 4.7 Dielectric loss vs. frequency for the coplanar line.

coplanar line: 30-ohm, w/h=1.94, s/h=0.20
50-ohm, w/h=0.73, s/h=0.45
70-ohm, w/h=0.30, s/h=0.60
90-ohm, w/h=0.12, s/h=0.65

where s is the coplanar line slot width
h, the substrate thickness, = .1mm
ε_r, the relative substrate permittivity, = 12.91.

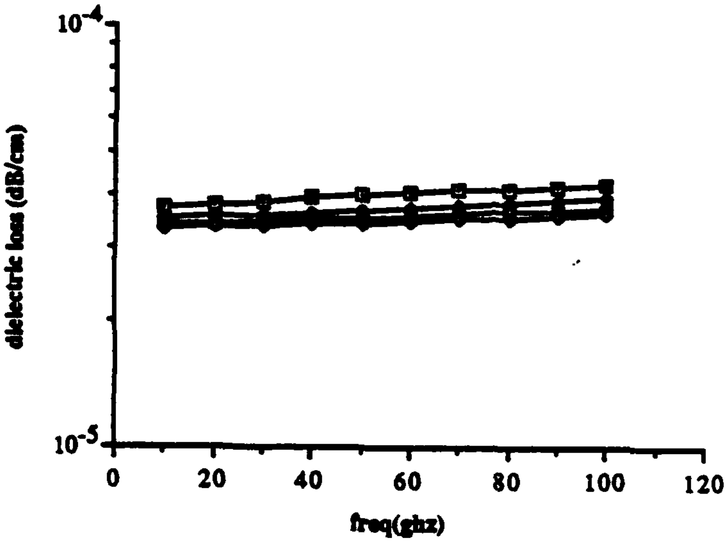

a) log scale

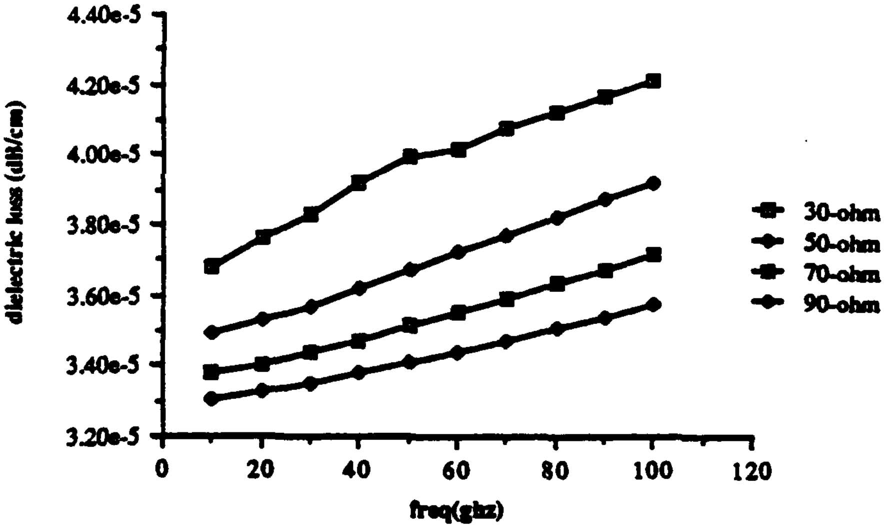

b) linear scale

Fig. 4.8 Dielectric loss vs. frequency for the microstrip line.
microstrip line: 30-ohm, w/h=1.95
50-ohm, w/h=0.73
70-ohm, w/h=0.30
90-ohm, w/h=0.12
where h, the substrate thickness, = .1mm
ε_r, the relative substrate permittivity, = 12.91.

however, show that the dielectric loss tends to increase with frequency and that the dielectric loss of the coplanar line is slightly less than that of microstrip line.

When computing the transmission line losses, it is common practice to assume that all the losses are due to the conductor losses and ignore the contributions of the dielectric loss. The magnitude of the dielectric losses calculated in this study appear to justify this approximation, i.e., the conductor losses are typically three orders of magnitude higher than the dielectric loss shown in Figs. 4.7 and 4.8. Figure 4.9, however, shows plots of the dielectric loss versus frequency and GaAs substrate resistivity for both the coplanar line and microstrip line. It can be seen that when GaAs has a resistivity of 10^4 ohm-cm the dielectric losses are of the same order as the conductor losses, hence, implying that the dielectric losses can no longer be ignored.

4.6 Strong Dispersion in a Single Substrate Coplanar Line

For the geometries used in the previous comparison it is clear that the coplanar line exhibits only slight dispersion between the 10 to 100 GHz range. Such dispersion characteristics are desirable for narrow-band applications, such as for phased arrays, but are undesirable for broadband high-speed digital pulse applications. To understand why this is true, one notes that at extremely high frequencies the entire electric field will tend to be completely confined inside the region of the highest dielectric. This tendency manifests itself in the dispersion curves of both the microstrip and coplanar lines [20]. At the lower frequencies both the microstrip and coplanar lines suffer only slight dispersion (i.e., the slope of the dispersion curve is very small) with an effective dielectric constant approximately one half that of the highest dielectric substrate. As the frequency increases, however, the dispersion

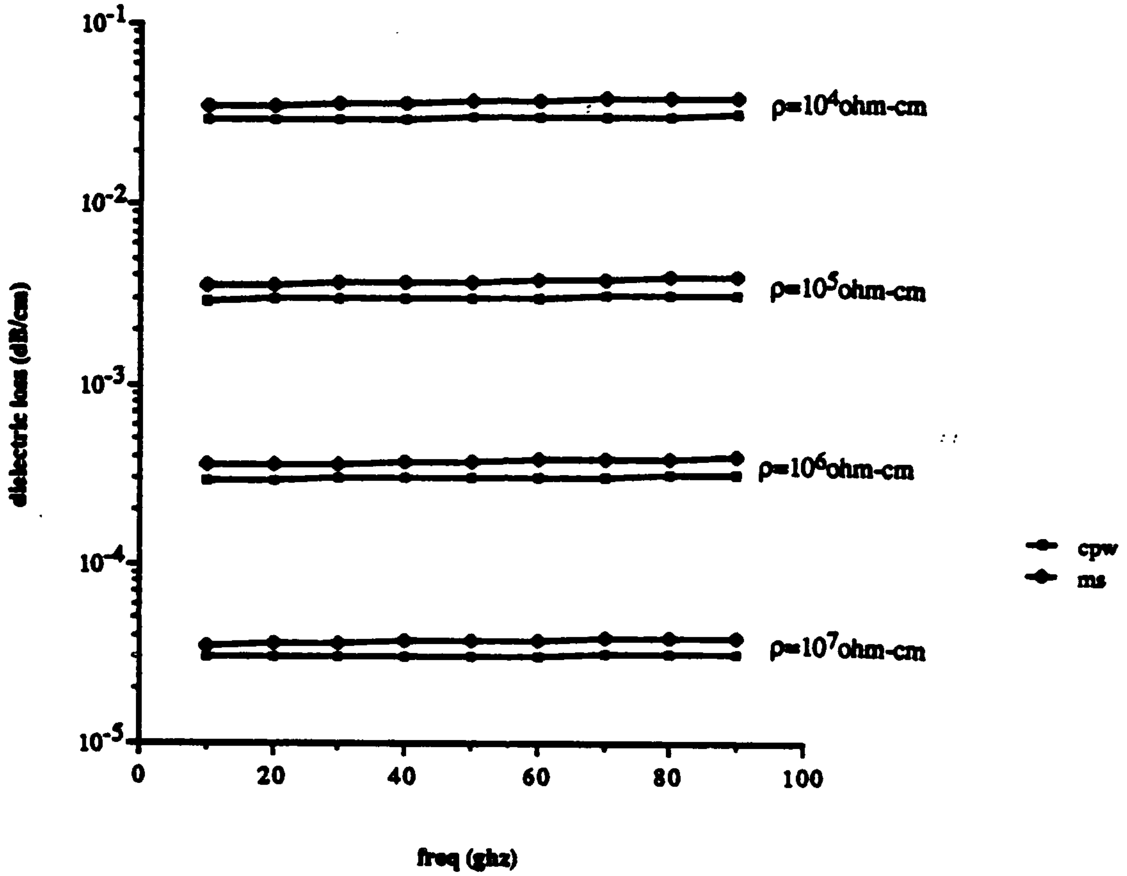

Fig. 4.9 Dielectric loss of a 50-ohm coplanar line and microstrip line vs. frequency for various substrate resistivities.
coplanar line: 50-ohm, $w/h=0.73$, $s/h=0.45$ microstrip line: 50-ohm, $w/h=0.73$
where h, the substrate thickness, = [illegible] um
ε_r, the relative substrate permittivity, $=12.91$.

becomes more and more pronounced until a frequency range is reached in which the dispersion increases dramatically. (Such increased dispersion will herein be referred to as "strong dispersion".) For frequencies much greater than those at the onset of strong dispersion, the dispersion curve reduces to approximately what it was before strong dispersion but at an effective dielectric constant much higher than before, i.e., the permittivity of the dielectric substrate (see Fig.4.10).

For high-speed digital pulse applications, i.e., rise time < 10 ps, the dispersion in the high frequency components is the major contributor to the dispersion of the pulse rather than the lower frequencies, i.e., < 100 GHz. Hence, unlike the narrow-band usage that is being considered for MMIC phased array design, it is desirable to construct a microstrip or a coplanar line which has its strong dispersion occurring at the lower frequencies rather than at the higher frequencies.

Figure 4.11 quantitatively illustrates the effect of varying the substrate thickness on the dispersion characteristics of the coplanar line. It can be seen that increasing the thickness can cause strong dispersion to occur at lower frequencies. This implies that in order to reduce the dispersion of narrow-band signals the substrate should be relatively thin. In contrast, this result also implies that in order to reduce the dispersion of broadband signals, the substrate should be relatively thick.

4.7 Summary

In this chapter, the importance of both a static analysis and a full-wave analysis was discussed. It was concluded that though the static analysis had the distinct advantage of being much simpler to implement in practice, a rigorous full-wave analysis was needed in order to

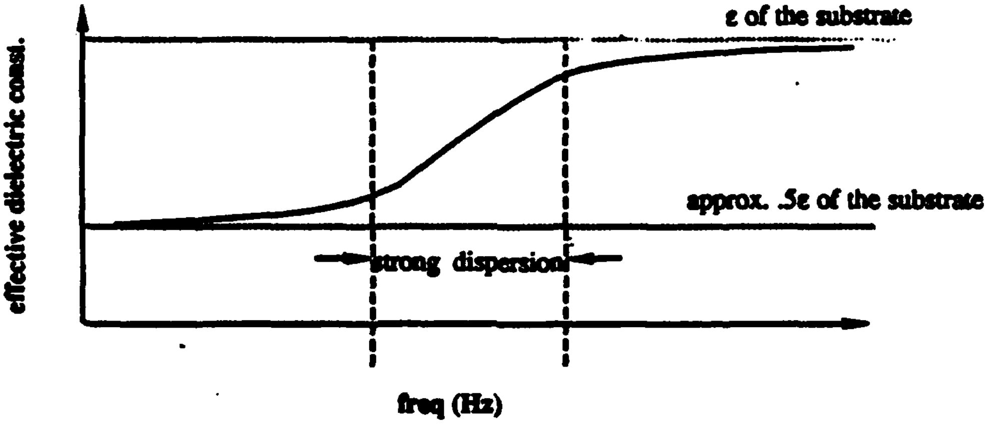

Fig. 4.10 A sketch of a typical dispersion curve for both the coplanar and microstrip transmission lines.

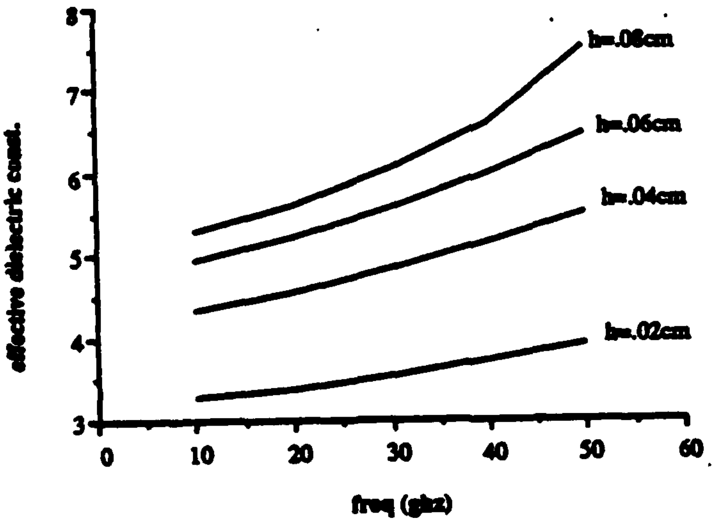

Fig. 4.11 Dispersion curves vs. substrate thickness, h, for the coplanar line.
where w, the "hot" conductor width, =0.10cm
s, the coplanar slot width, =0.03cm
ε_r, the relative substrate permittivity,=10.5.

quantitatively evaluate the transmission lines for MMIC phased array applications. This conclusion was based upon the fact that static analysis is accurate for low frequencies,i.e., < 15 GHz, and not for the high frequencies currently being considered (10 to 100 GHz) for MMIC design.

An outline of a spectral domain full-wave analysis used to solve for the effective propagation constant of a coplanar line was given. A brief outline of the steps used in the full-wave formulation was given. They included 1) determining the spectral dyadic Green's function using the spectral domain immitance technique 2) formulating the spectral admittance matrix equation and 3) expanding the electric field inside the coplanar slot region in terms of appropriate basis functions and using the spectral Galerkin's method to solve for the propagation constants (equivalent to finding the eigenvalues of a matrix equation).

A comparison between published experimental results for the dispersion characteristics of a coplanar line on a single substrate with those generated by a full-wave analysis developed for this study showed excellent agreement. In addition, it was found that the full-wave results also compared very well with those obtained using the static analysis. Moreover, a comparison between the dispersion curves obtained using the full-wave analysis in this study with those computed by others was made, and it was found that our analysis was in much better agreement with the experimental data. The reason for this was believed to be the different choice of basis functions used in this study which incorporated the so called "edge condition" of the electric field.

A quantitative comparison between the coplanar line and microstrip line was presented with regard to the MMIC design. In particular, the dispersion and dielectric loss of various coplanar and microstrip lines on a 100-micron GaAs substrate (e_r=12.91,ρ=10^7 ohm-cm) were compared using data generated by a full-wave analysis. It was found that the coplanar line is less dispersive and its effective dielectric constant is lower. The dielectric losses of both the coplanar and the microstrip lines were found to be negligibly small for resistivities $>10^4$ ohm-cm, but for resistivities less than that, the losses are comparable to conductor losses and should not be ignored. In addition, it was found that the coplanar line has less dielectric loss than the microstrip line for the geometries considered.

The design of coplanar lines for high-speed digital pulse applications was discussed briefly. Preliminary results indicate that it is possible to adjust the onset of "strong dispersion" in these lines by adjusting the substrate thickness so that the dispersion of the high frequency components is minimized.

CHAPTER 5

CONCLUSIONS AND FUTURE WORK

This study has focused mainly on the general design requirements for an MMIC active microstrip antenna phased array with an emphasis on using the coplanar line rather than the microstrip in the design of the feed network and active circuitry.

Chapter 2 qualitatively considered the requirements of monolithically integrating an antenna array with active device circuitry. It was concluded that the active array must be multilayered in order to accommodate all the required solid state devices, such as phase shifters, transistors and their associated biasing. This implied that the array must be proximity fed (no direct physical connection) using a corporate microstrip or coplanar line feed. As an illustration of this concept, a single element linearly polarized microstrip antenna (receive only) was designed with an open-end, coplanar-line proximity feed with a coplanar amplifier.

Chapter 3 presented experimental results of a novel four-element microstrip antenna array fed with a coplanar/slot line feed. It was experimentally found that the back radiation from the array is somewhat high (approximately 16 dB below the broadside radiation) and that it is not possible to reduce the back radiation by changing the lengths of the slot line used to feed the antenna or by changing the position of these slots under the patches. In addition, the measurements showed that the radiation patterns are approximately constant for a number of coplanar/slot line configurations implying that it is possible to adjust the input impedance of the antenna without degradation of antenna performance.

Chapter 4 quantitatively discussed the dispersion and dielectric loss characteristics of the coplanar line used in the feed structure. It was found that the results obtained by this study were in significantly better agreement with published experimental data than those for the previously published full-wave analysis. In addition, a quantitative comparsion between the dispersion and dielectric loss characteristics of the coplanar line and microstrip line on

100-micron GaAs was also made. It was found that the coplanar line is, for comparable geometries, less dispersive than the microstrip line for narrow-band microwave design but that the microstrip line had a larger effective dielectric constant. It was also found that for resistivities > 10^4 ohm-cm the dielectric loss is negligible compared to the conductor loss for frequencies as low as 10 GHz. In addition, preliminary dispersion curves were presented which show that the coplanar line may be made less dispersive for high-speed digital pulse propagation by increasing the substrate thickness.

5.1 Future Work

The work undertaken in this last period is quite preliminary. Much of the work was experimental in nature in order to obtain some preliminary insight into the problem. Many of the experiments were done simplistically, i.e., the antennas fabricated in this past year have been on single substrates rather than on multilayered media.

For future work all the experimental measurements need to be redone for multilayered media in order to more accurately determine the characteristics of the coplanar/slot fed microstrip array in a realistic MMIC setting. The full-wave coplanar line analysis should also be extended to multilayered media. The analysis should also be made to include the computation of the characteristic impedance of the line, conductor loss, and dispersion and dielectric losses.

Ways in which to reduce the back radiation from the coplanar/slot line fed arrays also need to be studied. Some of the solutions to be considered include decreasing the slot widths and placing a ground plane on the back of the antenna.

The input impedance of the array should also be examined. This past year the emphasis has been primarily on the radiation characteristics. No work, either experimental or analytical, has acutally been done to study the effects of the coplanar/slot geometry on the input impedance of the antenna. A full-wave analysis, in conjunction with experimental work, is sorely needed.

Research should be extended to include the possiblity of using the microstrip line in the design of the proximity feeds, in particular, the aperture coupled microstrip patch configuration [11]. It would be instructive to compare the coupling efficiency, i.e., coupling of energy from the feed to the antenna, of this microstrip feed vs. the coplanar/slot feed proposed in this study to see if there may be a compelling reason to choose one type of feed over the other. This sort of comparison is very difficult to do experimentally due to the required sensitivity of the equipment, hence, some sort of moment method analysis will be required.

Experimental and analytical work also needs to be done on characterizing coplanar line discontinuities for amplifier design before compact integration of the amplifier with the antenna array can be realized. Thus far, there has been very little published work in the literature which can aid the microwave engineer in the design of matching networks using the coplanar line.

REFERENCES

[1] R.J. Mailloux, "Phased architecture for millimeter wave active arrays," IEEE Antennas and Propagat. Society Newsletter, vol. 28,pp. 4-7, Feb. 1986.

[2] M. Houdart, "Coplanar lines: applications to broadband microwave integrated circuits," Proc. Sixth Eur. Microwave Conf., pp. 49-53, 1976.

[3] D.F. Williams, S.E. Schwarz, "Design and performance of coplanar waveguide bandpass filters, " IEEE Trans. Microwave Theory Tech., vol. MTT-31, pp. 558-566, July 1983.

[4] M. Riaziat, I. Zubeck, S. Bandy, and G. Zdasiuk, "Coplanar waveguide used in 2-18 GHz distributed amplifier," 1986 IEEE MTT-S Intl. Symposium Digest, pp. 337-338, Baltimore, MD, June 1986.

[5] R.S. Carson, High-Frequency Amplifiers, New York: John Wiley and Sons, Inc., 1982.

[6] J. Brenneman, private communication, 1985.

[7] Y.T. Lo, D. Solomon, and W.F. Richards, "Theory and experiment on microstrip antennas," IEEE Trans. Antennas Propagat., vol. AP-27, pp. 137-145, Mar. 1979.

[8] M. Oberhart, private communication, 1986.

[9] A. Nesic, "Slotted antenna array excited by a coplanar waveguide," Electronics Letters, vol, 18, pp. 275-276, Mar. 1982.

[10] D.M. Pozar, "A reciprocity method of analysis for printed slot and slot-coupled microstrip antennas," IEEE Trans. Antennas Propagat., vol. AP-34, Dec. 1986.

[11] D.M. Pozar, D.H. Schaubert, "Comparison of architectures for monolithic phased array antennas," Microwave Journal, vol. 29, pp. 93-104, Mar. 1986.

[12] E. Mueller, "Measurement of the effective relative permittivity of unshielded coplanar waveguides," Electronics Letters, vol. 13, pp. 729-730, Nov. 1977.

[13] J.B. Knorr, B. Kuchler, "Analysis of coupled slots and coplanar strips on dielectrics substrate," IEEE Trans. Microwave Theory Tech., vol. MTT-23, pp. 541-548, July 1975.

[14] C.P. Wen, "Coplanar waveguide: a surface strip transmission line suitable for nonreciprocal gyromagnetic device applications," IEEE Trans. Microwave Theory Tech., vol. MTT-17, pp. 1087-1090, Dec. 1969.

[15] C. Veyres, V. Fouad Hanna, "Extension of the application of conformal mapping techniques to coplanar lines with finite dimensions," Intl. Journal of Electronics, vol. 48, pp. 47-56, Jan. 1980.

[16] T. Itoh, "Spectral domain immitance approach for dispersion characteristics of generalized printed transmission lines," IEEE Trans. Microwave Thery Tech., vol. MTT-28, pp. 733-736, July 1980.

[17] K.C. Gupta, R. Garg, I.J. Bahl, Microstrip Lines and Slotlines, Needham: Artech House, Inc., 1979

[18] M.E. Davis, E.W. Williams, and A.C. Celestini, "Finite-boundary corrections to the coplanar waveguide analysis," IEEE Trans. Microwave Theory Tech., vol. MTT-21, pp. 594-596, Sept. 1973.

[19] R.W. Jackson, "Coplanar waveguide vs. microstrip for millimeter wave integrated circuits," 1986 IEEE MTT-S Intl. Symposium Digest, pp. 699-702, Baltimore, MD, June 1986.

[20] G. Hasnain, A. Dienes, and J.R. Whinnery, "Dispersion of picosecond pulses in coplanar transmission lines," IEEE Trans, Microwave Theory Tech., vol. MTT-34, pp. 738-741, June 1986.

MISSION
of
Rome Air Development Center

RADC plans and executes research, development, test and selected acquisition programs in support of Command, Control, Communications and Intelligence (C^3I) activities. Technical and engineering support within areas of competence is provided to ESD Program Offices (POs) and other ESD elements to perform effective acquisition of C^3I systems. The areas of technical competence include communications, command and control, battle management information processing, surveillance sensors, intelligence data collection and handling, solid state sciences, electromagnetics, and propagation, and electronic reliability/maintainability and compatibility.